High Precision Thermal Morphing of the Smart Anisogrid Structure for Space-Based Applications.

Austin A. Phoenix

Dissertation submitted to the faculty of the Virginia Polytechnic Institute and State University in partial fulfillment of the requirements for the degree of

Doctor of Philosophy
In
Mechanical Engineering

Pablo A. Tarazaga
Kevin B. Kochersberger
Jeff T. Borggaard
William J. Scharpf
Robert L. West
Michael K. Philen

August 25th 2016
Blacksburg, Va.

Keywords: Finite Element Analysis, Model Reduction, Parameter Ranking and Identification, Thermal Morphing, Structural Optimization, Anisogrid Structure

High Precision Thermal Morphing of the Smart Anisogrid Structure for Space-Based Applications.

Austin A. Phoenix

Abstract

To meet the requirements for the next generation of space missions, a paradigm shift is required from current structures that are static, heavy and stiff, to innovative structures that are adaptive, lightweight, versatile, and intelligent. This work proposes the use of a novel morphing structure, the thermally actuated anisogrid morphing boom, to meet the design requirements by making the primary structure actively adapt to the on-orbit environment. The proposed concept achieves the morphing capability by applying local and global thermal gradients and using the resulting thermal strains to introduce a 6 Degree of Freedom (DOF) morphing control. To address the key technical challenges associated with implementing this concept, the work is broken into four sections. First, the capability to develop and reduce large dynamic models using the Data Based Loewner-SVD method is demonstrated. This reduction method provides the computationally efficient dynamic models required for evaluation of the concept and the assessment of a vast number of loading cases. Secondly, a sensitivity analysis based parameter ranking methodology is developed to define parameter importance. A five parameter model correlation effort is used to demonstrate the ability to simplify complex coupled problems. By reducing the parameters to only the most critical, the resulting morphing optimization computation and engineering time is greatly reduced. The third piece builds the foundation for the thermal morphing anisogrid structure by describing the concept, defining the modeling assumptions, evaluating the design space, and building the performance metrics. The final piece takes the parameter ranking methodology, developed in part two, and the modeling capability of part three, and performs a trust-region optimization to define optimal morphing geometric configuration. The resulting geometry, optimized for minimum morphing capability, is evaluated to determine the morphing workspace, the frequency response capability, and the minimum and maximum morphing capability in 6 DOF. This work has demonstrated the potential and provided the technical tools required to model and optimize this novel smart structural concept for a variety of applications.

High Precision Thermal Morphing of the Smart Anisogrid Structure for Space-Based Applications.

Austin A. Phoenix

General Audience Abstract

To meet the requirements for the next generation of space missions, a paradigm shift is required from current structures that are static, heavy and stiff, to innovative structures that are adaptive, lightweight, versatile, and intelligent. This work proposes the combination of a unique structure with a new control method to provide a novel way to achieve smart structural adaptive (morphing) capability. This concept takes advantage of the natural expansion and contraction of materials caused by temperature changes (Coefficient of Thermal Expansion) to bend and twist the structure of interest into the desired configuration. By applying local heat (thermal energy) to induce temperature differences in the structure, the temperature induced material expansion (thermal strain) can be used to control and direct the structure into all different planes and rotations(X, Y, and Z displacements as well as the rotations in the X, Y, and Z axis). This structure is called an anisogrid boom. The potential applications of model range from passive thermal mitigation system to an active precision low frequency vibration control system. The anisogrid boom is a low mass and efficient structural configuration with a long history in aerospace applications. The thermally morphing anisogrid structure is made up of helical members (these members are heated and cooled to actively bend and twist the structure) and circumferential members (these members provide stability and rigidity to the structure). This work details the methods used to move and control the structure as well as the development of the technical capabilities required to effectively demonstrate the limits of the concept. To address the key technical challenges associated with implementing this concept, the work is broken into four sections. First, the method is detailed that is used to generate the large dynamic computer models and the method to reduce them using a model reduction method, Data Based Loewner-SVD. This reduction method provides the computationally-efficient dynamic models required for evaluation of the concept. Secondly, a novel methodology is discussed identifying the impact of an input parameter change on the resulting output, such that the parameters of importance can be ranked. This ranking provides insight into what parameters should be the focus for further evaluation and optimization. The last two sections address how these tools are used to demonstrate the performance of this novel morphing structure as a function of the geometric input parameters relative to multiple developed performance metrics. Finally, the structure is optimized to achieve the most accurate morphing possible so that the limits of the capability can be better understood. This work has demonstrated the potential and provided the technical tools required to model and optimize this novel smart structural concept for a variety of applications.

First I have to dedicate this work to my advisor, Dr. Tarazaga. You convinced me to believe that this insurmountable effort was realistic. That belief was enough to make this totally unreasonable work compliable. I need to thank the whole Tarazaga family, both through blood and through choice, the environment that you created made this challenging experience a joy. To my parents and sister, for your blind unending support, you were always there to pick me up when I needed it. Finally, to my wife without your endless love, support, understanding, sacrifices, and cooking I would not have dared take on this whole adventure.

If I have seen further than others, it is by standing upon the shoulders of giants.

-Isaac Newton

Table of Contents

Dynamic Model Reduction Using Data-Based Loewner-SVD Methods applied to Thermally Morphing Structures

Improved Model Correlation through Optimal Parameter Ranking using Model Reduction Algorithms: Augmenting Engineering Judgment

Thermal Morphing Anisogrid Smart Space Structures Part 1: Introduction, Modeling, and Performance of the Novel Smart Structural Application.

Thermal Morphing Anisogrid Smart Space Structures Part 2: Ranking of Geometric Parameter Importance, Trust Region Optimization, and Performance Evaluation.

Table of Figures

Dynamic Model Reduction Using Data-Based Loewner-SVD Methods applied to Thermally Morphing Structures

Improved Model Correlation through Optimal Parameter Ranking using Model Reduction Algorithms: Augmenting Engineering Judgment

Thermal Morphing Anisogrid Smart Space Structures Part 1: Introduction, Modeling, and Performance of the Novel Smart Structural Application.

Thermal Morphing Anisogrid Smart Space Structures Part 2: Ranking of Geometric Parameter Importance, Trust Region Optimization, and Performance Evaluation.

Table of Tables

Dynamic Model Reduction Using Data-Based Loewner-SVD Methods applied to Thermally Morphing Structures

Improved Model Correlation through Optimal Parameter Ranking using Model Reduction Algorithms: Augmenting Engineering Judgment

Thermal Morphing Anisogrid Smart Space Structures Part 1: Introduction, Modeling, and Performance of the Novel Smart Structural Application.

Thermal Morphing Anisogrid Smart Space Structures Part 2: Ranking of Geometric Parameter Importance, Trust Region Optimization, and Performance Evaluation.

Attribution: The author would like to highlight the effort provided by the co-authors in this work. Dustin Bales and Rodrigo Sarlo provided significant efforts in the manuscript titled "Improved Model Correlation through Optimal Parameter Ranking using Model Reduction Algorithms: Augmenting Engineering Judgment." Dustin Bales wrote the Q-DEIM, DEIM, Projection Coefficient and Weighted Projection Coefficient model reduction method codes, and also developed the novel Weighted Projection Coefficient Method. Rodrigo Sarlo helped develop the geometric configuration and identify the parameters to be used for the model correlation investigation and provided help in the methodology development. The author would like to thank the input and suggestions from the co-authors.

This page intentionally left blank

Preface

The intent of this effort is to demonstrate the thermal morphing anisogrid system's ability to provide novel high precision morphing capability needed to meet the design requirements of future space systems. The purpose of this work is to expand the capability of current adaptive structures by building smart structure systems that meet the on-orbit design requirements by actively adapting to the changing environment. This shift in methodology provides significant mass savings potential allowing, not only for cost savings, but also for enabling new mission architectures. Significant effort has been expended on the development of smart structures to address vibration, thermal distortion, deployment control, and overall intelligent environment control capability [1-15]. This concept has the potential to increase the capability of gossamer or large space structures [16, 17], where the mass is the driving design constraint [9, 16-23], by meeting the high precision displacement requirements of spacecraft systems more efficiently. To provide this capability, the thermal anisogrid concept achieves the morphing control through the use of thermal strain to actuate the individual helical members in the anisogrid structure. Properly controlling the temperatures of multiple helical members can introduce 6 Degrees of Freedom (DOF) morphing control. This system couples the use of low Coefficient of Thermal Expansion (CTE) materials with precise thermal control to provide the high precision morphing capability. The focus of this work is to define the limits of the morphing accuracy achievable by the novel thermal morphing anisogrid smart structure.

This work details the technical developments used to model, evaluate, and optimize the morphing performance of this novel morphing structural concept, the thermally actuated anisogrid morphing boom. Four key technical tasks were completed in order to develop the technical capability and optimize this complex structure. The first technical effort investigates the dynamic structural modeling of these complex dynamic structures and the reduction of the dynamic model through the use of the data based Loewner-SVD method. Not only does the model reduction reduce the cost of evaluating the structure, but it also enables future efforts to more efficiently investigate the dynamic properties of the complex anisogrid structure. The second technical challenge was the development of new sensitivity analysis methods to reduce a complex correlation, or optimization problem, to its most essential inputs. This method enables efficient optimization by eliminating all but the critical parameters required to identify the optimal geometry performance. The third challenge was focused on the development of the modeling requirements, the building of performance metrics, and investigation into the design space of the system. These developments build the required technical capability that allows for the fourth and final effort to efficiently find the optimal morphing capability of this complex morphing system.

While there are a significant number of FEM model reduction methods proposed in the literature, the approach demonstrated in this effort provides an opportunity unattained in currently adopted reduction methods. The work herein can be extended to model generation using experimental measurements by simply replacing the FEM output data used in this investigation with actual test measurements. This method will be demonstrated on two thermally morphing structures to determine properties of the reduction. This chapter, titled "Dynamic Model Reduction Using Data-Based Loewner-SVD Methods applied to Thermally Morphing Structures," details the method and identifies the benefits of the reduced model methodology.

In an attempt to reduce the complexity of highly coupled multi-parameter problems, such as model correlation, a methodology is demonstrated on the ranking and reduction of correlation parameters using model reduction techniques and an iterative FEM is discussed and evaluated. The proposed methodology attempts to use established model reduction methods to determine the parameters that are most mathematically independent, so that redundant, or low impact parameters, are not required for correlation and can thus be truncated. These techniques, when used in conjunction with classic or state-of-the-art correlation methods, identify the minimum number of parameters required to achieve the majority of the correlation, resulting in a faster, more efficient model correlation effort. This study focuses on expanding the capability of sensitivity analysis by adding intelligence to the ranking method. This work is demonstrated in the chapter titled "Improved Model Correlation through Optimal Parameter Ranking using Model Reduction Algorithms: Augmenting Engineering Judgment."

To evaluate the design space and perform the morphing optimization, a parameterized Finite Element Model (FEM) is developed to generate, run, and evaluate the morphing output. This model is used to calculate the performance of the nominal geometry and to perform a parameter sweep for all nine geometric parameters to better quantify the variations within the design space. The parameter ranking methodology, described in the second chapter, identifies the critical parameters for optimization so a reduced optimization set can be defined. The optimal geometry is then evaluated, using this reduced parameter set, to define the workspace quality, the minimum and maximum morphing capability for multiple materials, and to define the frequency response capability as a function of available power. This effort is detailed in the third and fourth chapters titled "Thermal Morphing Anisogrid Smart Space Structures Part 1 Introduction, Modeling, and Performance of the Novel Smart Structural Application" and "Thermal Morphing Anisogrid Smart Space Structures Part 2 Ranking of Parameter Importance, Trust Region Optimization, and Performance Evaluation."

This dissertation demonstrates the technical developments required to evaluate the capability of the thermal morphing anisogrid structure. This work uses these tools to answer the key technical questions regarding the morphing concepts minimum morphing capability, morphing range, workspace quality, and the frequency response capabilities.

References

1. Wada, B.K., *Adaptive structures-An overview.* Journal of spacecraft and rockets, 1990. 27(3): p. 330-337.
2. Thayer, D., et al., *Six-axis vibration isolation system using soft actuators and multiple sensors.* Journal of spacecraft and rockets, 2002. 39(2): p. 206-212.
3. Thill, C., et al., *Morphing skins.* The Aeronautical Journal, 2008. 112(1129): p. 117-139.
4. Kuder, I.K., et al., *Variable stiffness material and structural concepts for morphing applications.* Progress in Aerospace Sciences, 2013. 63: p. 33-55.
5. Li, W. and H. Huang, *Integrated optimization of actuator placement and vibration control for piezoelectric adaptive trusses.* Journal of Sound and Vibration, 2013. 332(1): p. 17-32.
6. Toropova, M.M., *THERMAL ACTUATION THROUGH BIMATERIAL LATTICES*, in *SMASIS*. 2015.
7. Yang, J., et al., *Design of a Vibration Isolation System for the Space Telescope.* Journal of Guidance, Control, and Dynamics, 2015: p. 1-8.
8. Tarazaga, P.A., D.J. Inman, and W.K. Wilkie, *Control of a space rigidizable inflatable boom using macro-fiber composite actuators.* Journal of Vibration and Control, 2007. 13(7): p. 935-950.

9. Ruggiero, E.J. and D.J. Inman, *Gossamer spacecraft: recent trends in design, analysis, experimentation, and control.* Journal of Spacecraft and Rockets, 2006. 43(1): p. 10-24.
10. Ramrakhyani, D.S., et al., *Aircraft structural morphing using tendon-actuated compliant cellular trusses.* Journal of aircraft, 2005. 42(6): p. 1614-1620.
11. Korkmaz, S., *A review of active structural control: challenges for engineering informatics.* Computers & Structures, 2011. 89(23): p. 2113-2132.
12. Hiroaki, T., et al., *Development of a smart reconfigurable reflector prototype for an extremely high-frequency antenna.* Journal of Intelligent Material Systems and Structures, 2015: p. 1045389X15580660.
13. Chopra, I., *Review of state of art of smart structures and integrated systems.* AIAA journal, 2002. 40(11): p. 2145-2187.
14. Li, D.-X. and R. Xu, *Optimal Design and Control of Smart Space Structures: A Memetic Evolution Approach.* Intelligent Systems, IEEE, 2014. 29(1): p. 40-46.
15. Garba, J.A., B.K. Wada, and J.L. Fanson, *Adaptive structures for precision controlled large space systems.* Journal of intelligent material systems and structures, 1992. 3(2): p. 348-366.
16. Jenkins, C.H., *Recent advances in gossamer spacecraft*. 2006.
17. Jenkins, C.H., *Gossamer spacecraft(membrane and inflatable structures technology for space applications).* Progress in Astronautics and Aeronautics, 2001.
18. Gorinevsky, D., T. Hyde, and C. Cabuz, *Distributed localized shape control of Gossamer space structures.* 2001.
19. Sakamoto, H., et al., *Folding patterns of planar gossamer space structures consisting of membranes and booms.* Acta Astronautica, 2014. 94(1): p. 34-41.
20. Miyazaki, Y., et al., *Finite element analysis of deployment of gossamer space structure.* Multibody Dynamics, 2011.
21. Cadogan, D.P. and S.E. Scarborough, *Rigidizable materials for use in gossamer space inflatable structures.* AIAA paper, 2001. 1417: p. 2001.
22. Straubel, M., et al. *Deployable composite booms for various gossamer space structures*. in *52nd AIAA/asme/asce/ahs/asc Structures, Structural Dynamics, and Materials Conference*. 2011.
23. Straubel, M. and M. Sinapius, *Boom concept for gossamer deployable space structures*, in *Adaptive, tolerant and efficient composite structures*. 2013, Springer. p. 237-250.

Dynamic Model Reduction Using Data-Based Loewner-SVD Methods applied to Thermally Morphing Structures

Austin A. Phoenix
United States Naval Research Lab, Naval Center for Space Technology

Serkan Gugercin Pablo A. TarazagaSerkan Gugercin, Pablo A. Tarazaga
Virginia Tech, Vibrations, Adaptive Structures, and Testing Lab
310 Goodwin Hall, Blacksburg, VA, 24060

Abstract: The work herein proposes the use of the Loewner-Singular Value Decomposition (SVD) data-based reduced method as applied to dynamic Finite Element Models (FEM) of thermally morphing structures. This method is computationally efficient and accurately reduces models using analytical output data from a FEM. This paper details the two-step process proposed in the Loewner-SVD approach. First, a random vibration FEM simulation is used as the input for the development of a Single Input Single Output (SISO) data-based dynamic Loewner state space model. Second, an SVD-based model reduction technique is used on the Loewner state space model, such that the minimal, dynamically representative, state space model is achieved. For this, varying levels of reduction are generated and compared. The work herein can be extended to model generation using experimental measurements by simply replacing the FEM output data in the first step and following the same procedure. This method will be demonstrated on two thermally morphing structures, a rigidly fixed hexapod in multiple geometric configurations and a low mass anisotropic morphing boom. This paper is working to detail the method and identify the benefits of the reduced model methodology.

Keywords: Data Based Loewner Method, Model Reduction, FEA, Thermal Actuation, Morphing Systems

1. Introduction

While there are a significant number of FEM model reduction methods proposed in the literature, this method provides an opportunity unattained in currently adopted reduction methods. The Loewner-SVD reduced model can be built with frequency response transfer functions generated using test data rather than the simulated FEM data as is shown in this feasibility study. This provides an additional approach as it removes the requirement to have an accurate predictive model as the baseline for the reduced model generation. The use of test data to produce high-quality predictive models provides significant advantages in model development, model correlation, and test development. This can also have significant benefits when the models are too complicated, time-consuming to develop and/or non-linear in nature. While models have been generated using test data before, using the Eigensystem Realization Algorithm (ERA) [1, 2] for modal parameter identification as well as to identify stiffness and other dynamic structural parameters [3, 4], the method discussed in this paper provides several advantages. The Loewner-SVD method described in this paper is specifically suited to produce dynamic transfer functions. This method provided a platform to develop a reduced model using the Loewner and shifted Loewner matrices without the need to compute the full state space model, allowing for an efficient iteration and reduced scale optimization. The work in this paper is a demonstration and qualification of this method applied to complex modeling applications for a large number of geometries.

The field of model reduction has had important advances, and significant efforts have been placed into forming a generalized model reduction approach [5] as well as specific FEM reduction methods. The reader is encouraged to see [3] for a comprehensive approach to general model reduction. The classic Guyan FEA reduction [6] acts directly on the mass and stiffness matrix removing elements not loaded in the system. System Equivalent Reduction

Expansion Process (SEREP) [7-9] takes advantage of the eigenmodes and eigenfrequencies of the system to provide a reduced model that contains the dynamic behavior of the system. Craig-Bampton [10] methods provide high-quality correlation through the reduction of the Degrees of Freedom (DOF) of the system to only constrained nodes and recovery nodes. Then the constrained eigenmodes and eigenfrequencies are calculated and included in the reduced model to provide a highly accurate dynamic model. This method provides a simple method to reduce the number of DOF in a complex system to only the DOF of interest, but these methods require the use of the full mass and stiffness matrix of a FEM. While this method can be used for FEA reductions, the purpose of this paper is not to provide a more efficient FEM reduction method, but to demonstrate a new versatile tool that can be implemented to reduce FEM as well as generate reduced models in the case where a model does not exist.

This paper details the implementation of the Loewner-SVD data-based model reduction method through its application to two separate structures under single axis, random vibration excitation. The reduced model of interest is a representative SISO model in the bandwidth of 20 to 2000 Hz for the hexapod and anisogrid geometries shown in Fig. 1 and Fig. 3, respectively. The Loewner-SVD model generates a state space model of size $n \times n$, where n is the length of the frequency response functions (FRF) output by the FEM. This $n \times n$ model is subsequently reduced using an SVD truncation methodology. For all geometries, multiple truncation points are evaluated to study the scale and accuracy of the reduced models as a function of geometric input parameters. The reduced model serves as a dimensionally smaller system on which to optimize the dynamic structural configuration. With this in mind, a parameter sweep of 125 unique hexapod geometric cases is developed, and a reduced model is created for all 125 dynamic responses as a parametric analysis on the reduction methodology. An investigation is done to identify the geometric effects on the quality of the various model reduction sizes. The goal of this study is not the development of a parameterized model reduction as seen in [11] but rather to evaluate the Loewner-SVD method. A single anisogrid geometric configuration is evaluated to demonstrate the method on a system with more complex geometry and dynamic response.

To justify the computational cost of using FEM inputs to develop a Loewner-SVD data-based model the system must be subjected to a high number of dynamic loading cases. Otherwise, the cost of reduced model development could exceed the cost of multiple full FEM calculations. However, this method provides significant benefits when used in conjunction with test data by reducing testing configurations and by generating accurate models in cases where the geometries or test cases are difficult to accurately capture.

The paper provides an introduction to the model generation, reduction method, the structures of interest, and the resulting FEM development. Likewise, the paper discusses the reduced hexapod geometry and the accuracy as a function of the geometric parameter inputs and resulting model scale. An investigation is completed on the anisogrid structure to demonstrate the ability to produce a reduced model using more complex dynamic systems. Finally, the methodology and results are summarized.

2. Structural Modeling and FEM

Thermally actuated morphing structures are researched in an attempt to build and provide high precision deflection capabilities that are not possible using conventional means. The Naval Research Lab has been heavily invested in lightweight adaptive structures as well as high fidelity morphing applications such as the structure investigated here specifically for space applications. The use of thermal strain as the actuation mechanism has been studied at the micro [12-17] and macro level [18], but the use of standard materials applied on the micro scale to enable high precision morphing is a novel investigation. This paper looks to advance the field of structural modeling by developing modeling methods that reduce the overall complexity and allow for easier model optimization while maintaining accurate dynamic behavior.

The classic hexapod geometry is a parallel robot with six actuators providing six DOF morphing control. The first hexapod geometry, also called a Stewart platform, was presented in 1965 [19] by D. Stewart for flight simulators. In recent years significant effort has been put into structural optimization [20] and workplace optimization [21-23].

Further work has been the development and implementation of the Hobby-Eberly Telescope morphing structures [24-26]. These structures provide the baseline for the development of the thermal morphing hexapod. The thermal morphing hexapod structure allows for the development and evaluation of the tools required for this system in a system that is simple enough yet representative to carry out parametric iterations. A secondary, more complex thermal morphing system of interest is the anisogrid boom which is more indicative of the leading edge in ultra-lightweight thermally morphing structures, but its complexity limits a thorough parametric analysis. Here the anisogrid structure is used to test the methodology on a highly complex system.

Anisogrid tubular structures have shown great promise in structural applications where a lightweight structure is of critical importance [27-34]. These systems provide significant potential for reduced mass structural applications, specifically in the large space structures field. Similarly to the thermal morphing hexapod structure the anisogrid structure has the potential for high-performance thermal morphing applications. The anisogrid structure will be used as a demonstration of the method on a complex dynamic system. Before the dynamics of the full design space for the highly complex anisogrid morphing system can be understood, the dynamics of the simpler hexapod system need to be investigated.

Given the complexity of these structures, the purpose of this reduction is to provide an efficiently reduced model to use for dynamic structural optimization. The key design characteristics for optimization are the geometric parameters listed in Table 1 for the hexapod and the anisogrid system. The full design space for the hexapod system is investigated through the evaluation of 125 geometries. To generate those 125 geometric cases, the three geometric parameters (L1, L3, and Z) are swept between 2.5 and 30cm (2.5, 9.375, 16.25, 23.125 and 30 cm). For the Anisogrid system, there are 11 parameters of interest for the structural optimization. This paper will not investigate the full design space of the anisogrid system and instead will demonstrate the approach on a single anisogrid geometry. Extension of this work could lead to the generation of the optimization tools for the anisogrid structure presented here.

Table 1 Geometric parameters of interest for each thermal morphing structure.

Hexapod	**Anisogrid**
Length 1	Height
Length 3	Pitch
Height	Hel Cross Section 1
	Hel Cross Section 2
	Cir Cross Section 1
	CirCross Section 2
	# of Helicals
	Base Radius
	Tip Radius
	Modulus
	Fixity

2.1 Hexapod Structure

Kinematic morphing hexapods classically consist of two parallel plates connected using six linear actuators. The actuators are connected using a pinned-pinned boundary condition on either plate as shown in Fig. 1. The thermally actuated hexapod concept is a novel variation on the classic design where a hexapod is connected using fixed-fixed rigid struts where global and local thermal gradients are applied as the actuation mechanism. The thermal gradients provide individual strut actuation to obtain six degrees of freedom high precision control. The investigation into the hexapod will only focus three critical parameters, L1, L3, and Z, which define the geometry. Other parameters such as beam cross section are held constant for this investigation. These three parameters of interest, L1, L3 and Z define the bottom plate size, top plate size, and the height of the system, respectively. To investigate the design space, each of the three parameters is swept through five values resulting in a total of 125 different hexapod geometries. Following this, an FEM and consequently a reduced model is generated for each geometry case.

MSC Nastran dynamic solution set 111 is used to model the hexapod structures under an X-axis random vibration excitation, with a flat input of 1.25e-4 G^2/Hz from 20 to 2000 Hz measured at 1181 frequency points. The center node of the active platform is "measured" and the X-axis input and platform response is used as the output for the SISO model. The Hexapod model in Fig. 1 contains 56 nodes with 51 linear beam elements and a total of 336 independent degrees of freedom, resulting in a stiffness and mass matrix that is 336 × 336. The top plate and bottom plate in Fig. 1 (b) and (c) are represented by a rigid element ensuring coupled responses of the top and bottom interfaces

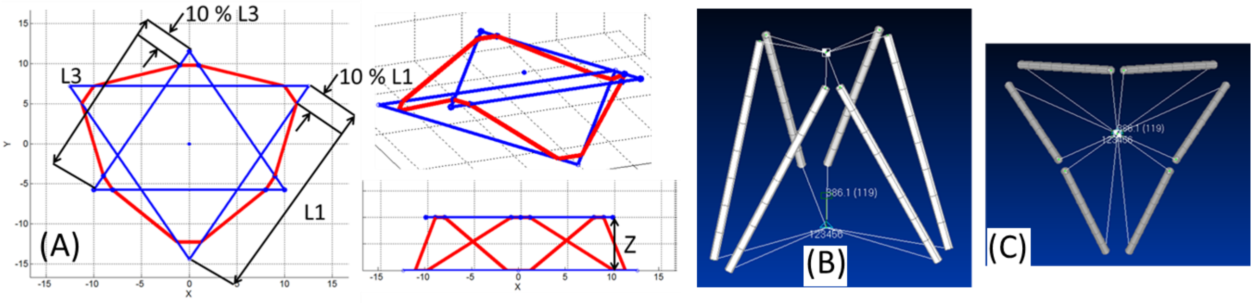

Fig. 1 (A) Detail of the Geometric Parameters for the Hexapod (L1, L3, and Z). (B) FEM developed for a given geometry case. (C) Top View of FEM

The resulting dynamic analysis shows 72 modes in the frequency range of interest for a nominal geometry. Five of the representative modes are shown in Fig. 2. The length of each of the three parameters is set to every possible combination of 5cm, 11.25 cm, 17.5cm, 23.75cm, and 30cm. To ensure accurate modeling, a convergence study demonstrated that the FEM is appropriately sized. This structure functions as an appropriate test bed to evaluate the method proposed herein but does not produce an oversimplification in complexity such that the structure is no longer representative. Furthermore, the base building block for the six helical anisogrid is a hexapod configuration lending itself to further evaluation. To obtain a deeper understanding of the geometry and the reduction capability of the proposed technique, the more complex anisogrid structure is also investigated and described in the following section.

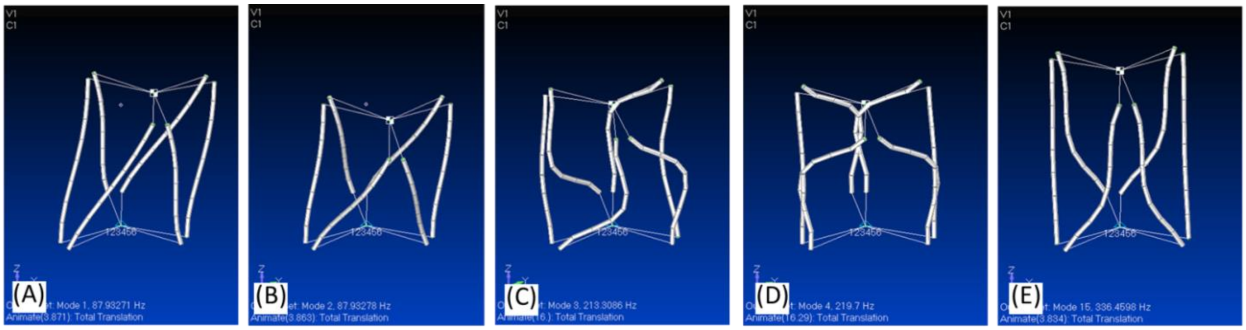

Fig. 2 (A) Mode 1 at 15 Hz,(B) Mode 2 at 87.9 Hz, (C) Mode 3at 87.9 Hz, (D) Mode 4 at 213 Hz, (E) Mode 15 at 336 Hz.

2.2 Anisogrid Structure

The morphing anisogrid model reduction operates on the same methodology as the hexapod with local and global thermal gradients providing the anisogrid structure the required actuation strain to achieve high precision morphing. The anisogrid model of interest is 1.0 meters tall with a 0.25-meter radius. MSC Nastran dynamic solution set 111 is used to model the anisogrid structure under an X-axis random vibration excitation, with a flat input of 1.25e-4 G^2/Hz from 20 to 2000 Hz measured at 1181 frequency points. The top center node, located at Z = 1 of the active platform, is "measured" and the X-axis input and response is used as the output for the SISO model. The anisogrid model seen in Fig. 3 contains 1,712 nodes with 1,889 elements and 10,272 independent degrees of freedom resulting in a stiffness and mass matrix that is 10,272 × 10,272. The reduced model will provide a reasonable measure of the ability of this approach to reduce a complex dynamic model while still conserving the dominant dynamics of the system.

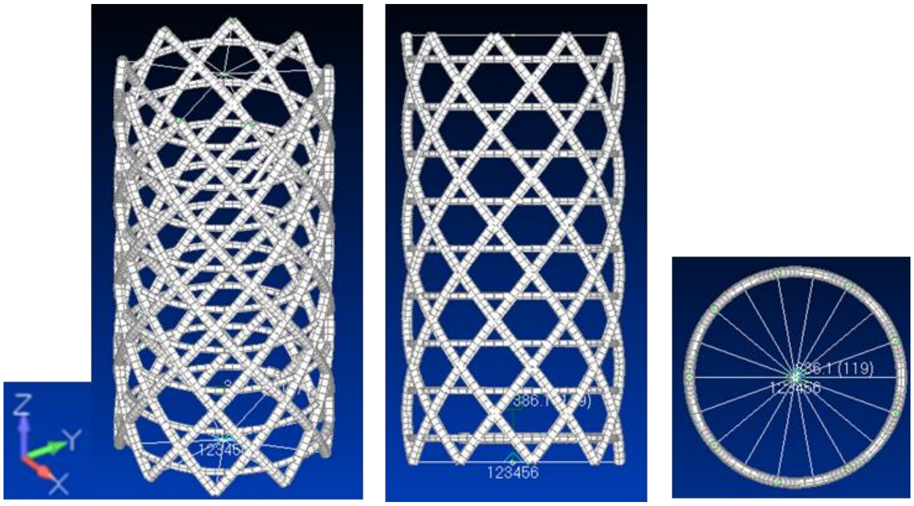

Fig. 3 Anisogrid, 1 meter tall with a .25 meter radius, FEA Model requiring 1889 Elements.

The anisogrid structure has 213 modes in the frequency range of interest as compared to the 72 modes for the baseline hexapod geometry. The increase in structural complexity requires a significant increase in modeling effort from 336 DOF to 10,272 to capture all of the dynamics in the FEM. A representative segment of the modal content of the anisogrid structure is shown in Fig. 4. This structure was chosen specifically to act as a baseline to evaluate the methodology on more complex structures so that the reduced model scale and quality can be assessed.

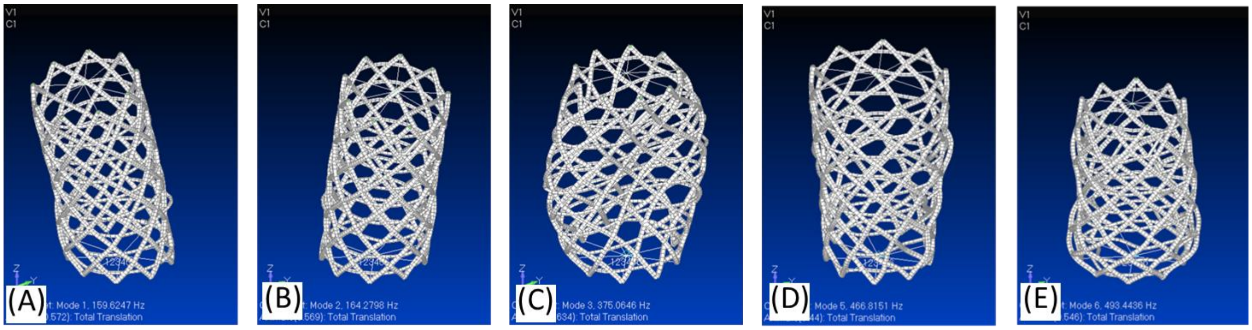

Fig. 4 Select modes of the anisogrid structure: Mode 1, 2, 3, 5 and 6 at160, 164, 377, 466 and 493 Hz, respectively.

3. Loewner-SVD Model Reduction Development and Implementation

The Loewner matrix and the shifted Loewner matrix used in this work are detailed in the literature as the divided-difference matrix and the null-pole coupling matrix used for solving rational interpolation problems [35]. This method is an efficient Hermite interpolation method that can generate a state space model from a given set of frequency response functions. The Loewner matrices' application for time and frequency domain interpolation has been heavily researched in [36] and [37]. The application of interest is the data-based approach model reduction applied to the state-space Loewner matrices that are obtained from an FEM via simulated frequency response functions. Notice that the method can be extended in a straightforward manner to actual experimental data instead of the simulated frequency response functions used in this study. These simulated or experimental generated FRF's are used to produce the Loewner-SVD Data-based model. The use of the generalized Loewner method itself is not a reduction, but rather generates a model in a state space form such that model reduction methods can be applied to it. In this study, an SVD model reduction approach is applied to generate the reduced model. This process is detailed in Fig. 5.

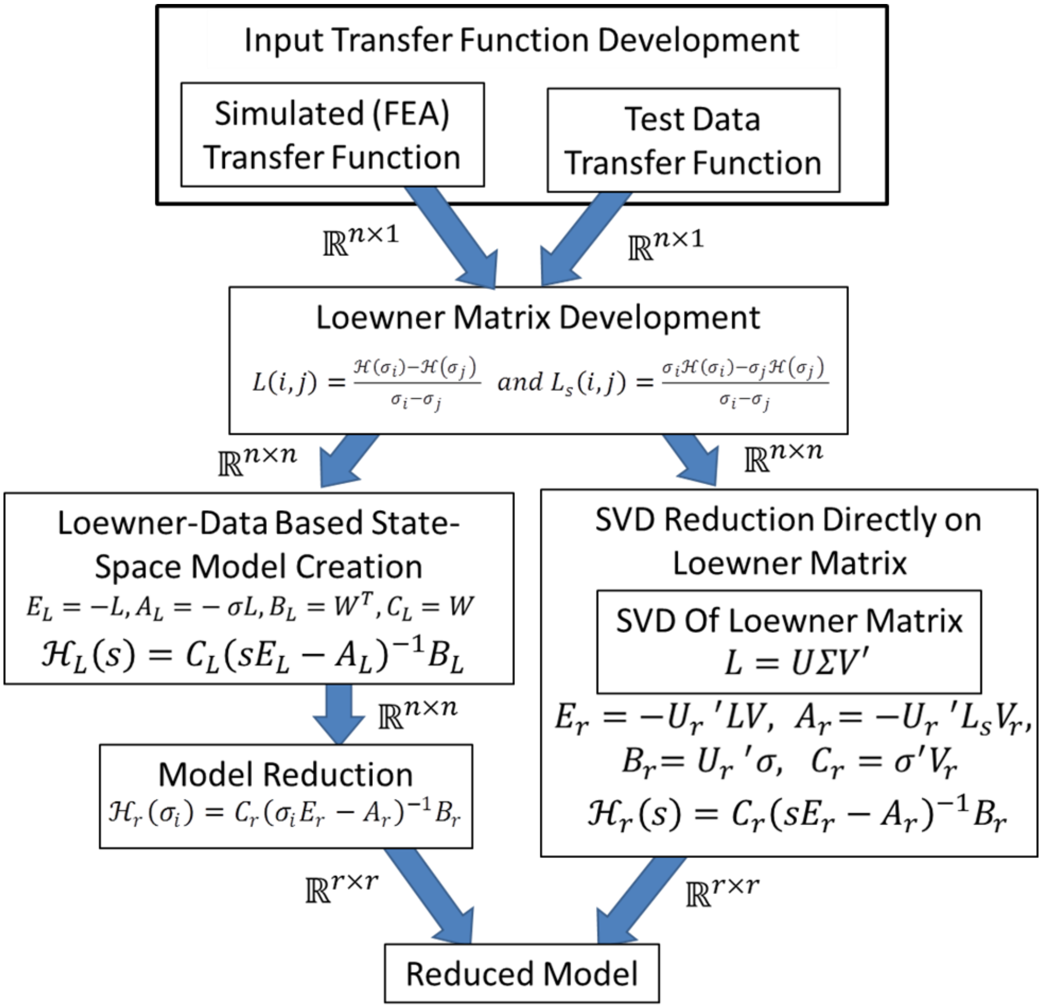

Fig. 5 Methodology framework development using FEA transfer functions or experimental data followed by an SVD model reduction method to achieve a dynamically relevant reduced model.

As is detailed in Fig. 5, one of two input transfer functions (FEA or test data) is used to develop the Loewner-SVD, state-space model. The resulting model is reduced using an SVD model reduction approach resulting in a reduced model of scale *r*. This paper evaluates the capabilities of the method as applied to the two morphing configurations described previously and 126 individual FEMs. The intent is to detail the implementation of a standard SISO interpolation model reduction problem using FEM outputs as the input transfer function.

3.1 Data Based Loewner-SVD Method

The method used here, covered in depth in [38] and briefly included here for completeness, requires solving the generalized realization problem. The problem requires transfer matrix evaluations $\mathcal{H}(\sigma_i)$ and $\mathcal{H}'(\sigma_i)$ from a linear system, to construct a state space model that is controllable and observable. For this evaluation, a FEM is used to develop the transfer function at 1181 frequency points as described in the previous section. This formulation takes advantage of the symmetric Loewner (L) and shifted Loewner (L_s) matrices and creates a state space model using a Hermite Interpolate σ_i evaluated at $\sigma_1 \ldots \sigma_n$ as detailed in [39]. The Hermite Interpolation ensures that generated transfer functions match the FEA transfer function both in value and in slope at the chosen interpolation points. Those 1181 frequency points, defined in the FEM, are then used as the interpolation points to develop the full Loewner matrix. The full Loewner matrix transfer function is calculated in the form as

$$\mathcal{H}_L(\sigma_i) = C_L(\sigma_i E_L - A_L)^{-1} B_{L\,,} \tag{1}$$

$$where\ A_L, E_L \in \mathbb{R}^{n\times n}, B_L \in \mathbb{R}^{n\times m}, C_L \in \mathbb{R}^{p\times n}\ , \tag{2}$$

where σ_i is the i^{th} interpolation point. For this single input single output case m=p=1 and n = 1181 resulting in a SISO system evaluated at 1181 points. To develop the Loewner and shifted Loewner matrix, projection matrices are required. The projection matrices V and W are developed from the FEM transfer function evaluated at the n frequency values as

$$W = [\,\mathcal{H}(\sigma_1), \dots, \mathcal{H}(\sigma_n)],\ V^T = [\,\mathcal{H}(\sigma_1), \dots, \mathcal{H}(\sigma_n)]\ , \tag{3}$$

$$where\ W, V^T \in \mathbb{R}^{1\times n} \tag{4}$$

moreover, the Loewner Matrix and shifted Matrix can be defined as

$$L(i,j) = \frac{\mathcal{H}(\sigma_i) - \mathcal{H}(\sigma_j)}{\sigma_i - \sigma_j}\ \text{if i} \neq \text{j, and if i = j,}\ \ L(i,i) = \mathcal{H}'(\sigma_i) \tag{5}$$

$$L_s(i,j) = \frac{\sigma_i\mathcal{H}(\sigma_i) - \sigma_j\mathcal{H}(\sigma_j)}{\sigma_i - \sigma_j}\ \text{if i} \neq \text{j, and if i = j,}\ \ (i,i) = \sigma_i\mathcal{H}'(\sigma_i)\quad \text{where}\ L\ and\ L_S \in \mathbb{R}^{n\times n}. \tag{6}$$

The conversion back to the state space transfer function is given by

$$E_L = -L, A_L = -\,\sigma L, B_L = W^T, C_L = W \tag{7}$$

The resulting full Loewner matrix is sized 1181 × 1181 and the transfer function $\mathcal{H}(s)$ perfectly represents the FEM at all frequencies used for interpolation. This results in a perfect correlation between the full Loewner matrix and the FEM at all the frequencies evaluated in the FEM. For this investigation the SVD truncation reduction, explained in the following section, is used to produce a reduced state space model.

4. SVD Model Reduction

As noted previously, the state space matrices obtained via the Loewner method result in a system of equations of size n × n, where n is the number of frequency values used as interpolation points. For this case, the method results in an 1181 × 1181 Loewner matrix and subsequent Loewner state space model. As discussed in [40] the SVD-based reduction is an appropriate method for the evaluation of this problem. To define the appropriate truncation point r, an SVD analysis is performed and plotted for all the hexapod geometries as shown in Fig. 6. In the same manner, the decomposition for the anisogrid structure is shown in Fig. 12. The scale of the SVD value provides the insight used to choose the reduced model size that balances reduction efficiency and model accuracy. This method is straightforward to implement and simple to test multiple r values to find the optimally reduced model. Once the reduction scale is chosen from the SVD investigation, it is not necessary to generate the full Loewner State Space model in Eqn. 7, rather the reduced model can be developed directly from the Loewner matrix as

$$\mathcal{H}_L(\sigma) = C_L(\sigma E_L - A_L)^{-1} B_L \tag{8}$$

where the Loewner transfer function is exactly equal to the FEM transfer function at the interpolation points

$$For\ i = 1{:}\,r\ \ \mathcal{H}_L(\sigma_i) = \mathcal{H}_{FEA}(\sigma_i)\ . \tag{9}$$

The reduced model $\mathcal{H}_r$ can be developed by preforming the SVD on the Loewner matrix

$$L = U\Sigma V'\ . \tag{10}$$

Once the SVD is completed on the Loewner matrix, the singular vectors can be truncated at r resulting in a reduction of the left singular vectors $U \in \mathbb{R}^{n\times n}$ to produce $U_r \in \mathbb{R}^{n\times r}$and a reduction in the right singular vectors $V \in \mathbb{R}^{n\times n}$ to produce $V_r \in \mathbb{R}^{n\times r}$. These reduced singular values are used, in conjunction with the left and right singular matrices, to develop the reduced model as,

$$E_r = -U_r{}'LV,\ \ A_r = -U_r{}'L_sV_r,\ \ B_r = U_r{}'\sigma,\ \ C_r = \sigma' V_r\ . \tag{11}$$

Reconstruction of the transfer function using the reduced state space model produces

$$\mathcal{H}_r(\sigma_i) = C_r(\sigma_i E_r - A_r)^{-1}B_r\ \ . \tag{12}$$

This method provides the opportunity to efficiently generate reduced state space models using FEM or test data as the primary input. It also demonstrates the ability to test with ease multiple reduced model sizes by increasing or reducing r to ensure that optimally reduced models are generated. To evaluate the quality of the resulting reduced model, a relative error e is calculated between the FEM and the reduced model. The FEM and reduced model transfer function is evaluated at all 1181 frequency points. The H_2 norm of the difference between the two transfer functions is used to evaluate the reduced model error as seen in Equation 12.

$$e = |H_{FEA} - H_r|_2 \tag{13}$$

To define the optimally reduced model multiple r values are used to balance accuracy and computational efficiency. For the hexapod and anisogrid geometries, accurate models, detailed in the next section, where achieved using the SVD reduction method. For a system with orders of magnitude increased complexity, the generation of the highly reduced and well-correlated models may require a more advanced reduction method than SVD. Particular cases are examined to bring attention to some of the intricacies of the method and the dynamical response.

5. Hexapod 125 Case Model Reduction

To better understand the dynamic behavior of the reduced models and how they are affected by the truncation a process, multiple reduction models are generated for each of the 125 hexapod structure configurations. As seen in Fig. 6, there is a significant variation in the hexapod geometries' singular value decay resulting in different optimal reduction scales for individual geometries. Overall, these geometric variations indicate that no single r value will provide an optimally reduced model for all the geometries of interest. This is to be expected as a generalization across multiple dynamic behaviors due to geometric changes should not be expected. Having said that, there is a general trend that can be exploited if necessary.

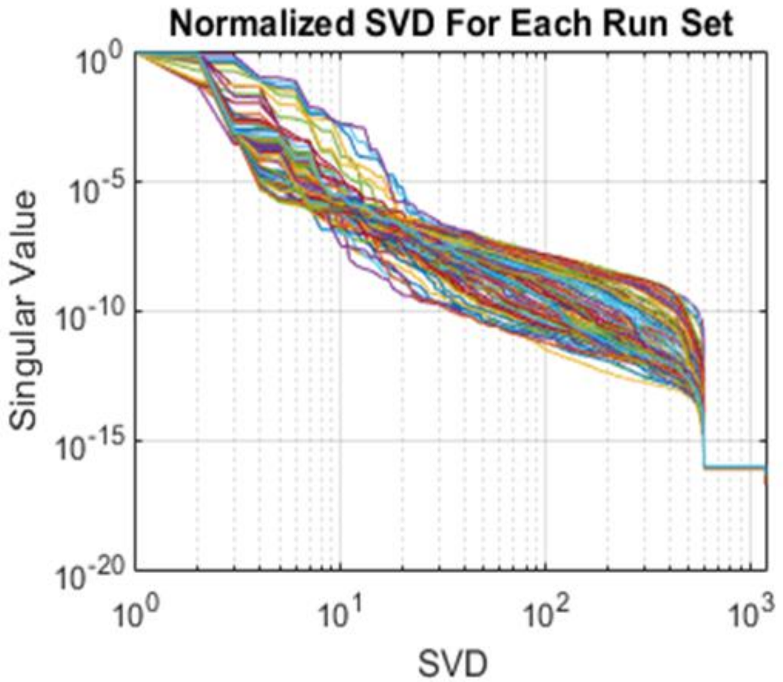

Fig. 6 The normalized singular values for all 125 hexapod configurations.

The investigation into the resulting max and minimum error provided by the H_2 norm for all hexapod geometries demonstrates the variability in the reduced model accuracy as a function of reduction scale. The results of this study can be seen in Table 2 for several discreet reduction values. This is carried out to provide insight into the geometric parameters' impact on system dynamics and define a method to determine the optimal r value for each geometry.

Table 2 Comparison of Max and Min H_2 norm for all runs

	H_2 Norm for all 125 Hexapod Geometries				
	r = 10	r = 15	r = 30	r = 45	r = 60
Max For all Geom.	1.09	5.54E-01	1.12E-01	7.31E-01	2.56E-02
Min For all Geom.	6.98E-05	1.06E-05	5.80E-07	1.70E-07	2.30E-07

The geometries that were chosen provide an opportunity to evaluate the variety of correlation accuracies given a range of the Loewner-SVD model reduction sizes. We can see that in Table 2, a sufficiently accurate model is obtained for all geometries with a given reduction of r = 15. To better understand the FRF responses generated from a variety of H_2 norm error comparison, six representative geometries are evaluated in Fig. 7.

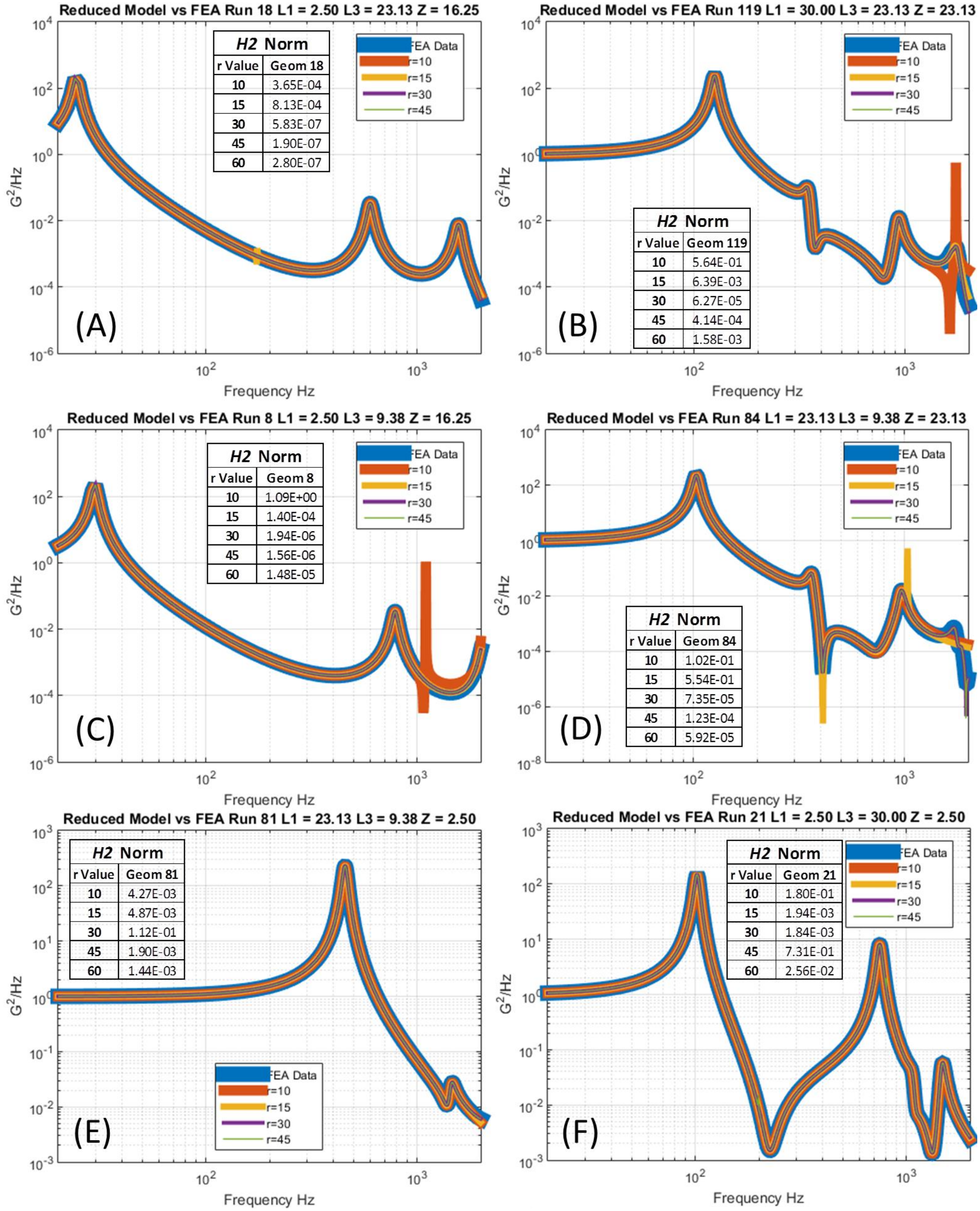

***H2* Norm**

r Value	Geom 18
10	3.65E-04
15	8.13E-04
30	5.83E-07
45	1.90E-07
60	2.80E-07

***H2* Norm**

r Value	Geom 119
10	5.64E-01
15	6.39E-03
30	6.27E-05
45	4.14E-04
60	1.58E-03

***H2* Norm**

r Value	Geom 8
10	1.09E+00
15	1.40E-04
30	1.94E-06
45	1.56E-06
60	1.48E-05

***H2* Norm**

r Value	Geom 84
10	1.02E-01
15	5.54E-01
30	7.35E-05
45	1.23E-04
60	5.92E-05

***H2* Norm**

r Value	Geom 81
10	4.27E-03
15	4.87E-03
30	1.12E-01
45	1.90E-03
60	1.44E-03

***H2* Norm**

r Value	Geom 21
10	1.80E-01
15	1.94E-03
30	1.84E-03
45	7.31E-01
60	2.56E-02

Fig. 7 Model Responses for a representative set of geometries for various error bounds for Geom. 18 (A), Geom. 119 (B), Geom. 8 (C), Geom. 84 (D), Geom. 81 (E), and Geom. 21 (F).

The reduced dynamic model for geometry 18 (L1 = 2.5 (cm) L3 = 23.13 (cm) Z = 16.25 (cm)) demonstrates a high correlation for all *r* values as shown in Fig. 7 (A). Geometry 119 (L1 = 30 (cm) L3= 23.13 (cm) Z= 23.13 (cm)) and geometry 8 (L1 = 2.5 (cm) L3 = 9.38 (cm) Z = 16.25 (cm)) shown in Fig. 7 (B) and (C) respectively, are the maximum error cases for *r* = 10. It can be seen that despite the high H_2 norm error the dynamics of the system with *r* = 10 are accurate below 1000Hz. Above 1000 Hz, where the accuracy of the FEM is greatly diminished, the reduced model does not accurately predict the dynamics of the system. This is an important finding indicating a frequency dependent accuracy that can be exploited for applications with lower frequency range requirements. The maximum error case for *r* = 15 demonstrates an error introduced in the prediction of the high-frequency modal responses for geometry 84 (L1 = 23.13 (cm) L3 = 9.38 (cm) Z = 23.13 (cm)), shown in Fig. 7 (D). Shown in Fig. 7 (E), geometry 81 (L1 = 23.13 (cm) L3 = 9.38 (cm) Z = 2.5 (cm)) is the maximum error case for *r* = 30. As can be seen geometry 81, the max error case, produces an accurate prediction with the use of *r* =30 demonstrating the quality of all reduced models using *r* = 30. As the scale of the model increases to *r* = 45 the maximum error, found in geometry 21 (L1 = 2.5 (cm) L3 = 30 (cm) Z = 2.5 (cm)), shows a high-quality frequency response plotted in Fig. 7 (F) that cannot even be perceived by observation.

Based on this study, the *r* = 30 model would be chosen for all geometries based on the resulting balance between model errors and the scale of the model. If high-frequency responses are not of interest, smaller order models could provide sufficient accuracy in the frequency range of interest. For a model with a reduced bandwidth of interest, a truncation of the frequency range used to develop the reduced model could reduce the model further without introducing errors in the frequency range of interest. .

This study has shown that the primary shortcomings of concern with this methodology are that the system has the potential to ignore (i.e., Fig 7. D last mode for *r* =10,15) or introduce modes (i.e., Fig 7 C) if the model does not have a representative size to model all relevant dynamics. This method has been shown to develop accurate, reduced, state-space models of order *r* = 30 for all of the studied geometries with some of the representative responses are shown in Fig. 7. This has produced accuracies well within the needs of this system while minimizing the model complexity. The mythology proposed herein has been shown to keep the relevant dynamics while reducing the system by 91% (original FEM model 336 DOF to a reduced Loewner-SVD system with *r* = 30).

6. Results as a Function of Geometric Input Parameters

To better understand the cause of the variation in reduced model quality an investigation was conducted into the variations caused by the geometric inputs. To evaluate this, several key metrics are investigated and plotted against the geometric inputs. The error provided by the H_2 norm as a function of geometry and the reduced model size is evaluated to provide better insight into the hexapod design space. An investigation into the H_2 norm error for all 125 geometries is presented in Fig. 8 (A). It can be seen in Fig. 8 (A) that there is a general trend of reduced H_2 norm error as *r* increases, but this does not hold for all geometries or reduced model scales. To better understand the H_2 norm error as a function of geometric inputs, the accuracy is evaluated as a function of the geometric inputs for reduced model sizes 10, 15, 30, 45 and 60 in Fig. 8 (B) through Fig. 8 (F).

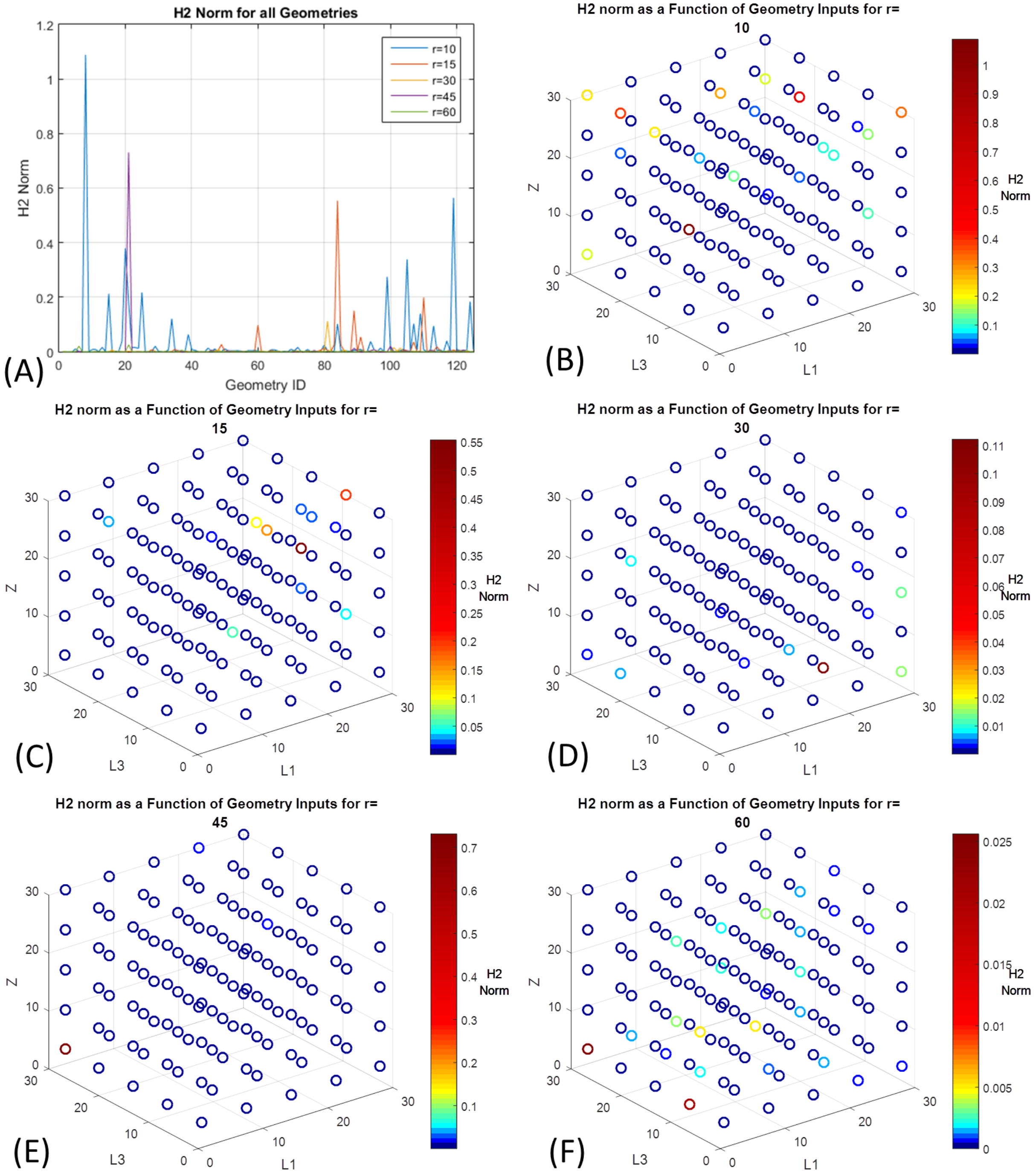

Fig. 8 Impact on H_2 norm for increasing r values for all 125 geometries (A), Response as a function of geometry for r=10 (B), r=15 (C), r=30 (D), r=45 (E), r=60 (D)

While it is difficult to identify the quality of the resulting models based on H_2 norm error alone as seen in Fig. 8 it can be seen that generally, the models get better as the reduced model increases in size. That trend of decreased H_2 norm error when r increases does not hold for individual geometries but is shown to hold generally as seen in Fig. 9.

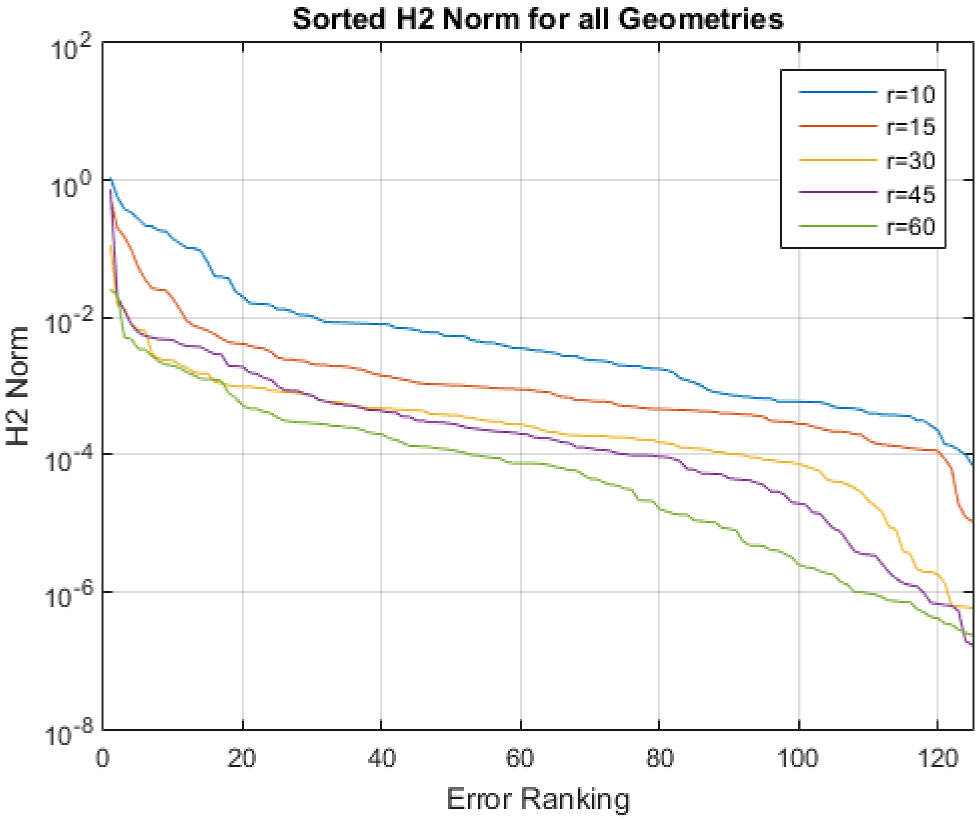

Fig. 9: Sorted error rankings for all reduced hexapod models.

As is demonstrated in Fig. 9 the sorted error for each reduction size highlights the trend where increased model size reduces the $\boldsymbol{H_2}$ norm. The key point is that this does not hold for specific geometries but the overall trend is true. To define an optimal model size for all geometries is not possible. That being said, overall increased model size generates reduced H_2 norm error as is demonstrated in Table 2 and Fig. 8(A).

To better quantify the dynamic model reduction capability, relative to geometric inputs, the H_2 norm errors for each reduced model scale is summed and evaluated in Fig. 10 (A). It can be seen, when compared to Fig. 8 (A), that the large errors are driven by a single outlier in the reduced model size. By investigating the resulting model quality as a function of geometric inputs, seen in Fig. 10 (B), it can be seen that no single region of the design space performs poorly. However, it can be observed that the larger errors are located at the extremes of the design space. This finding provides information about geometries with lower dynamic complexity and more accurate model generation.

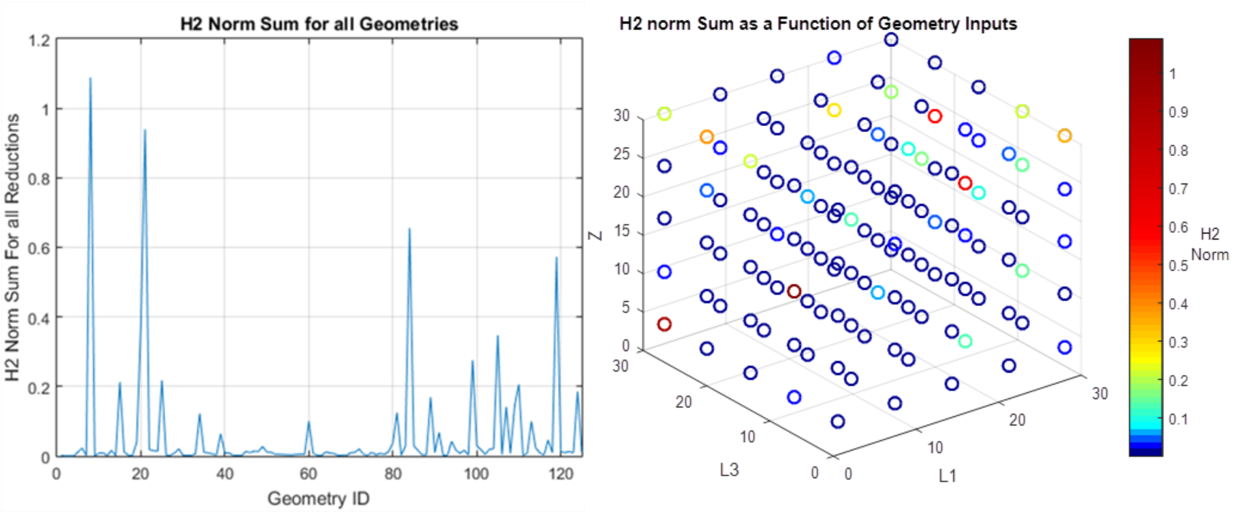

Fig. 10 (A) Sum of the Five Reduced Models H_2 Norm (B) Sum as a function of Geometric Inputs

Now that the resulting reduction quality has been evaluated as a function of the input geometry, a study into the reduced models minimum singular value is performed to gain insight into the resulting dynamics of the geometry and the reduced models. The SVD is first evaluated for each geometry at each model reduction size as demonstrated in Fig. 11 (A). As can be seen, models with r = 10 result in a truncation at the 10th singular value have large remaining singular values. As can be seen in Fig. 11 (A) the singular value drops off significantly for these models as r is increased to 30. To further investigate this, a plot demonstrating the singular values for each of the five reduced scales as a function of each geometric parameter is shown in Fig. 11 (B) through Fig. 11 (F).

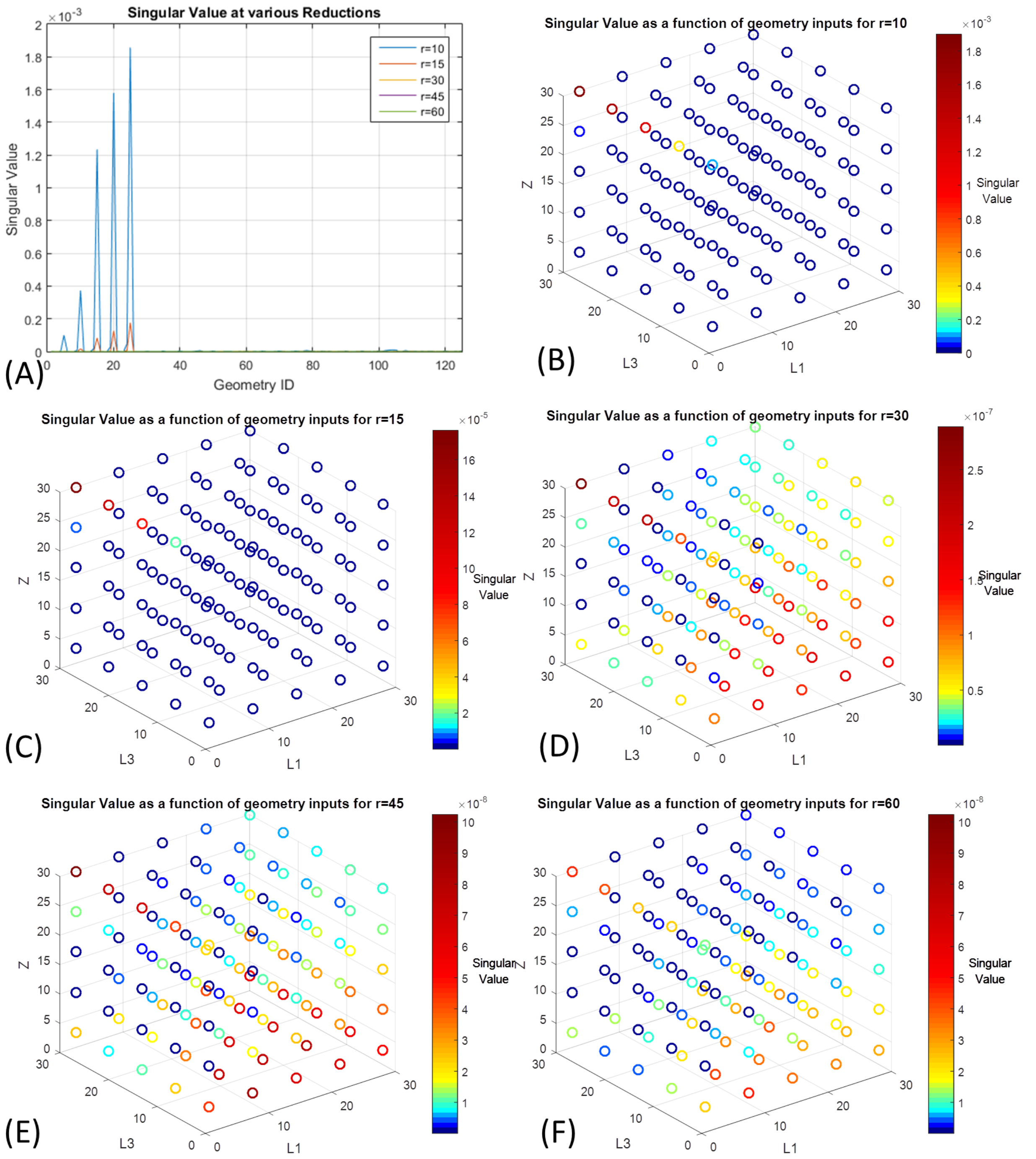

Fig. 11 Investigation into the rth Singular Value for various reductions and all 125 Geometries (A), for *r* =10 (B), for *r* =15 (C), for *r* =30 (D), for *r* =45 (E), for *r* = 60 (F).

The expected response of this system would be that the larger the individual geometric parameters are (L1, L3 and Z), the lower the frequencies and, therefore, the more modes in the frequency range of interest. This increase in dynamics in the range of interest would be expected to increase the singular values at all truncation points. In this case, it can be seen that the maximum singular values do not occur when L1, L3, and Z are at their largest value, but instead, there are two regions where larger singular values are seen. Looking at the responses seen in Fig. 11 (B) and Fig. 11 (C) the peak singular value occurs when L3 and Z are at their maximum and L1 is at its minimum. This is indicative of an unexplained complexity in the dynamics of this geometric case. In Fig. 11 (D) through Fig. 11 (F) it can be seen that a secondary region of high singular values develops. This region occurs when L3 and Z are minimized at a range of L1 values. These regions are indicative of locations in the design space with complex dynamics. These regions provide insight into regions of the design space that need to be investigated further to improve the understanding of the local dynamics.

7. Anisogrid Model Reduction

Using the same methodology applied to the hexapod geometries, the anisogrid FEM is evaluated using multiple reduced models. To quantify the scale of the reduced anisogrid model, the singular values of the Loewner matrix were plotted in Fig. 12. By observing the decaying singular values, there does not seem to be a clear cut-off section where the reduction scale should be set. Although r = 600 could be a possible cut-off condition, it is expected that a considerably smaller system can be found which is representative. For this reason, a study is carried out on the size of the reduction r and the resulting accuracy is compared to the full FEM.

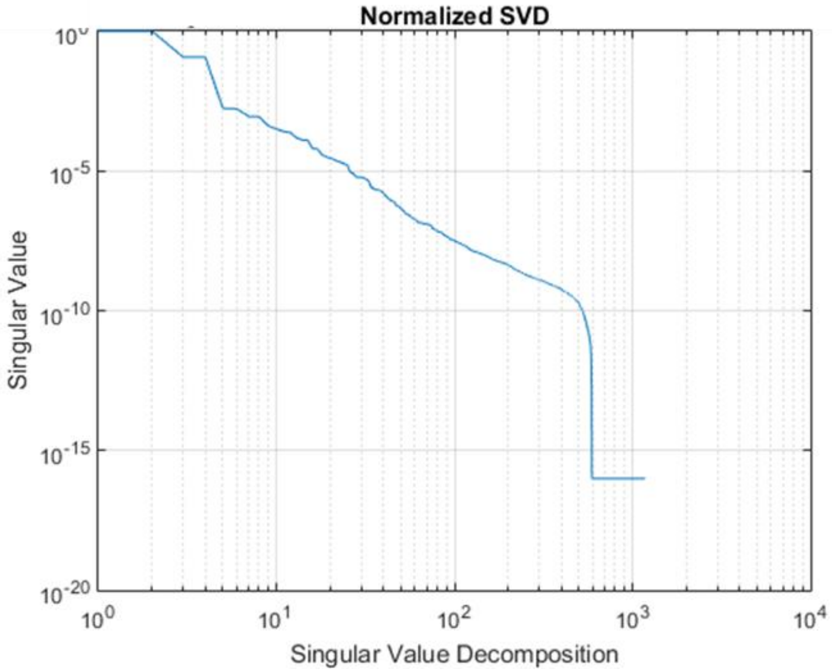

Fig. 12 Anisogrid normalized singular values.

A frequency domain comparison of the dynamics needs to be completed to ensure that the modes of interest and the dynamics of the system are being captured in the bandwidth of interest. Compared to the hexapod, the anisogrid decay of the singular values is much slower. This drives the use of larger r values to ensure the dynamics of the system are captured. To study these effects r = 10, 15, 30, 45, 60, and 75 are considered to investigate larger reduced models for this more complex system.

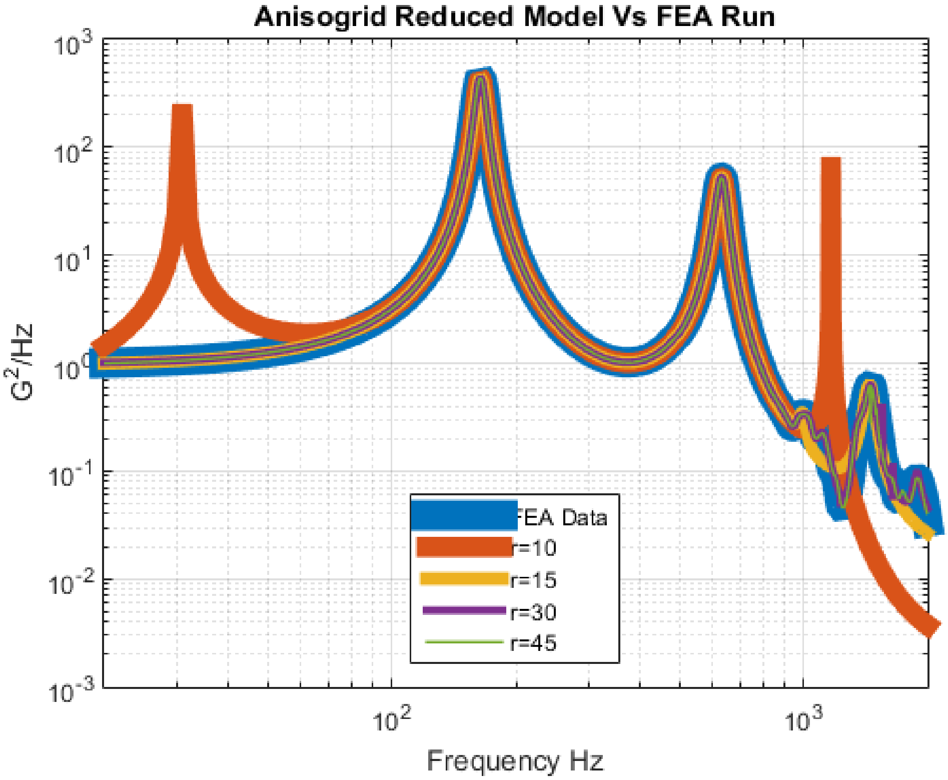

Fig. 13 Anisogrid Response Predictions compared to FEA response.

As previously carried out the response of the system is plotted against the full FEM model fore comparison. As seen in Fig. 13, the reduced model with r = 10 produces an unrepresentative dynamic response and introduces non-real responses to the system's dynamic not present before. A reduction using r = 15 does not have the ability to model the structural dynamics over 1000 Hz and misses critical dynamic behavior at the high-frequency range. As the reduced model increases in scale to r = 30, the system dynamics are matched, and the high-frequency dynamics are modeled with relatively good accuracy. From the H_2 norm error shown in Table 3 and the qualitative FRF comparison, it can be seen that for r = 30 the model produces a high correlation between the reduced model and the FEM. This reduced model is capable of capturing all the dominant dynamics of the system in the bandwidth of interest. This approach successfully reduces the 10,272 × 10,272 FEM model to a 30 × 30 state space model with accurate predictive capability.

The dynamics of the anisogrid structure and its 213 modes can be reduced to a model of size 30 × 30 with a resulting H_2 norm error of 3.02×10^{-1}. Table 3 details the reduction size and its corresponding H_2 norm error for the other reductions cases. Increasing r beyond r = 30 does not significantly reduce the H_2 norm, thus, it can be confidently stated that balance between accuracy and reduced model size is achieved for this geometry using a value of r = 30. This result proves the reduction capabilities of this method on highly complex structures and provides a basis for future work on data based Loewner-SVD model reduction methods.

Table 3 H_2 norm for all r value choices for multiple frequency Ranges

	H_2 Norm for Anisogrid Structure					
	r =10	r =15	r =30	r =45	r =60	r =75
H_2 Norm	2.65E+02	6.64E-01	3.02E-01	3.75E-01	2.30E-03	1.38E-02

Conclusions

This paper has shown that a Loewner-SVD data based model reduction approach can be used to model complex dynamical systems accurately. Through a computationally efficient method, the work has shown the ability to iterate and generate a large number of reduced models while retaining high modeling accuracy. This paper has demonstrated the reduced model development methodology using a FEM transfer functions and provided the opportunity for test data based reduction by following the same procedure. An investigation was performed on the hexapod geometry providing insight into the system dynamics as a function of geometry and yielding an optimal reduced order evaluation.

For the hexapod system, five reduction sizes are applied to 125 geometries resulting in 625 individual reduced models were generated allowing for an optimally reduced model while balancing accuracy and reduce model size. Through this investigation, it was determined that the trend of decreased H_2 norm error as r increases does not hold for individual geometries so no general rule for the size of r can be . It was also determined that the geometries that exist at the extremes of the design space introduce the largest average reduction errors. For all hexapod geometries, a modest reduction was demonstrated enabling the generation of an accurate model under 1000 Hz with a reduced size of $r = 10$ from the original $n = 336$. Above 1000 Hz, the dynamic predictions were shown to be more error prone, but the use of $r = 30$ produces high accuracy models for the full frequency range of interest for the hexapod system. This results in a reduction of the 336 × 336 stiffness and mass matrix to a 30 × 30 state space model capable of capturing all the dominant dynamics. The anisogrid structure demonstrated the ability to generate a highly correlated model with significant reduction compared to the FEM. The 10,272 × 10,272 stiffness and a mass matrix of the anisogrid system were reduced to an accurate 30 × 30 state space model. This represents a significant reduction in the scale of the original model.

This model reduction method has been shown to provide an opportunity to improve on the state of the art reduced models for FEA model reduction problems as well as provide unique opportunities to develop reduced models from test data. The method is computational efficient enabling the calculation of multiple reduces. This enables the identification of the optimally reduced model. Furthermore, it has been shown that this method is simple to use and can provide valuable model reduction capability without the need for a priori accurate model development.

Acknowledgements

The authors would like to acknowledge the support by the Naval Research Laboratory through the Select Graduate Training Program.

References

1. Juang, J.-N. and H. Suzuki, *An eigensystem realization algorithm in frequency domain for modal parameter identification.* Journal of Vibration and Acoustics, 1988. 110(1): p. 24-29.
2. Juang, J.-N., J. Cooper, and J. Wright, *An eigensystem realization algorithm using data correlations (ERA/DC) for modal parameter identification.* Control-Theory and Advanced Technology, 1988. 4(1): p. 5-14.
3. Caicedo, J.M., S.J. Dyke, and E.A. Johnson, *Natural excitation technique and eigensystem realization algorithm for phase I of the IASC-ASCE benchmark problem: Simulated data.* Journal of Engineering Mechanics, 2003.
4. Rebolho, D.C., E.M. Belo, and F.D. Marques, *Aeroelastic parameter identification in wind tunnel testing via the extended eigensystem realization algorithm.* Journal of Vibration and Control, 2014. 20(11): p. 1607-1621.
5. Antoulas, A.C., *Approximation of large-scale dynamical systems*. Vol. 6. 2005: Siam.
6. Guyan, R.J., *Reduction of stiffness and mass matrices.* AIAA journal, 1965. 3(2): p. 380-380.
7. O'Callahan, J., P. Avitabile, and R. Riemer. *System equivalent reduction expansion process (SEREP)*. in *Proceedings of the 7th international modal analysis conference*. 1989. Union College Schnectady, NY.

8. O'Callahan, J. and P. Li. *SEREP expansion*. in *PROCEEDINGS-SPIE THE INTERNATIONAL SOCIETY FOR OPTICAL ENGINEERING*. 1996. SPIE INTERNATIONAL SOCIETY FOR OPTICAL.
9. Koutsovasilis, P. and M. Beitelschmidt, *Comparison of model reduction techniques for large mechanical systems.* Multibody System Dynamics, 2008. 20(2): p. 111-128.
10. Bampton, M.C. and J. CRAIG, Roy R, *Coupling of substructures for dynamic analyses.* AIAA Journal, 1968. 6(7): p. 1313-1319.
11. Ionita, A.C. and A.C. Antoulas, *Data-driven parametrized model reduction in the Loewner framework.* SIAM Journal on Scientific Computing, 2014. 36(3): p. A984-A1007.
12. Zhu, Y., A. Corigliano, and H.D. Espinosa, *A thermal actuator for nanoscale in situ microscopy testing: design and characterization.* Journal of Micromechanics and Microengineering, 2006. 16(2): p. 242.
13. Bühler, J., et al., *Thermally actuated CMOS micromirrors.* Sensors and Actuators A: Physical, 1995. 47(1): p. 572-575.
14. Schweizer, S., et al., *Thermally actuated optical microscanner with large angle and low consumption.* Sensors and Actuators A: Physical, 1999. 76(1): p. 470-477.
15. Schmid, P., F. Hernandez-Guillen, and E. Kohn, *Diamond switch using new thermal actuation principle.* Diamond and related materials, 2003. 12(3): p. 418-421.
16. Singh, J., et al., *3D free space thermally actuated micromirror device.* Sensors and Actuators A: Physical, 2005. 123: p. 468-475.
17. Rahafrooz, A., et al. *Thermal actuation, a suitable mechanism for high frequency electromechanical resonators*. in *Micro Electro Mechanical Systems (MEMS), 2010 IEEE 23rd International Conference on*. 2010. IEEE.
18. Toropova, M.M., *THERMAL ACTUATION THROUGH BIMATERIAL LATTICES*, in *SMASIS*. 2015.
19. Stewart, D., *A platform with six degrees of freedom.* Proceedings of the institution of mechanical engineers, 1965. 180(1): p. 371-386.
20. Taherifar, A., et al., *Kinematic Optimization of Stewart Platform for Simulators Using Genetic Algorithm.* 2013.
21. Paraschiv, I.C., M. Zapciu, and C. Dogariu. *Behaviour Analysis of Hexapod Structure for Integrated Design*. in *Applied Mechanics and Materials*. 2014. Trans Tech Publ.
22. Shi, H., H.-J. Su, and N. Dagalakis, *A stiffness model for control and analysis of a MEMS hexapod nanopositioner.* Mechanism and Machine Theory, 2014. 80: p. 246-264.
23. Shi, H. and H.-J. Su. *Workspace of a flexure hexapod nanopositioner*. in *ASME 2012 International Design Engineering Technical Conferences and Computers and Information in Engineering Conference*. 2012. American Society of Mechanical Engineers.
24. Zierer, J.J., et al. *The development of high-precision hexapod actuators for the Hobby-Eberly Telescope Wide Field Upgrade*. in *SPIE Astronomical Telescopes+ Instrumentation*. 2010. International Society for Optics and Photonics.
25. Wedeking, G.A., J.J. Zierer, and J.R. Jackson. *Kinematic optimization of upgrade to the Hobby-Eberly Telescope through novel use of commercially available three-dimensional CAD package*. in *SPIE Astronomical Telescopes+ Instrumentation*. 2010. International Society for Optics and Photonics.
26. Zierer, J.J., et al. *Design, testing, and installation of a high-precision hexapod for the Hobby-Eberly Telescope dark energy experiment (HETDEX)*. in *SPIE Astronomical Telescopes+ Instrumentation*. 2012. International Society for Optics and Photonics.
27. Totaro, G., *Local buckling modelling of isogrid and anisogrid lattice cylindrical shells with triangular cells.* Composite structures, 2012. 94(2): p. 446-452.
28. Totaro, G. and F. De Nicola, *Recent advance on design and manufacturing of composite anisogrid structures for space launchers.* Acta Astronautica, 2012. 81(2): p. 570-577.
29. Sorrentino, L., et al., *Design and Manufacturing of an Isogrid Structure in Composite Material: Numerical and Experimental Results.* Composite Structures, 2016.
30. Zhang, Y., et al., *Deformation and failure mechanisms of lattice cylindrical shells under axial loading.* International Journal of Mechanical Sciences, 2009. 51(3): p. 213-221.
31. Vasiliev, V. and A. Razin, *Anisogrid composite lattice structures for spacecraft and aircraft applications.* Composite Structures, 2006. 76(1): p. 182-189.
32. Morozov, E., A. Lopatin, and V. Nesterov, *Finite-element modelling and buckling analysis of anisogrid composite lattice cylindrical shells.* Composite Structures, 2011. 93(2): p. 308-323.
33. Vasiliev, V.V., V.A. Barynin, and A.F. Razin, *Anisogrid composite lattice structures–development and aerospace applications.* Composite structures, 2012. 94(3): p. 1117-1127.

34. Vasiliev, V., V. Barynin, and A. Rasin, *Anisogrid lattice structures–survey of development and application.* Composite structures, 2001. 54(2): p. 361-370.
35. Antoulas, A. and B. Anderson, *On the scalar rational interpolation problem.* IMA Journal of Mathematical Control and Information, 1986. 3(2-3): p. 61-88.
36. Ionita, A. and A. Antoulas, *Data-driven parametrized model reduction in the Loewner framework.* SIAM Journal on Scientific Computing, 2014. 36(3): p. A984-A1007.
37. Lefteriu, S. and A.C. Antoulas, *A new approach to modeling multiport systems from frequency-domain data.* Computer-Aided Design of Integrated Circuits and Systems, IEEE Transactions on, 2010. 29(1): p. 14-27.
38. Mayo, A. and A. Antoulas, *A framework for the solution of the generalized realization problem.* Linear algebra and its applications, 2007. 425(2): p. 634-662.
39. Beattie, C.A., Z. Drmač, and S. Gugercin, *Quadrature-based IRKA for optimal H 2 model reduction.* IFAC-PapersOnLine, 2015. 48(1): p. 5-6.
40. Antoulas, A.C., D.C. Sorensen, and S. Gugercin, *A survey of model reduction methods for large-scale systems.* Contemporary mathematics, 2001. 280: p. 193-220.

Improved Model Correlation through Optimal Parameter Ranking using Model Reduction Algorithms: Augmenting Engineering Judgment

Austin A. Phoenix
United States Naval Research Lab, Naval Center for Space Technology

Dustin Bales, Rodrigo Sarlo, Pablo A. Tarazaga
Virginia Tech, Vibrations, Adaptive Structures, and Testing Lab
310 Goodwin Hall, Blacksburg, VA, 24060

Abstract: As the complexity and scales of dynamic models increase, novel and efficient model correlation methodologies are vital to develop accurate models. Classically, to correlate a Finite Element Model (FEM) to a dynamic test, an experienced engineer chooses a small subset of input parameters that are surmised to be crucial, sensitive and/or possibly erroneous. The operator will then use engineering judgment, or a model updating technique to update the parameters until the error between the FEM and the test article is reduced to within a set bound. In order to reduce the intricacy and difficulty of model correlation, a model reduction methodology is proposed to evaluate parameter sensitivity but also the parameter sequence of importance. Thus, in this work the following methods are applied to such a methodology to study this selection process: the Discrete Empirical Interpolation Method (DEIM), Q-DEIM, Projection Coefficient and Weighted Projection Coefficient. This reduced and prioritized scale is achieved by decreasing the number of FEM input parameters used for the subsequent correlation. These model reduction methods identify and rank critical parameters, which results in reduced computational resources and engineering effort required to generate a correlated model. The insight gained using these methods is essential in developing an optimal, reduced parameter set that provides high correlation capability with minimal iterative costs. A representative set of academic and industry experts provided their engineering judgment for comparison with the methodology presented. A comprehensive investigation of the robustness of this methodology is performed on a simple system for demonstration. The scale of the model has expressly been chosen to allow for all potential ranking variations to be evaluated so that these ranking methods can be understood relative to the true optimal ranking. The ranking robustness to incorrect engineering judgment, resulting in uncertainty in the assumed size of the design space and, therefore, the error bounds, is investigated. The methodology presented identifies the most useful parameters for correlation, enabling a straightforward and computationally efficient model correlation approach as compared to other methods presented. To quantify the ranking quality, a metric, the Correlation Norm error, is developed. For the problem discussed, blind random assessments result in a Correlation Norm Error of 413.3. Engineering judgment has been shown to improve upon blind random assessments, reducing the Correlation Norm Error to 334.3. The best performing model reduction method, Q-DEIM using 10 FEM runs as the input, was able to identify the optimal ranking correctly, reducing the Correlation Norm Error to zero.

Keywords: Model Reduction, Model Correlation, Discrete Empirical Interpolation Method (DEIM), Q-DEIM, Finite Element Model (FEM)

1. Introduction

In an attempt to provide highly precise and representative FEMs, a methodology to reduce correlation efforts using model reduction techniques and an iterative FEM is discussed and evaluated. Classically, correlation is achieved by an experienced engineer using judgment to identify parameters of interest and iteratively modifying those parameters in order of perceived importance. Parameters are then changed until the error between the FEM and the test article is reduced to some acceptable threshold and correlation is achieved. In this work, model reduction methods are used to identify the parameters required, i.e., the dimensions of the problem, that are required to best match the dynamics of the system. In this case, the proposed methodology attempts to use reduction methods to determine the parameters that are most mathematically independent, so that redundant, or low impact parameters, are not required for correlation and can thus be truncated. These techniques, when used in conjunction with classic or state of the art correlation methods, provide the minimum number of parameters required to achieve correlation, resulting in a faster, more efficient model correlation effort.

In the past few decades, many improvements have been made in model updating [1-8] to automate the correlation process, enabling accurate models that were previously nearly impossible to achieve. In addition, recent structural health monitoring [9-11] and surrogate system design [12] techniques have employed machine learning to learn relationships between FE model responses and the modeling parameters. The method herein can be leveraged to improve the efficiency of these updating methods by optimally reducing the size of the problem and providing insight into the most relevant parameters for correlation. This is particularly important for scaling these methods to larger and more complex structures. Parameter identification using sensitivity analysis [6-8, 13-15] has been robustly demonstrated to aid in this process of parameter selection. In recent years, a clear division between two methods of sensitivity analysis, the local and global methods, have been developed in [15]. The key difference between the two is succinctly described as follows: local sensitivity analysis techniques examine the local response of the output by varying a single parameter and keeping all other parameters at their nominal value; global sensitivity techniques examine the global response averaged over variations due to all parameters by exploring a finite region of the defined design space. This study focuses on local sensitivity analysis while implementing some aspects of a global sensitivity evaluation.

Once the method to vary the input parameter set is defined, multiple methods can be used for evaluating and quantifying the variations in the output due to the input uncertainties. The reduction, or truncation, of the degrees of freedom using SVD methods and Principle Component Analysis (PCA) has been documented in [16-18]. Identification of the parameters of specific geometric importance relative to test hardware using statistical methods has also been employed in [5]. Methods have also been implemented using projection coefficient [7, 19] to provide a ranking of parameter importance. These methods provide insight into the parameters of importance. Work by the authors [20] has provided some basic understating on the possible use of newly developed reduction methods, such as DEIM and Q-DEIM, for parametric sensitivity analysis. These methods have shown significant promise for the identification of optimal input sets for other applications such as optimal sensor placement [21]. In addition, this paper also introduces a modification of the Projection Coefficient for a simple five parameter system, the Weighted Projection Coefficient, and examines the resulting quality of the parameter ranking as compared to engineering judgment. The Correlation Norm Error, discussed herein, is development and used to provide a metric by which to compare relative rankings. To expand on previous work, and improve the model reduction algorithm implementation, a study is performed on the impact of an increased scale Sensitivity Matrix. This study is performed by capturing higher order parameter coupling. This is used to identify the optimal input set size to be used in conjunction with the model reduction methods. Additionally, a comparison is made between the quality of the rankings and the required computational cost. As there are initial error bound assumptions specified for use in this methodology, the effects of uncertainty in those initial error bound assumptions is investigated in order to understand the robustness of the methodology. It is not the intent of this paper to provide a model correlation methodology, but instead, to provide a method for improving the implementation of the correlation method of choice by providing an optimally reduced parameter set.

A methodology explanation is presented in Section 3 along with the process of developing the appropriate input matrix and the use of the model reduction algorithms. An overview of the modelling reduction Projection Coefficient, Weighted Projection Coefficient, SVD-DEIM, and Q-DEIM is briefly provided in Section 4. A case study is performed using a ‘simple’ five-parameter model to demonstrate the process and discuss the outcomes of this methodology in Section 6. To examine the quality of the dynamic correlation metric used, an investigation into the H_2 norm correlation, as compared to first and second mode frequency, and an amplitude error is performed in Section 7. Additionally, the engineering judgment ranking, set development, and quality are discussed. The resulting quality of the methodology is presented for all of the proposed ranking methods in Section 7. To ensure that the methodology is valid for larger systems, an investigation into the computational cost of the resulting methods as a function of the resulting correlation quality was completed. Finally, an investigation is performed into the ranking variability when given uncertain error bounds to ensure system robustness in Section 8.

2. Established Parameter Identification Methods

To provide a comparison for this methodology, established parameter identification methods and tools are discussed. The examined methods are: engineering judgment, sensitivity analysis and SVD analysis. Engineering judgment and sensitivity analysis are established parameter ranking methods, where SVD is used as an indicator of the ability to truncate the problem to remove unnecessary parameters.

2.1 Engineering Judgment

Engineering judgment is critical for any model correlation effort. For this method, engineering judgment is required to identify the initial parameter set under investigation and identify the error bounds, or design space, of the system. Through previous work by the authors, it has been shown that engineering judgment is not always a reliable method to identify the critical parameters of complex models. In this case, the simple five parameter system provides an opportunity to study engineering judgment responses for a dynamically simple case. The engineering judgment evaluation is done to offer a baseline for comparison to better understand the reduction of correlation effort through the use of the proposed ranking methodology. To develop a robust engineering judgment data set, 16 experienced engineers in industry and academia were asked to examine the case study in Section 6 and rank the parameters by their perceived importance in correlation.

2.2 Sensitivity Analysis

Sensitivity analysis is the study of how the uncertainty in the output of a model can be allocated to different sources of uncertainty in the model inputs. In the case of model correlation and parameter ranking, sensitivity analysis is used to identify the input parameters that exhibit the largest model sensitivity to input changes relative to the given error bounds. In sensitivity analysis methods the first step is to decide to vary either a single parameter, multiple parameters, or randomly varying multiple input parameters as well as the scale of those variations. The second step is to identify the method of ranking quantitatively parameter importance from the output. Over the years, there have been many attempts to define the optimal method to quantify parameter importance. A detailed example can be found in [8]; here, the first twelve eigenvalues are evaluated against 149 stiffness input parameters that were assessed at the maximum error bound value. The top ten parameters are defined by the sum of the variations over all of the evaluated modes. Another key advance in this paper was the ‘condensing’ of multiple parameters that demonstrated the same normalized sensitivity into a single stiffness parameter. This reduced the overall complexity of the correlation effort; however, this required the condensed parameters to be the same input parameter type. Methods have also been implemented where each input is quantified simply by the output responses maximum deviation percent [19, 22] or the dimensionless gradient [23]. More specific to the dynamic excitation frequency domain, eigenvalues are used as a robust comparison [24]. In cases where the amplitude is critical, frequency and amplitude correlation functions [25] have been implemented. The first order reliability methods (FORM) has been defined in [26] and used in [27] where a given performance function is defined to quantify the importance of a parameters effect on the system. New methods, such as the use of orthogonalization and Mean-Squared Error methods, as a parameter ranking method, in conjunction with sensitivity analysis, can be seen in [28, 29]. Further investigation into the use of perturbation analysis to estimate the sensitivity-related importance measures of the parameters has also been attempted in [30].

While sensitivity analysis is a prolific field, little consensus exists among experts on the single best methodology to use. This paper introduces a new cost function and a new step in the classic sensitivity analysis process. The cost function used to compare the output responses, is an evenly weighted difference calculation that uses the Frequency Response Function (FRF) and the nominal FRF response, which is evaluated at all frequencies. This generates a cost function of length associated with the evaluation of the FRF. In the approach presented here this is a $\mathbb{R}^{1\times1458}$ vector for each FEM evaluation. Thus, by analyzing the effect of different parameters, these vectors can then be concatenated into a matrix which will be referred to as the Sensitivity matrix. In order to fully study the methodology only five parameters have been chosen as possible modeling error locations or uncertainties; two thickness, two lumped masses and damping (fully described in Table 2 and Fig 8). The choice of only five parameters enabled the full design space to be evaluated using a brute force approach in order to benchmark the proposed methodology described herein. The use of five parameters balances the computational cost with ensuring the methodology is evaluated on a reasonable scaled problem. The next step in the development of the ranking is the application of model reduction techniques to condense the $\mathbb{R}^{5\times1458}$ Sensitivity matrix into a five parameter ranking. Overall, the efforts discussed in this paper are focused on providing low computational cost, enabling the removal of redundant design space parameters, providing a single metric to evaluate all parameters, and ensuring that negative and positive uncertainties are captured. This paper expands on sensitivity analysis, with a particular focus on the novel use of model reduction algorithms to quantify the importance of individual parameter responses measured in the Sensitivity matrix.

2.2.1 Sensitivity Analysis Investigation

To evaluate the sensitivity analysis method, eleven FRF responses are generated for comparison, one for the nominal case, five for each parameter at the maximum of the error bound, and five for each parameter at the minimum of the error bound. The data provides valuable insight into the qualitative importance of each parameter, and is shown in Fig. 14. (Table 2 and Fig 8 will aid in the meaning of the legends of this figure).

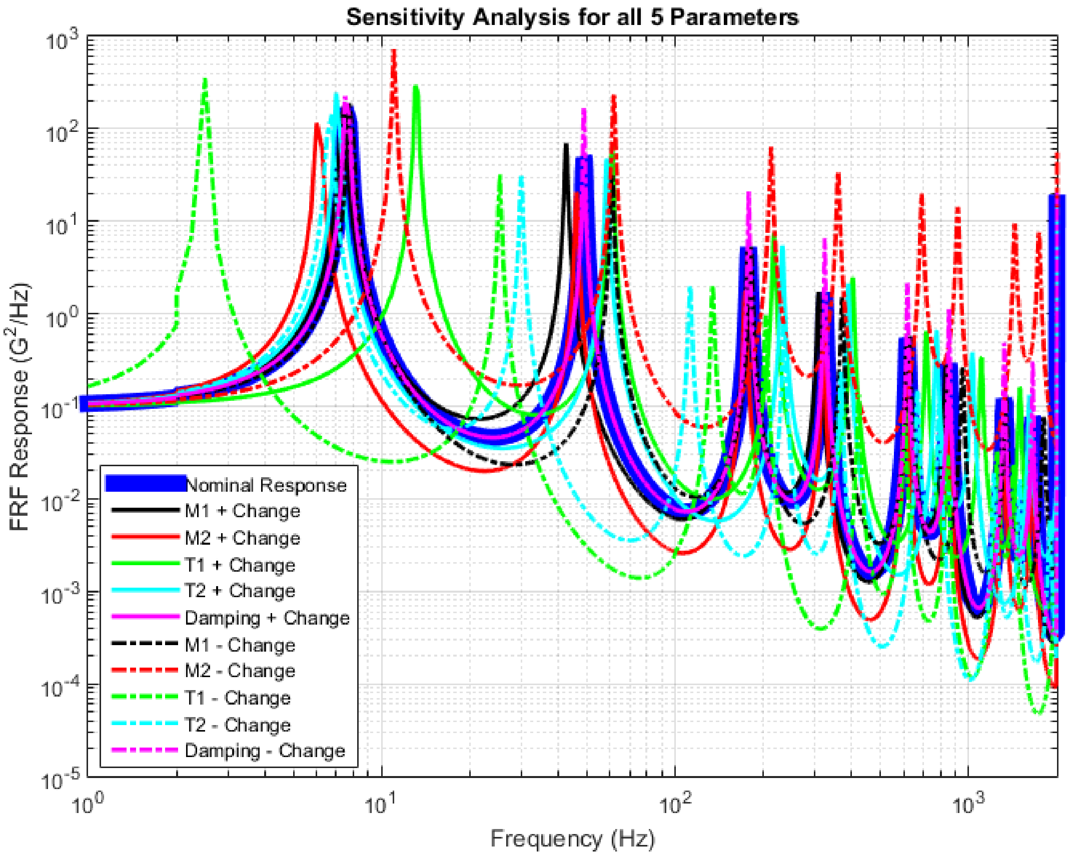

Fig. 14 Frequency Response Function (FRF) for all Parameters at the ends of the error bounds.

As can be seen, there is a broad range of responses based on the various inputs. By investigating Fig. 14, it can be seen that thickness 1 (T1) and mass 1 (M2) have a significant effect on the dynamics, but the generation of a full ranking of parameter importance for this simple system is challenging. A note worth discussing is that the variation in the dynamic behavior associated with parameters is that positive and negative sides of the error bounds is not symmetric and varies significantly. For this reason, it is important to evaluate both extremes of the error bound to understand the parameters' impact on the system dynamics.

2.3 Singular Value Decomposition Analysis

Once the Sensitivity matrix has been calculated, it is used as the input to model reduction methods as well as the input to an SVD pre-analysis. The SVD analysis is critical to identify the decomposition of the system via its singular values that would yield an approximate reduced order of the system while still maintaining the most important information of the matrix. In particular, it is favored to see large drops in the singular values assuring that only a small number of singular values contain most of the valuable information needed, and the rest play a less significant role in the matrix information. This is of major importance as this not only ranks the parameters but informs of their relative importance. This then allows the system to be reduced by truncation. The SVD for the Sensitivity matrix is shown in Fig. 15 for five vectors at the positive error bounds.

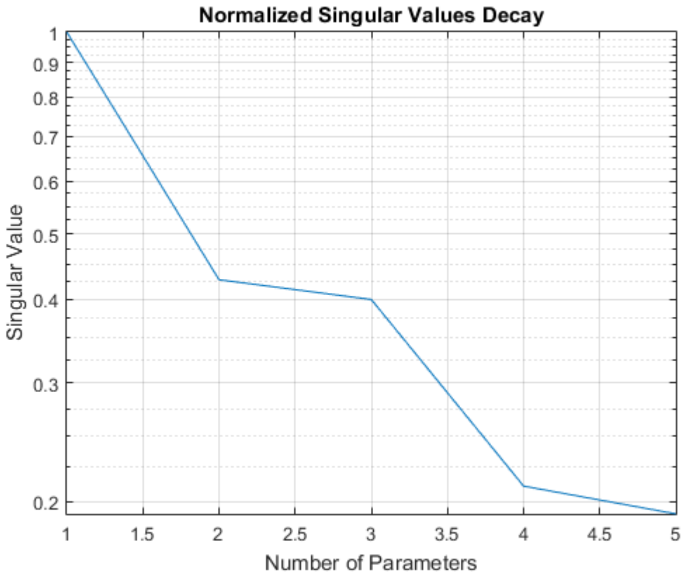

Fig. 15 Normalized SVD for the five parameter system

Normalized singular values that are significantly smaller are indicative of parameters that are less relevant to the dynamics of the system. The SVD identifies the number of independent inputs in the system, which allows the identification of redundant or unnecessary degrees of freedom. The SVD values for this problem are such that no parameters can be ignored or truncated during correlation without reduced correlation capability. While this simple model allows for examination of the proposed methodology, this model does not exemplify the situations where this methodology provides the most impact. The most impact would be seen in cases with larger exponential decay due to unnecessary parameters resulting in clear opportunities for truncation. This would be especially true when less is known about the system so a large number of parameters are included resulting in an obvious truncation point. In the five parameter case under investigation, all five parameters are shown to be relatively significant so no truncation is performed.

3. Parameter Ranking Methodology

The first step in developing a robust parameter ranking is to identify the parameters in the FEM that sufficiently represent all significant system physics. All though all parameters can be chosen, this has historically proven to be computationally prohibitive especially with modern day complex models. Through a verification process [31] there are parameters that can be identified as crucial for an updating analysis. Regardless, this process can always be restarted with new or additional parameters at this stage in the method. The computational cost of ranking a parameter is low compared to the cost of leaving out a critical parameter as correlation would become impossible and further updating would be required. At this stage, the computational cost of including too many parameters is low compared to the cost of leaving out a critical parameter as correlation would become impossible and further updating would be forced on incorrect parameters. For this reason, over parameterization is encouraged, within reason. Once all parameters of interest are identified, a reasonable error bound for each parameter needs to be carefully chosen. The error bound, if chosen well, conservatively defines the appropriate design space that encompasses all potential test geometries. Otherwise, the resulting ranking quality will be reduced as is discussed in section 8.1. The second step is to develop the Sensitivity Input matrix, S_{input}, which is used to evaluate the dynamic impact of a parameter change. The Sensitivity Input matrix enables independent parameter investigation by developing ‘on/off’ FEM input sets, shown in Fig. 16. In the case of the five parameter test model, six FEM inputs provide the minimal size input set. The first input vector of the Sensitivity Input matrix is made up of the five nominal parameter inputs (row 1 in Fig. 16). For each other vector, all parameters are set to its nominal value except for a single parameter that is increased to the maximum value in the error bound as detailed in Equation 1. The parameters $P_1\ through\ P_n$, are changed relative to the nominal parameter input values by the associated parameter error bound $e_1\ through\ e_n$. This method is detailed by

$$S_{input}(1{:}6,:) = [P_1, P_2, \ldots, P_5]\ and\ for\ i = 1{:}5\ S_{input}(i+1, i) = P_i(1+e_i)\ . \qquad [1]$$

The visualization of the resulting difference between the parameter values in the Sensitivity matrix and the nominal parameter values is shown in Fig. 16. The plot displays the parameters’ magnitude, at the maximum value in the error bounds, relative to the nominal normalized parameter value used to develop the Sensitivity Input matrix. The use of a larger order Sensitivity input matrix to improve ranking quality will be discussed further in Section 5.

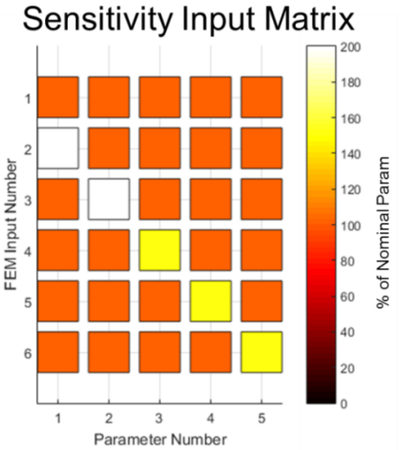

Fig. 16 Sensitivity Input matrix development relative to the nominal parameters.

The flowchart in Fig. 5 summarizes the flow of data from the Sensitivity Input matrix to the correlated model. Each row of the S_{input} matrix is the vector used as the input parameter vector for each of the *n* FEM models where *n* is the number of rows in the S_{input} matrix. The resulting FRF outputs from the FEM model are all normalized by the nominal response resulting in *n*-1 normalized FRFs. These FRFs are combined in a single matrix to generate the Sensitivity matrix, S, as graphically depicted in Fig. 18. The model reduction algorithms use the Sensitivity matrix as an input to generate the parameter ranking. A SVD analysis is then used to determine the number of parameters to be used for an initial correlation attempt. The optimal ranking and minimum number of parameters required are used to help correlate the model efficiently. If model correlation is unachievable to a desired level of accuracy given the parameters used, more parameters can be included or even altered (e.g., drop the parameters corresponding to the lowest singular values and add new parameters). To better explain the method by which these reduction algorithms are used for parameter ranking, the methodology is illustrated in Fig. 17.

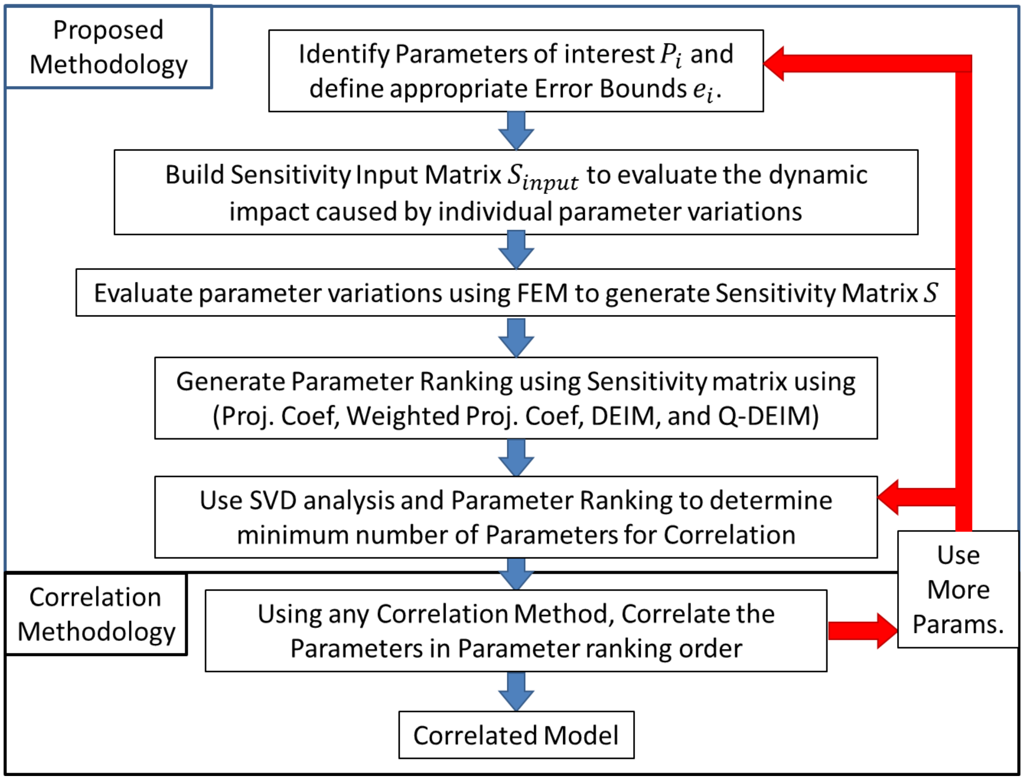

Fig. 17 Methodology for Parameter Ranking Development for Correlation.

Each row of the $\boldsymbol{S_{input}}$ matrix is used to generate a single FEM input set resulting in a single FRF. The resulting *n* FEM's outputs are concatenated into a $\mathbb{R}^{n\times 1458}$ matrix, *S*, where *n* is the number of parameters, and 1458 is the dimension of the FRF. As shown in Fig. 18, the FEA output is subtracted by the nominal input to generate the FRF response difference between the $\mathbb{R}^{n\times 1458}$ FRF response matrix and the nominal input. The resulting matrix is the Sensitivity matrix. This Sensitivity matrix is used with the four proposed model reduction methods to generate four different parameter rankings. Those rankings are then used to inform the order and the number of parameters used for correlation using the engineer's preferred correlation method. The most important parameters decided by the ranking should be the parameters correlated first**.** The true correlated values are known for this methodology demonstration, so once the parameter ranking is identified, correlation is trivial herein and not the focus of the work.

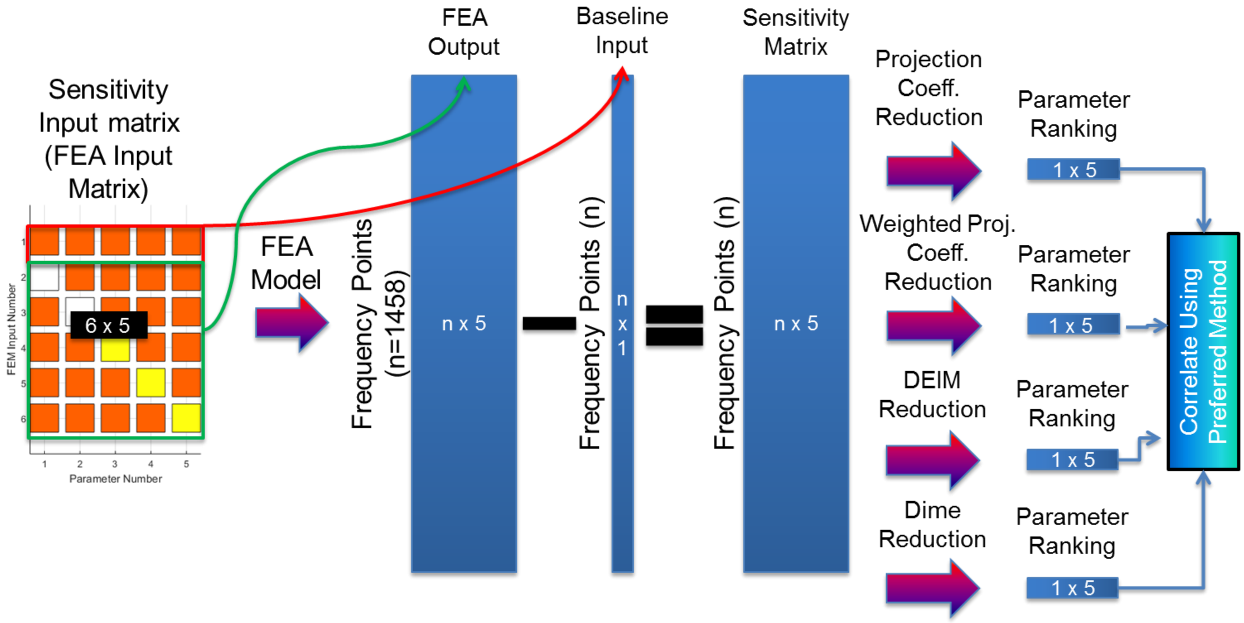

Fig. 18 Data flowchart from Sensitivity Input matrix development to model correlation.

As can be seen, the Sensitivity matrix is an evenly weighted difference calculation using the FRF response and the nominal FRF response evaluated at all frequencies. This results in a Sensitivity matrix of size $\mathbb{R}^{5\times1458}$ for the five input cases. Classical sensitivity methods would use a deviation percent or frequency and amplitude correlation function to calculate the parameter importance. In this case, the use of model reduction methods is implemented to provide a novel look at the ranking and uniqueness of each parameter for correlation. The use of model reduction methods inherently removes redundant, or low impact, parameters from the correlation effort. The various model reduction methods are discussed in Section 4.

4. Model Reduction Methods

To determine the optimal method for ranking the critical parameters, previously used methods, such as a projection coefficient and engineering judgment, are compared to three model reduction methods known as Discrete Empirical Interpolation Method (DEIM), Q-DEIM and Weighted Projection Coefficient. The Sensitivity matrix S is used as the input for the Projection Coefficient, Weighed Projection Coefficient, DEIM and Q-DEIM evaluations. To better understand the differences between these methods, a brief discussion detailing each method is provided.

4.1 SVD DEIM

DEIM was proposed by Chaturantabut and Sorensen in [32] for use in the reduction of dynamic systems. Sorensen and Embree in [33][4] used a database search as an example similar to the proposed use in this work to find representative web pages from two geographic areas. The methodology in this work uses an SVD of the acceleration output of the parameter sweep and then a greedy search algorithm DEIM.

DEIM is an efficient method to project high-dimensional, non-linear functions into a lower dimensional space for the purpose of data reduction [32]. The DEIM algorithm (found in [32]) iteratively minimizes the error of the approximation or projection onto a lower dimensional space via a selected index. The first entry is chosen by determining the index of the largest magnitude of the left eigenvector. Other entries are chosen by selecting the index associated with the largest residual error. The residual is effectively the error between the input basis and its approximation due to interpolating the basis. The SVD-DEIM methodology allows for the determination of the most independent parameters for every trial.

4.2 Q-DEIM

The Q-DEIM method, which is an alternate formulation of the DEIM, was developed using a QR matrix factorization for the purpose of large-scale systems. Previous applications of this methodology are found in [34], where various dynamic systems are reduced as examples for comparison to the DEIM method. The Q-DEIM method offers an improved theoretical bound on the error of the projection on a lower dimensional space compared to DEIM [34].

As stated earlier, the formulation of this method is through the QR factorization of the Sensitivity matrix. The QR transformation, further explained in [35], is the factorization of a matrix, S (in our case), into the form:

$$S = QR \,, \tag{2}$$

where Q is an orthogonal matrix and R is an upper triangular matrix. The algorithm for Q-DEIM can be found in [34].

4.3 Projection Coefficient

The projection coefficient method is often used in the dynamics modeling field to determine the degree to which an experimental and analytical mode shape match. Perinpanayagam, Ewins, and Chen [36, 37] show examples of using such formulation in sub-structural testing. This is proposed in order to determine the most relevant modes to test of the subcomponents toward the importance and relevance of the condition of the assembled structure. The formulation of the projection coefficients requires examining the angle between the original singular vectors (in this case, the acceleration with one parameter set to its maximum error value) and the left eigenvectors produced by the SVD.

The coefficient is calculated as the cosine of the angle between two vectors (in this case, a single left eigenvector and a single vector of the Sensitivity matrix). Seen in the following equation as,

$$Projection\ Coefficient = PC = \cos(\theta) = \frac{a \cdot b}{|a||b|} \,, \tag{3}$$

where θ is the angle between the two vectors, a is the left eigenvector and b is the original data vector. The coefficient varies between 1 and 0, where 1 represents a high degree of alignment of the two vectors and 0 represents orthogonality between them.

Understanding how the first left eigenvector relates to the original data, allows for an investigation of which parameters are most independent. A seemingly arbitrary selection of the first eigenvector is justified by the previously mentioned singular value decay. For this inquiry, the first singular value accounts for an average of 63 % of the sum of all singular values. The first eigenvector is chosen as it represents the largest amount of the original data set while enabling the data to be reduced to a single vector (for the angle of alignment comparison).

4.4 Weighted Projection Coefficient

The insight for the Weighted Projection Coefficient method comes from the fact that, in using only the first eigenvector in developing the Projection Coefficient, there is an undervaluing of other certain parameters. If the second eigenvector were used in the formulation of the Projection Coefficient, then a completely different ranking would result. Weighted Projection Coefficients are proposed to account for the value of each parameter as determined by the similarity measure from all but the first eigenvector. The first eigenvector is very representative of the data, which is apparent by the largest associated singular value. Therefore, the choice was made to weigh each of the similarities between respective eigenvectors and the original vectors by the associated singular value. These weighted similarity coefficients are then summed over the respective parameter to provide a ranking that accounts for the importance of a parameter as seen by the remaining eigenvectors. To our knowledge, this proposed extension of the Projection Coefficient is not present in the literature.

The output of these methods, the Weighted Projection Coefficient, Projection Coefficients, DEIM, and Q-DEIM, is a ranking of the parameters from most independent to most redundant. The ordering of the parameters were tested against the engineering judgment ranking to show the variations between each ranking process as well as against all possible correlation orders.

5. Expansion of Proposed Ranking Methodology

Many sensitivity methods make the assumption that the single positive parameters, used to generate the Sensitivity Input matrix (shown in Fig. 16), is sufficient to produce an acceptable ranking via the methods previously discussed. To expand on this work, an examination of that assumption is performed by providing various Sensitivity Input matrices that include increasing amounts of coupling between parameters. In the originally discussed Sensitivity Input matrix, no parameter coupling is captured as only one parameter at a time is set to a non-nominal value. The increase in complexity is evaluated to improve the quality model reduction ranking by providing more coupled system dynamics. To develop a Sensitivity Input matrix that can evaluate both the positive and negative parameter changes, the positive change Sensitivity Input matrix was appended with the negative changes, as can be seen in Fig. 19 (B). Using the previous methodology, the ranking algorithms would output a ten-parameter ranking. Three weighing methods are employed to condense the ten-parameter ranking back into a five-parameter ranking.

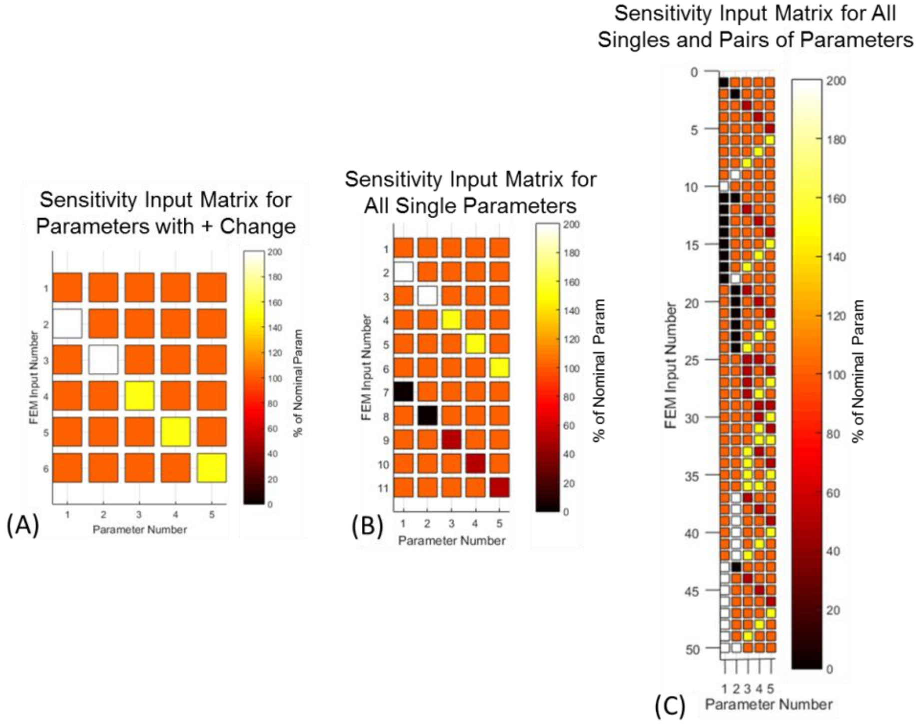

Fig. 19 Sensitivity input matrix. (A) Five parameters with all parameters at their max error bound. (B) Ten parameters with all parameters at max and min of their error bound. (C) Fifty parameters with all possible combinations of two parameters.

The critical physics that is not included in the five parameter input data set that is provided for the model reduction methods, is the subsequent coupling that exists between multiple parameters. For the five parameter system, it is possible to evaluate all potential coupling combinations associated with each parameter at three values: its maximum error bound, the nominal value, and the minimum error bound. This evaluation results in 3^5 or, alternatively, 243 potential combinations of parameter inputs. To investigate the quality of the resulting ranking as a function of the computational cost, reduced sets are also studied. Sets combining one parameter, two parameters (seen in Fig. 19), three parameter and four parameters simultanoeusly were chosen as the coupling subdivision cases for evaluation. For this assessment, all higher order coupling cases include all previous cases, as seen in Table 4. This analysis allows for a better understanding of the relationship between the input data size and the resulting ranking quality. Balance must be made as enough input data must be generated to have a meaningful ranking; but the more input data generated, the larger the computational cost associated with this methodology.

Table 4 Representative Breakdown of all 17 Weighting and Ranking Methods for Each Model Reduction Method.

Ranking Evaluations Applied to Each Model Reduction Method			
# of Params	Sensitivity Matrix Input Description	Weighting Method	Rank #
5	Positive	-	1
5	Negative	-	2
10	Pos+Neg (All Singles)	Linear	3
50	Singles+Pairs	Linear	4
130	Singles+Pairs+Trips	Linear	5
210	Singles+Pairs+Trips+Quads	Linear	6
243	All	Linear	7
10	Pos+Neg (All Singles)	Log	8
50	Singles+Pairs	Log	9
130	Singles+Pairs+Trips	Log	10
210	Singles+Pairs+Trips+Quads	Log	11
243	All	Log	12
10	Pos+Neg (All Singles)	SVD	13
50	Singles+Pairs	SVD	14
130	Singles+Pairs+Trips	SVD	15
210	Singles+Pairs+Trips+Quads	SVD	16
243	All	SVD	17

5.1 Weighted Ranking of Model Reduction Methods

A study is performed into the expansion of the input data used in the development of the original Sensitivity Input matrix. The multiple rankings that result from each of the methods must be combined to succinctly still target only the five parameters used. Rank aggregation is the field of study associated with combining multiple rankings and there has been significant study in this field with several methods to be employed; further reading on the subject is available in [38]. While further examination of the rank aggregation method can be completed, this work studies modified Borda methods that produce a ranking based on a scaling that rewards a high ranking and punishes a lower ranking [39]. The weighting methods chosen are linear, log and the singular values output from the previously mentioned SVD analysis, shown in Fig. 15. The quality of these resulting methods is studied further in this work.

In total, this work examines four model reduction methods as applied to seven Sensitivity Input matrix formulations. For five of the seven Sensitivity Input matrices, three weighting scales are implemented, resulting in 68 unique rankings combinations. This paper details the effort to identify the optimal size of the Sensitivity input matrix, the optimal weighting method, and the optimal model reduction method under a variety of conditions.

5.2 All Possible Ranks Evaluation

To develop a baseline understanding so that all ranking methods such as engineering judgment, DEIM, Q-DEIM, Projection, and Weighted Projection can be compared, 120 possible parameter rankings are computed. By evaluating all possible rankings, the true optimal ranking, the blind random ranking and the mean engineering judgment ranking can be calculated. Knowledge of all possible rankings allows for an examination of the overall effectiveness of a given method.

6. Case Study: Five Parameter Cantilever Beam

The test geometry for this study is comprised of a fixed base cantilever beam made out of AL 6061, $18\frac{1}{16}$ inches long with a cross section of $\frac{1}{8}$ inches by 1 inch. Five parameters are evaluated for this system. Two unknown point masses are located at the center point ($x = ½\, L$) and the tip ($x = L$) and, two unknown beam thicknesses are applied at ($x = 0\ through\ ½\, L$), and ($x = ½\, L\ through\ L$). The final parameter of interest is the global damping value. These five parameters directly affect the mass, stiffness, and damping matrix of this system while providing a straightforward correlation problem.

In the development of any model, there are both a standard deviation and an uncertainty in the input parameter values obtained from the manufacturer (i.e., Young's Modulus) or introduced through variations in assembly (i.e., damping). Thus, these parameters have a set uncertainty associated with the 'real-world' system that needs to be updated to be able to correlate the FEM results. The inputs that are required from the user are the FEM input parameters of interest and the reasonable error bounds (seen in Table 5) for those parameters. The error bound, if chosen well, conservatively defines the appropriate design space that encompasses all potential test geometries. Five parameters are used to define the system, as shown in Fig. 20.

Table 5 The parameter list with applied error bounds.

Parameter Description	ID #	Nominal Value	Units	Error Bound
Mass 1	1	0.0625	lb	100%
Mass 2	2	0.0625	lb	100%
Thickness 1	3	0.125	in	50%
Thickness 2	4	0.125	in	50%
Damping	5	0.01	in/in	50%

This beam is modeled using a FEM, and large error bounds have been assumed to provide an interesting, albeit large, design space so that the proposed methodology can be investigated. This work compares FEM simulation results to FEM simulation. The nominal, or baseline, input values for the FEM can be seen in Table 5. The FEM used to evaluate the system, shown in Fig. 20, is developed in MSC Nastran using SOL 111 for random vibration excitation, from 1 to 2000Hz in the Y-axis with an amplitude of $1.25\text{x}10^{-4} g^2/Hz$. The model uses 100 linear beam elements. Two mass elements are used to represent the variable mass parameters 1 and 2, resulting in an FEM consisting of 101 nodes and 606 Degrees of Freedom (DOF). The frequency response function is recovered for the base input excitation and tip response for all six DOF. The Y axis response of interest is the beam tip response located at $x = L$. These five parameters do not encompass all potential FEM input parameters, but do provide a reasonable parameter set for initial investigation. This system provides a good basis for methodology verification due to its simplicity, in terms of the number of parameters, enabling for the calculation of the "true" optimal parameter set. The relative simplicity also allows a reasonable basis for comparison to engineering judgment.

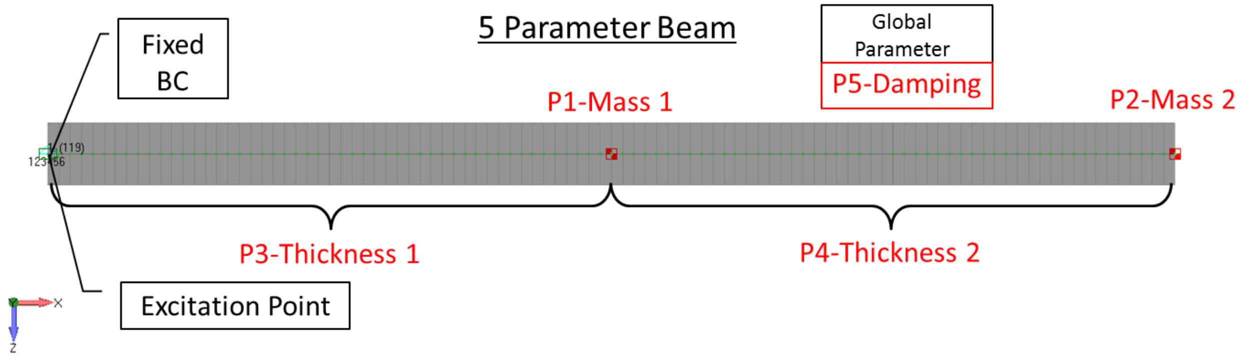

Fig. 20 FEM with Parameters and Points of Interest Highlighted.

While the error bounds used in this problem are for demonstration purposes, the specific error bound choice has a significant effect on the resulting parameter ranking. When calculating the parameter importance, the algorithm evaluates variations in the response FRF due to parameters set to the maximum and minimum values allowed by the prescribed error bound. The use of parameter specific error bounds rather than global error bounds provides the opportunity to define a more representative design space for the particular test hardware. In this case, an FEM to FEM comparison is used, so the hardware design space is precisely specified by the applied error. To ensure the system is robust to errors between the error bound and the actual hardware design space, an investigation is done into the impact of uncertainties in the assigned error bound, discussed in Section 8. A discussion of the parameter ranking methodology follows.

7. Ranking Methodology Verification through Correlation

A baseline is required to compare the quality of the correlation produced through the use of these ranking algorithms so that the quality of the methodology can be verified. To evaluate the rankings, all potential rankings need to be developed and correlated. The output ranking provided by the various model reduction algorithms are then compared on 90 test geometries that represent 'real' geometries requiring correlated FEMs. Ninety representative test cases were correlated on each ranking independently. These 'real' geometries are developed using parameters that are randomly distributed within the given error bounds. For example, the thickness of the first test geometry is,

$$T_1 = T_n(1 + \alpha e_T) \qquad [4]$$

where T_n is the nominal thickness, α is the randomized scale factor, e_T is the error bound for the thickness, and T_1 is the new randomized thickness for the 1st geometry. The resulting five parameters, randomized within the error bounds, are then used to produce FRFs using an iterative FEM code developed for this investigation. As can be seen in Fig. 21, the frequency and dynamic responses for each of these test geometries vary greatly, representing a large design space. To ensure that the full design space of the five parameter model is well represented, an arbitrary but statistically significant number of test geometries is used.

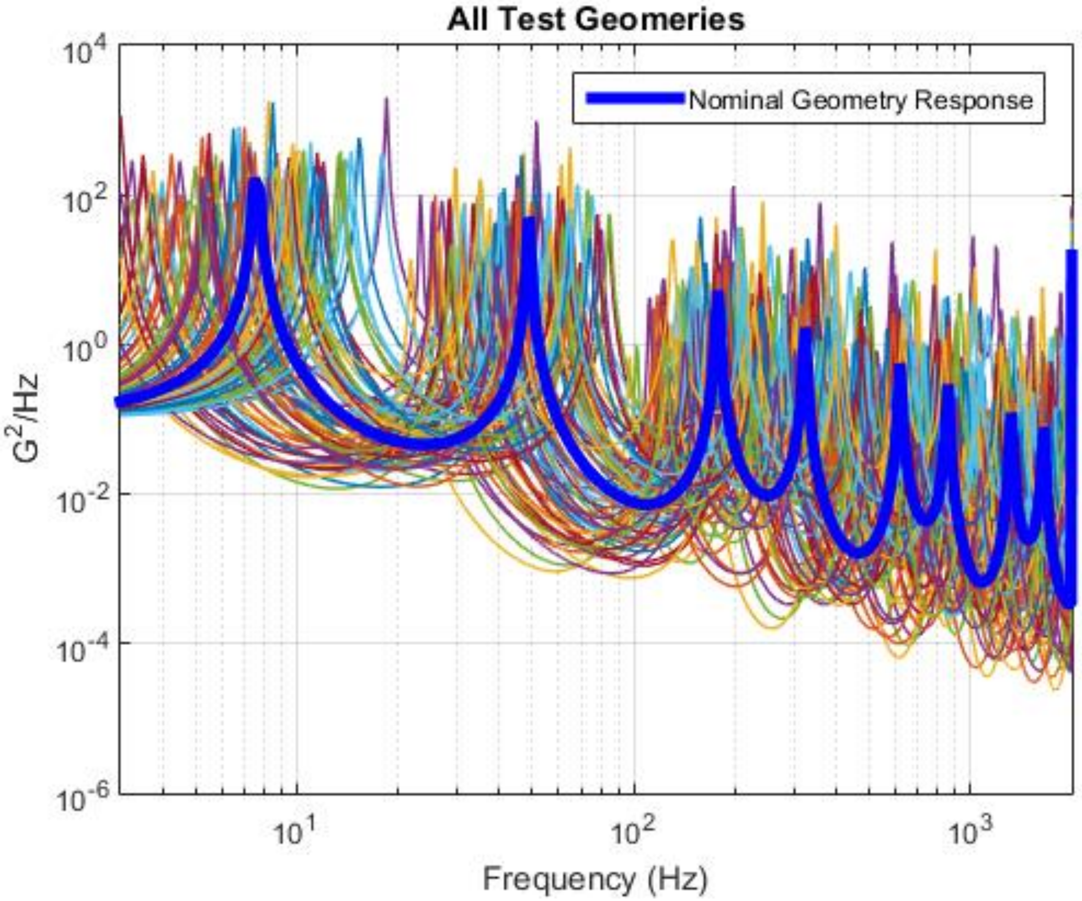

Fig. 21 All 90 geometries frequency responses used to validate the methodology.

The use of this methodology enables the simulation of a high number of test results and provides a sufficient statistical basis to validate the parameter ranking methodology, without carrying out a similar number of hardware tests. To evaluate one ranking on a given geometry, five FEM runs are created. For the five FEM runs labeled $n = 1{:}5$, the top n ranked parameters for a given ranking are set to the exact parameter value of the test geometry. This is repeated for all 90 geometries and all 120 possible rankings resulting in 54000 runs. The methodology to generate the input parameters for the FEM correlation runs for a single geometry (geometry 49) and one ranking case (the optimal ranking) is shown in Table 6. The starting point for this ranking evaluation is at the nominal geometry where all five parameter values are set to the nominal parameter value. To evaluate the i^{th} parameter correlation case, the $1\ through\ the\ i^{th}$ most important parameters are perfect correlated by being set to the intended geometries parameter value. Once all five parameters are correlated, the correlated geometry exactly matches the inputs for geometry 49.

Table 6 Correlation inputs for FEM runs for the optimal rank order (P3, P2, P4, P1, P5) with correlated values shown in black.

Correlation Run Inputs for Optimal Rank Order on Geometry 49					
Description	Mass 1 (P1)	Mass 2 (P2)	Thickness 1 (P3)	Thickness 2 (P4)	Damping (P5)
Nominal	0.0625	0.0625	0.125	0.125	0.01
1 Param Correlated	0.0625	0.0625	1.33E-01	0.125	0.01
2 Param Correlated	0.0625	5.82E-02	1.33E-01	0.125	0.01
3 Param Correlated	0.0625	5.82E-02	1.33E-01	1.24E-01	0.01
4 Param Correlated	1.12E-01	5.82E-02	1.33E-01	1.24E-01	0.01
5 Param Correlated	1.12E-01	5.82E-02	1.33E-01	1.24E-01	5.68E-03
Geom 49 Params.	1.12E-01	5.82E-02	1.33E-01	1.24E-01	5.68E-03

As can be seen with the optimal ranking in Fig. 22 (A), each parameter correlated shifts the FRF from the nominal geometry toward the response of the test geometry. At five parameters correlated, the correlated FEM exactly matches the test response. To simplify the plot the five parameters correlated model is not plotted. At two correlated parameters in Fig. 22 (A), the first mode is well matched, but the second mode is uncorrelated; however, as each subsequent parameter is correlated, the frequency response behaves more closely to that of the test geometry. Fig. 22 (B) shows the worst ranking order possible. It can be seen that the ranking order of parameters introduces significant differences in correlation quality when compared to the best ranking order. This example demonstrates the benefits associated with identifying and using the optimal correlation order.

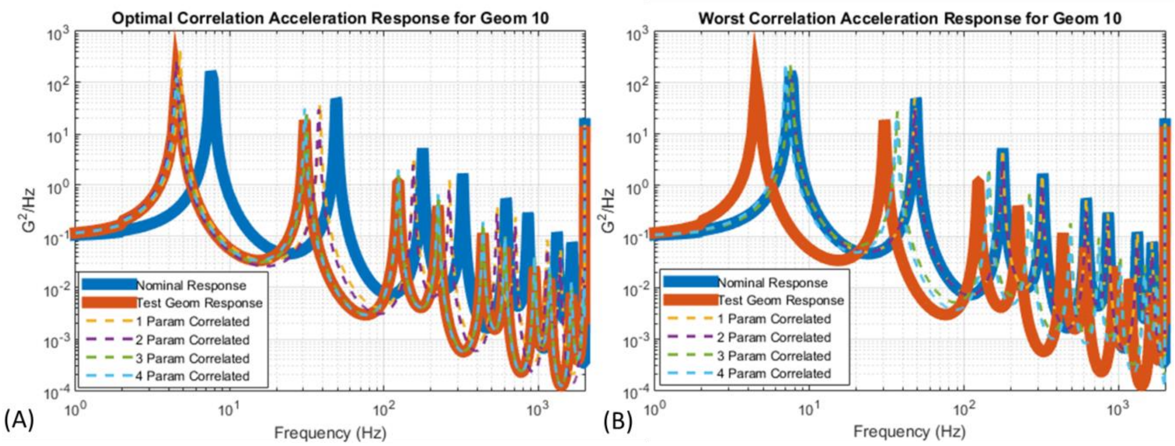

Fig. 22 (A) Correlation using the best ranking. (B) Correlation using worst Ranking.

.

7.1 Correlation Metric Comparison Between H2 norm and Peak Modal Response

The chosen correlation metric used to compare the test geometry and the correlated geometry FRFs is the H_2 norm. The H_2 norm provides a method to determine the total error between the two frequency response functions so that the resulting correlation can be evaluated consistently. To evaluate the quality of H_2 norm as a correlation metric, other correlation metrics (such as peak response frequency and amplitude) are compared to H_2 norm in Fig. 23 for several test geometries.

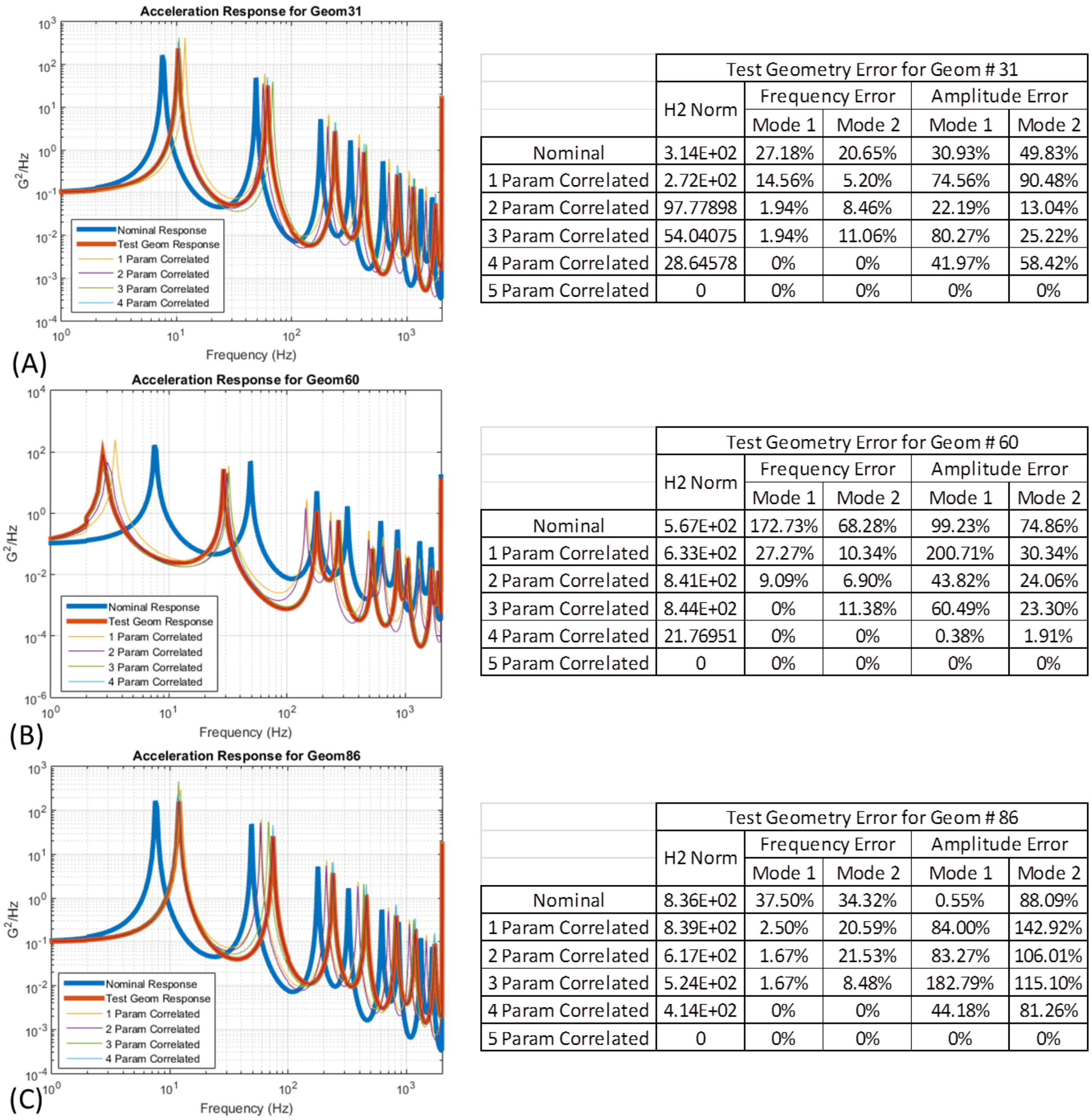

	Test Geometry Error for Geom # 31				
	H2 Norm	Frequency Error		Amplitude Error	
		Mode 1	Mode 2	Mode 1	Mode 2
Nominal	3.14E+02	27.18%	20.65%	30.93%	49.83%
1 Param Correlated	2.72E+02	14.56%	5.20%	74.56%	90.48%
2 Param Correlated	97.77898	1.94%	8.46%	22.19%	13.04%
3 Param Correlated	54.04075	1.94%	11.06%	80.27%	25.22%
4 Param Correlated	28.64578	0%	0%	41.97%	58.42%
5 Param Correlated	0	0%	0%	0%	0%

	Test Geometry Error for Geom # 60				
	H2 Norm	Frequency Error		Amplitude Error	
		Mode 1	Mode 2	Mode 1	Mode 2
Nominal	5.67E+02	172.73%	68.28%	99.23%	74.86%
1 Param Correlated	6.33E+02	27.27%	10.34%	200.71%	30.34%
2 Param Correlated	8.41E+02	9.09%	6.90%	43.82%	24.06%
3 Param Correlated	8.44E+02	0%	11.38%	60.49%	23.30%
4 Param Correlated	21.76951	0%	0%	0.38%	1.91%
5 Param Correlated	0	0%	0%	0%	0%

	Test Geometry Error for Geom # 86				
	H2 Norm	Frequency Error		Amplitude Error	
		Mode 1	Mode 2	Mode 1	Mode 2
Nominal	8.36E+02	37.50%	34.32%	0.55%	88.09%
1 Param Correlated	8.39E+02	2.50%	20.59%	84.00%	142.92%
2 Param Correlated	6.17E+02	1.67%	21.53%	83.27%	106.01%
3 Param Correlated	5.24E+02	1.67%	8.48%	182.79%	115.10%
4 Param Correlated	4.14E+02	0%	0%	44.18%	81.26%
5 Param Correlated	0	0%	0%	0%	0%

Fig. 23 H_2 norm comparison against Peak and Amplitude Error for First Two Modes for an arbitrary correlation order with (A) Geometry 31, (B) Geometry 60, and (C) Geometry 86.

The H_2 norm correlates well with the frequency and amplitude error calculated for the first two modes. The H_2 norm can also be seen as more stringent as the entire FRF bandwidth is required to be correlated and not a single point (natural frequency). The H_2 norm does not linearly reduce as the number of parameters is correlated, highlighting the complexity of this simple problem. That being said, Geometry #60, as seen in Fig. 23 (B), only requires four correlated parameters to reach an H_2norm of 21 and less than 5% error in both frequency and amplitude for the first two modes. This identifies that parameter five is not required to accurately correlate the full model for geometry 60. An inherent issue with the H_2 norm is the importance placed on the higher modes which may not be of interest in some applications. The final parameter correlated in the case shown in Fig. 23 is the global damping parameter. As can be seen, the amplitude error for all cases (except Geometry #60) is significant until all five parameters are correlated. This is a key discovery that demonstrates a difference between the $H2$ norm and the classic correlation method associated with modal frequency and amplitude error. This identifies a problem inherent in the use of the $H2$ norm evaluated across the full frequency spectrum. While this method is still sufficient for model correlation efforts, further investigation could be done to focus the correlation efforts on the lower modes by weighting the frequency spectrum to shift the importance towards the lower frequencies or possibly truncating the spectrum used for the actual Sensitivity matrix.

7.2 Evaluation of all Potential Ranking Correlations

The correlation methodology detailed in Table 6 is used to generate the data to evaluate the quality of all possible rankings. The output of this analysis is a $H2$ norm for 120 different rankings applied to 90 different geometries with 6 correlation states from 0 to 5 parameters correlated. This results in 64,800 individual FEM runs to generate an objective truth for this system. The metric used to compare the relative rankings is defined as the Correlation Norm Error metric. The Correlation Norm Error is generated by evaluating the plots seen in Fig. 24 and calculating the area under the curve or, equivalently, the sum of the H_2 norm for $1{:}n$ parameters correlated. To generate a normalized value, the area under the curve is reduced by the minimum area under the curve. This ensures that the optimal path has zero Correlation Norm Error. The results for specific geometries 13, 27, and 79 can be seen in Fig. 24 (A), (B), (C), respectively. The average result for all 90 geometries can be seen in Fig. 24 (D).

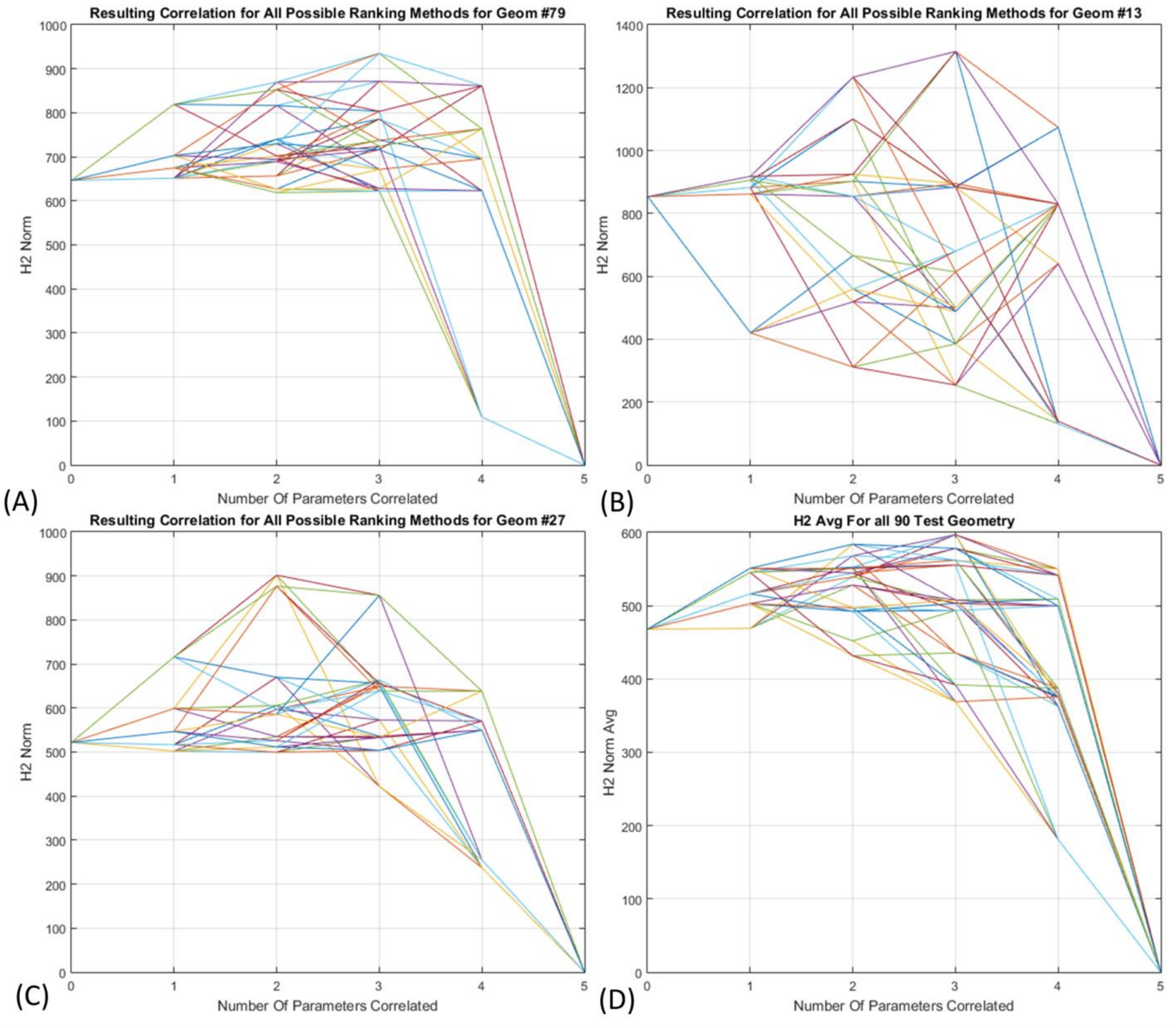

Fig. 24 All possible rankings as a function of parameters correlated for (A) Geom. #13, (B) Geom. #27, (C) Geom. #79, and (D) Averaged for the 90 Geometries of interest

As expected, the effectiveness of individual ranking varies significantly as a function of the geometry being analyzed. This variation is due to the random input parameters resulting in variability in the optimal ranking order for individual geometries. This is easily explained; in the example test case there is minimal change in a given parameter and the correlation impact of that parameter is expected to be minimal. For specific geometries like geometry 13, there is a clear path that can slowly decrease the error between the model and the test geometry. In Fig. 24 (B) and (C), the correlation of one or two parameters does not increase the correlation of the system due to the large initial correlation error. As seen in Fig. 24 (C), all of the correlation error is due to four parameters, so the only significant improvement occurs after all four parameters are correlated. Given that the "test" specimen is a simulation in which to test the methodology, it is also expected that the fifth parameter will always yield zero error.

Given these rankings, the Correlation Norm Error is used to determine the optimal correlation path. Using this methodology, it can be determined that the "true" optimal ranking order is [Thickness 1, Mass 2, Thickness 2, Mass 1, Damping]. The worst correlation path can be calculated to be [Mass 1, Damping, Thickness 2, Mass 2, Thickness

1]. It is worth noting, that the best and worst rankings are not exactly reverse orders of each other. For this five parameter geometry, the resulting optimal and worst ranking paths can be seen in Fig. 25.

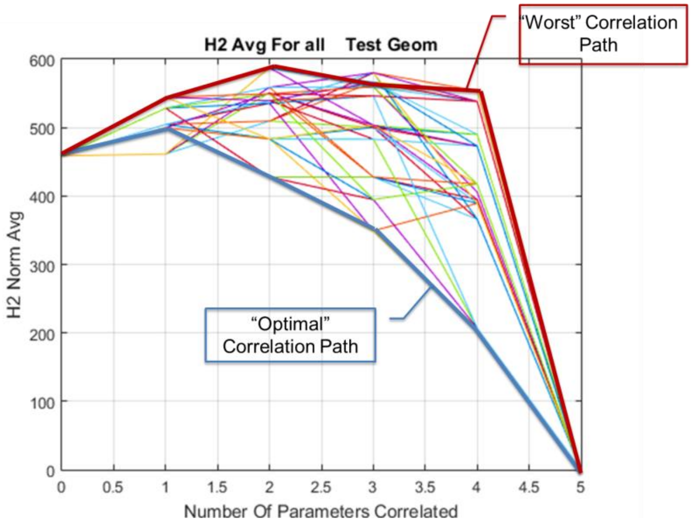

Fig. 25 Optimal and worst correlation path for all test geometries.

As was originally hypothesized, no single path is optimal at all points. If a single path existed, it would decrease the number of rankings of importance from 120 to 25, for instance if parameter #2 is in the single optimal parameter set, it must also be contained in the optimal two parameter set. As shown, this simplification cannot be made for this problem, requiring a significantly more complex and computationally expensive effort to determine the optimal correlation path. The resulting optimal path identification method for a five parameter system requires the generation of 64,800 models. This makes the identification of the optimal ranking through the use of brute force calculation too expensive for practical use. To achieve "truth" for a ten-parameter system, using the same method requires 3.6×10^9 FEM runs. This highlights the impractical nature of the use of truth for anything but the methodology investigation. This result further informs the need for effective, computationally inexpensive methods to determine a 'good enough' ranking of parameters.

7.3 Engineering Judgment

Engineering judgment alone for the use of parameter identification has several flaws, but nevertheless it is required to identify the initial parameter set and determine the error bounds in this methodology. To better understand the variability in the engineering judgment ranking, 16 engineers were asked to provide their ranking of parameter importance. The engineers chosen for this investigation represent an experienced and well-educated group in the field of vibrations, testing, and modelling. Their responses are shown in Table 7.

Table 7 Engineering Judgment ranking by 16 experienced engineers with resulting Correlation Norm Error.

	Optimal Ranking	Worst Ranking	Correlation Order Provided by Experienced Engineers															
			Eng 1	Eng 2	Eng 3	Eng 4	Eng 5	Eng 6	Eng 7	Eng 8	Eng 9	Eng 10	Eng 11	Eng 12	Eng 13	Eng 14	Eng 15	Eng 16
Correlation Param 1	3	1	2	3	5	5	5	5	5	5	2	2	2	2	5	2	3	2
Correlation Param 2	2	5	1	4	2	3	3	2	2	2	3	1	4	4	2	1	4	5
Correlation Param 3	4	4	5	2	4	4	4	1	4	1	5	4	3	5	3	3	2	3
Correlation Param 4	1	2	3	5	3	2	2	3	1	4	1	3	1	3	1	4	1	4
Correlation Param 5	5	3	4	1	1	1	1	4	3	3	4	5	5	1	4	5	5	1
Correlation Norm	**0.0**	**770.0**	**560.9**	**215.0**	**512.1**	**378.7**	**378.7**	**495.1**	**699.5**	**664.7**	**315.4**	**348.1**	**163.3**	**585.9**	**362.8**	**184.7**	**20.3**	**440.4**

The engineering judgment ranking, detailed in Table 7, has significant variation. Furthermore, Engineer 7 was able to match correctly three of the five parameters in the optimal parameter rank, but the ranking resulted in the worst overall Correlation Norm error. This is indicative that a high-quality ranking is reliant on the identification of the most and least important parameters. To better understand how these rankings perform relative to all potential rankings, the engineering ranking paths are plotted in Fig. 26 (A) and the Correlation Norm Error is plotted in Fig. 26 (B).

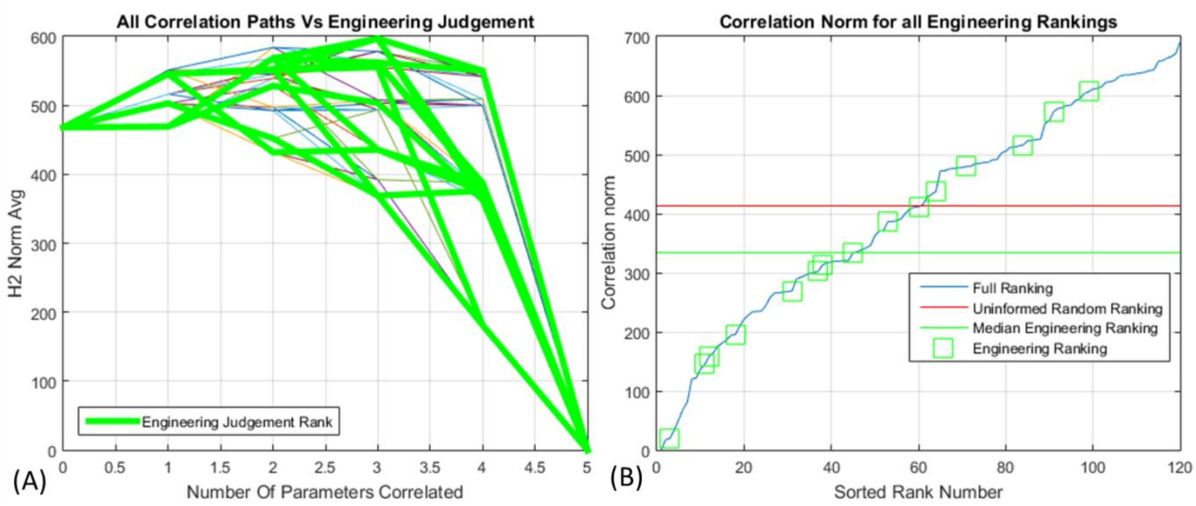

Fig. 26 Engineering judgment investigation into (A) All correlation paths. (B) Correlation Norm Error vs. engineering rankings.

As shown, the median professional engineering judgment ranking correlates better than random choice, but for a simple system engineering judgment was expected to perform better. The random ranking results in a Correlation Norm Error of 413.3 while engineering judgment produces a Correlation Norm Error of 334.3, resulting in an improvement in the relative Correlation Norm Error of 79 compared to random. As the number of parameters increase, a corresponding decrease in the quality of the engineering judgment is expected.

7.4 Ranking Method Evaluation

While the quality of the ranking is of paramount importance, the computational cost must also be taken into account. While large numbers of runs were used to investigate the quality of the reduction methods in question, relatively few computations were required to generate the ranking for this simple system. For this geometry, the full set of all possible coupled parameters was investigated resulting in a total of 3^5 or 243 coupling combinations. As demonstrated in Table 4 and Fig. 19, several subdivisions were chosen for further investigation. These include simultaneous two parameter coupling cases, three parameter coupling cases, four parameter coupling cases and, finally, all potential variations of the parameters set to the max-min and nominal values as dictated by the error bounds. These subdivisions result in 10, 50, 130, 210 and 243 individual FEM runs that are used to generate the input data set. To evaluate the quality of the ranking against the computational cost the ranking quality vs. the number of FEM runs required to produce that ranking are plotted in Fig. 27.. The calculation used to generate the True ranking requires the most FEM run (64800), and the engineering judgment ranking requires the least (0). Each ranking and weighting method combination computational cost is based on the six different sized sensitivity matrix sizes, detailed in Fig. 19 and Table 4. This allows the selection of a method and an input size that balances the computational cost with the resulting ranking quality. The resulting quality and computational cost from the 68 ranking method combinations are seen in Fig. 27.

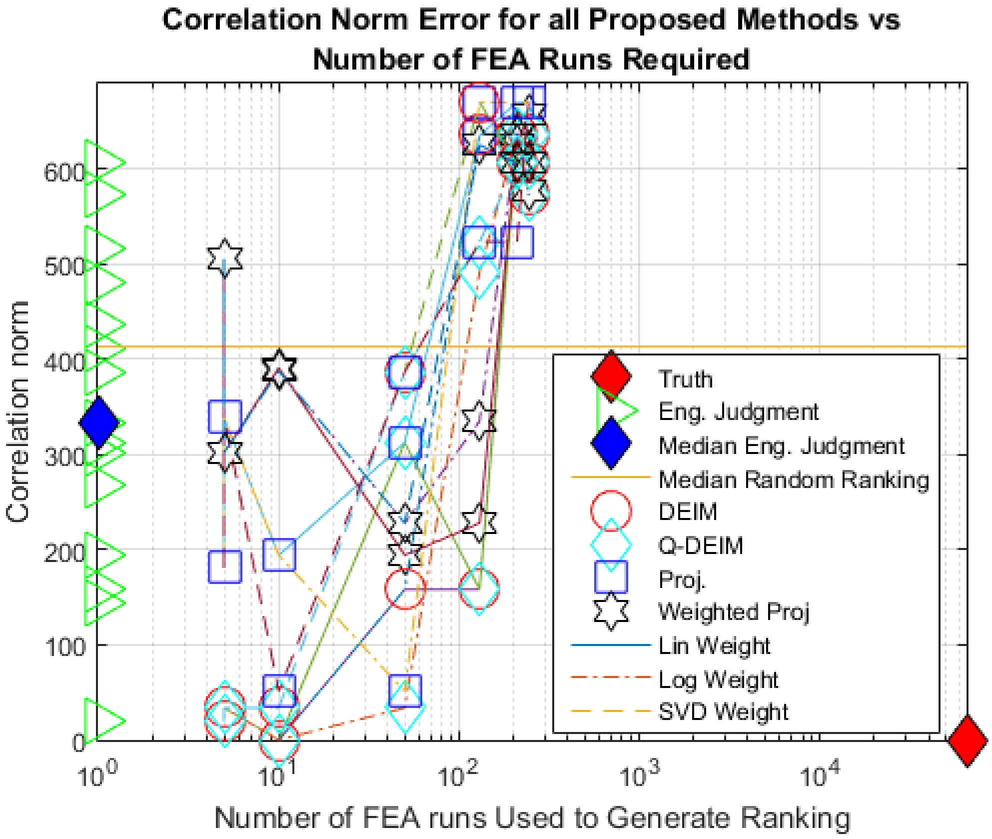

Fig. 27 Area under the Curve Error as a function of Computational Effort Required to Calculate Ranking.

From Fig. 27, the resulting ranking quality for engineering judgment, truth, and the proposed methodology can be seen. For all cases, an increase in the size of the input set increases the quality of the correlation up to a point. The optimal location varies with each method, but all cases have a poorer correlation using 210 input points than the 130 input case. While this is not entirely understood, it is suspected that the inclusion of higher order coupling provides no valuable insights into the dynamics of the problem, instead deteriorating the quality of ranking. The computational cost of the methodology presented, highlights the impracticality of defining the optimal ranking using “True” as it requires 64,000 FEM model evaluations.

As can be seen, the lowest error method is either the Q-DEIM or DEIM method. However, the robustness of the method to errors in the inputs needs to be understood before identification of the optimal ranking method is possible. For this reason, an investigation into the ranking quality as a function of uncertainty in the error bounds is performed. This determines if the methodology presented herein is robust to incorrect assumptions concerning the initial error bounds. This simple system requires only the low computational cost of solving between 5 and 243 FEM, depending on the method chosen. For a system with an increased number of parameters, the required increase in computational cost would be significant. For larger parameter sets, there is a practical limit to the number of possible FEM iterations. This will be discussed in reference to the resulting quality and robustness of the various methods proposed for future use.

8. Error Bound Investigation

The error bounds in this example are subject to manufacturing tolerances, material uncertainty and user judgment errors. The error bound choices have a significant effect because the scale of the parameter change used in this methodology is based on the error bound assumptions. To better understand the impact of the error bounds on this methodology, a further investigation into the uncertainty in the initial error bound assessment is completed. The resulting ranking robustness is evaluated on ten randomly generated error bounds with the randomized uncertainty contained within [5%, 10%, 25%, 50%, and 75%]. To generate the ten unique 5% error bound uncertainty cases, each parameter's error bound input is randomly varied between 95% and 105% of the original error bound value. The ten resulting Sensitivity Input matrices are used to generate 68 new parameter rankings. The resulting ranking from this evaluation examines the change in ranking quality as a function of the Correlation Norm Error. This is done for all model reduction methods, all weighting methods and for all five error bound uncertainty values as can be seen in Fig. 28.

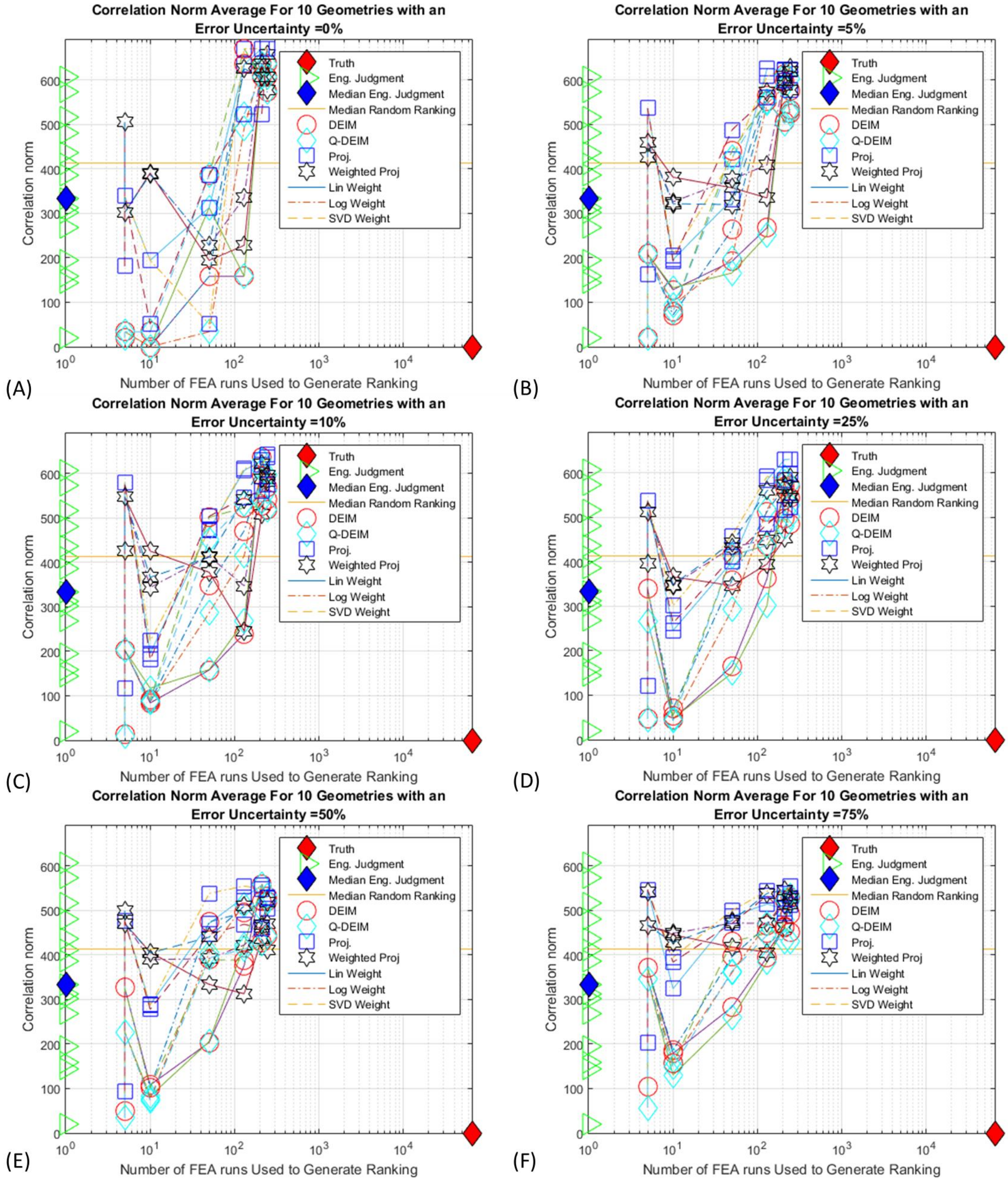

Fig. 28 Evaluation of Model Reduction Methods Quality with Errors in Initial error bound Assumptions

The resulting quality of the correlated model is dependent on the initial assumptions regarding the assumed error bounds. As error bound uncertainty increases, the ranking quality decreases, as expected. Overall, the quality of the resulting ranking is high even with large uncertainties associated with the original error bound assumptions. While the figure provides information regarding the resulting ranking quality under a variety of error bound uncertainties, hypothesis testing is used to investigate the quality of each ranking method.

8.1 Hypothesis Testing

Upon completion of the error bound investigation, the 68 ranking variations were run on ten geometries for each of the five uncertainty values. This results in a total of 40,80 unique runs. To determine what method is best, a statistical investigation is done. An analysis of variance (ANOVA) is carried out followed by a multiple comparison test (Tukey test). All other variables are held constant during this analysis.

The ANOVA analysis is used to analyze the differences in group means and ultimately if a difference between group means exists [40, 41] the mean correlation errors are examined. In this analysis, a null hypothesis is tested and is either accepted or rejected. The null hypothesis is that all treatments of the data will result in the same mean correlation error. That is, there is no difference between using any model reduction algorithm to rank the parameters. ANOVA rejects the null hypothesis if the recorded mean error is statistically improbable under the assumption that all the means are the same. The threshold to determine what is statistically significant is chosen to be 95 %, which is customary in an ANOVA analysis.

The purpose of completing multiple comparison tests is to understand which group performed best if the ANOVA concludes that there is a difference in performance between groups. A Tukey multiple comparison test is chosen for the analysis as it has been proven to be robust to recognizing power differences for a small number of groups and is a commonly used comparison test [42]. The Tukey test compares all pairs of means for similarity within some confidence interval, again chosen as 95 % in this analysis.

Hypothesis testing on the data, as seen in Fig**.** 29, is done to quantify the results shown in Fig. 28. This provides insight into the statistical properties of the resulting rankings as a function of weighting, model reduction method, the input data size and the uncertainty in the error bound. This is done for all of the ten randomized geometries used to generate the average responses seen in Fig. 28. This work defines the optimal operating cases and identifies the best operating methods for this process.

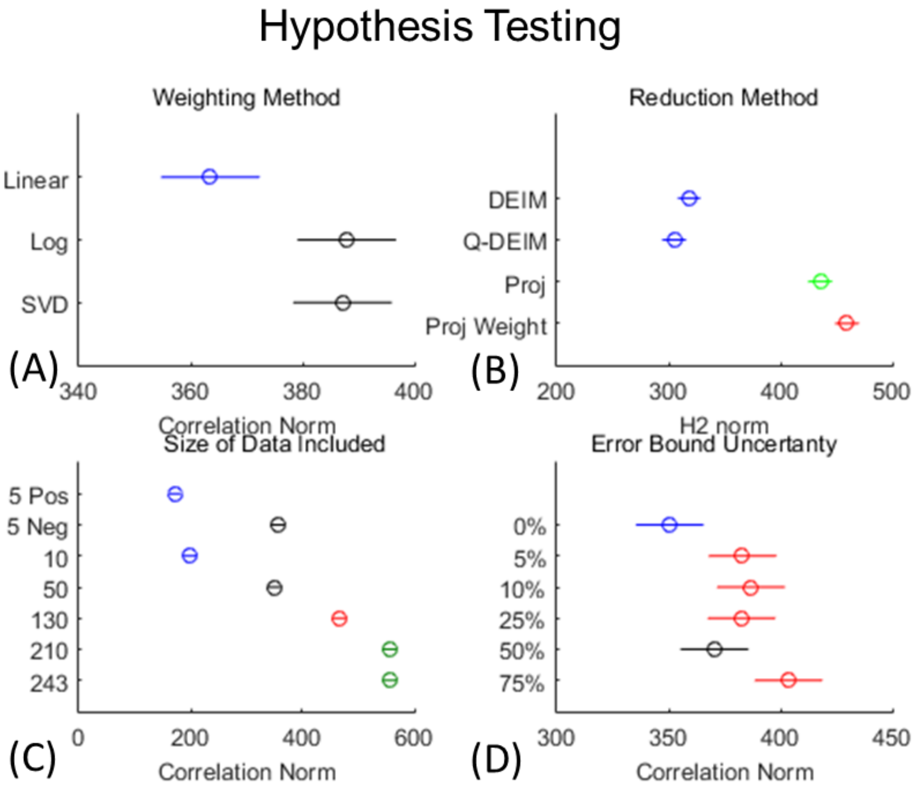

Fig. **29** Hypothesis testing to statistically evaluate the optimal Weighting Method (A), the optimal Model Reduction Method (B), the optimal Amount of Included Data (C) and the Error Impact due to the error bound Uncertainty (D).

As seen in Fig. 29 (A), the linear weighting method produces reduced H_2 norms relative to the other weighting methods. The model reduction method in Fig. 29 (B), highlights that the Q-DEIM and DEIM method are not statistically distinguishable from each other, but instead, both perform better than Projection and Weighted Projection. The results from Fig. 29 (C) indicate that the 10 parameter input and the 5 parameter positive input are the best performing data inputs. This is interesting as it is not understood why the input case using the positive end of the error bounds produces better results than the use of the negative side of the error bounds. As is expected, in Fig. 29 (D) the quality of the models follows a general trend of reduced quality as the uncertainty is increased. The variations are due to the random nature in the development of the error bound uncertainty.

Through the hypothesis testing, the optimal cases for all input variations can be deduced. As shown in Fig. 29 (A), linear weighting provides the best weighting method. The use of Q-DEIM and DEIM are statistically shown to be the best reduction algorithms in conjunction with five positive inputs. The two best input scale cases for each reduction method are plotted in Fig. 30.

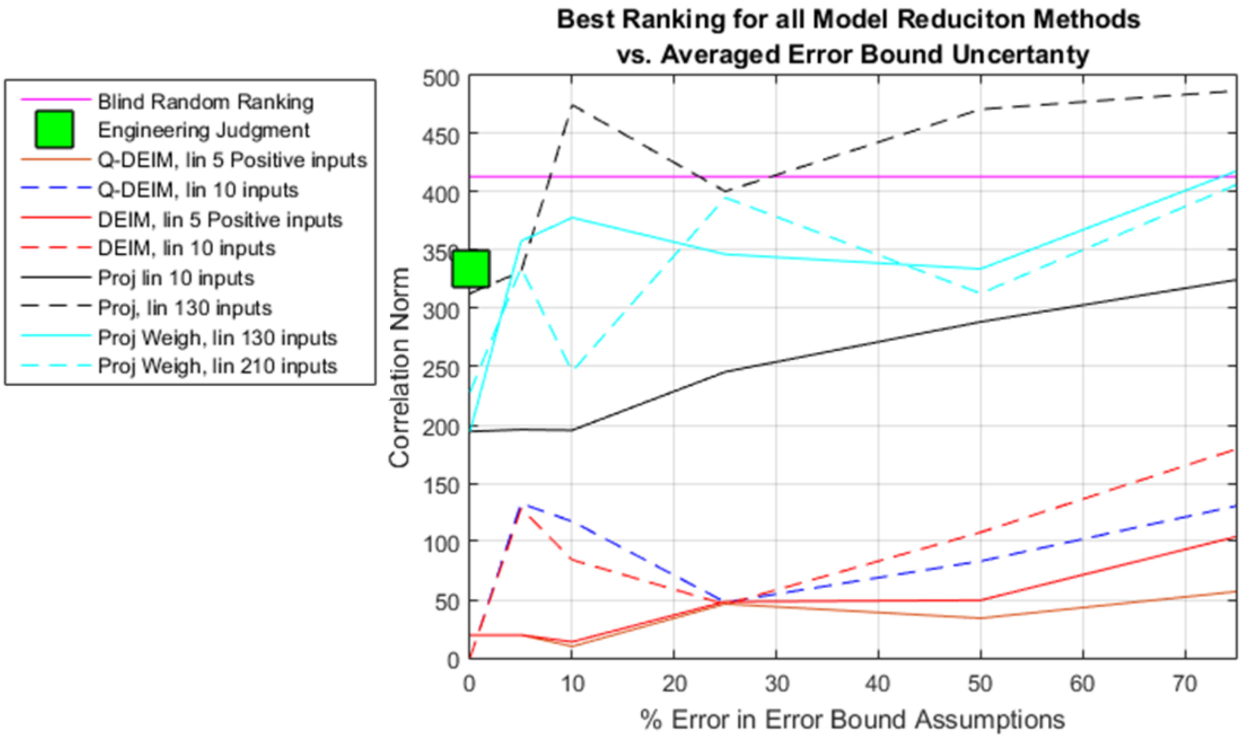

Fig. 30 Best performing parameter ranking algorithms averaged over ten geometries compared to errors in the Error bound assumptions.

As seen in Fig. 30, all methods reduce in quality as the uncertainty in the error bounds increase. It can be seen that Q-DEIM and DEIM produce similar results as was expected from hypotheses testing. A significant reduction in quality occurs for Projection and Weighted Projection. This demonstrates that Projection at 130 points and Projection Weighted are worse than engineering judgment with a given uncertainty of 10%. Overall it can be seen that the use of Q-DEIM and DEIM produce high-quality rankings even with large uncertainties in the error bounds. To better understand this, Fig. 31 investigates the response for each of the 10 test geometries used to generate the data seen in Fig. 30 using Q-DEIM as the ranking method.

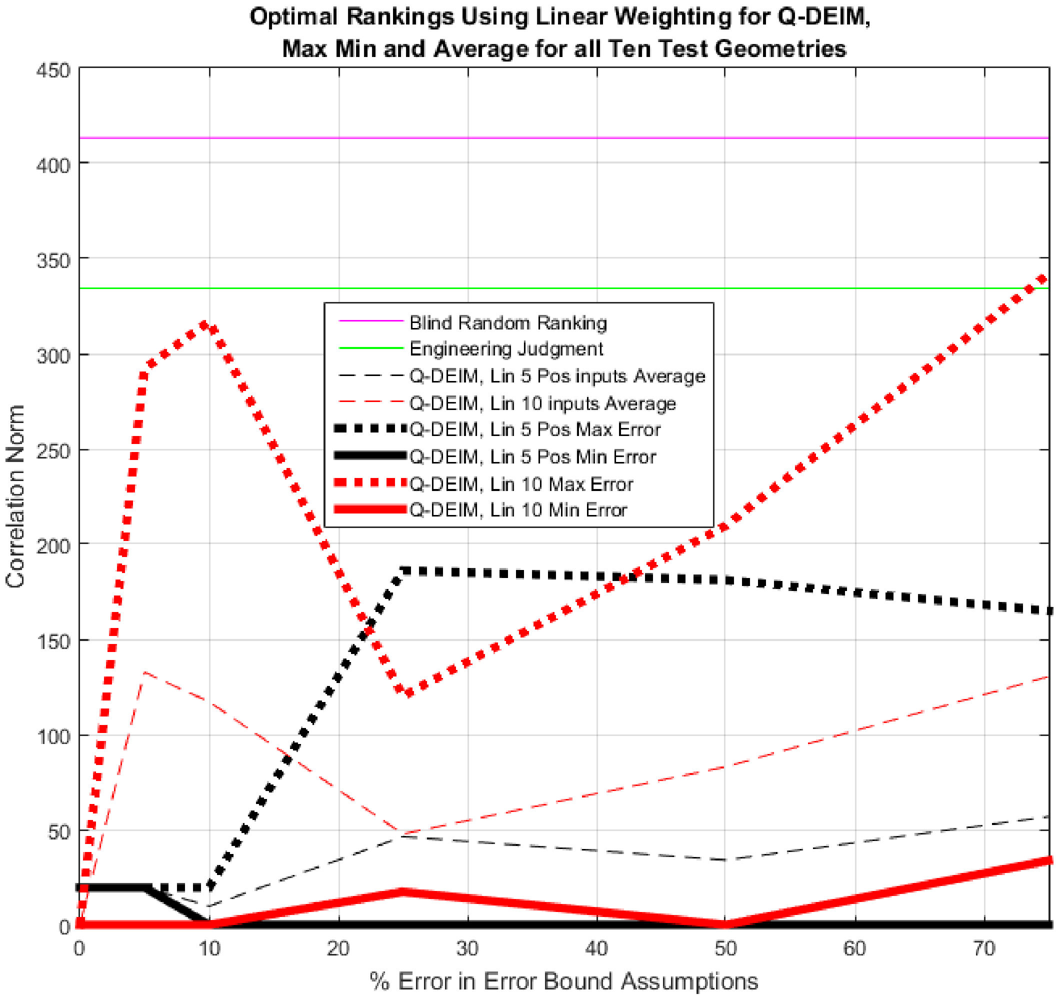

Fig. 31 Maximum, minimum, and average errors using two ranking methods for the ten rankings using Q-DEIM as a function of errors in the error bound Assumptions

By investigating the individual test geometries, it can be seen that outliers exist, but all cases below 75% uncertainty improve on engineering judgment. It should also be noted that there is no practical way to evaluate the uncertainty effect on engineering judgment, which would be expected to also increase with increased uncertainty but it is not addressed in this work. This study has shown robustness to errors and uncertainty in the engineering judgment associated with error bound development. Overall, this system has shown improvement on current methods with low computational cost.

Acknowledgements

I gratefully acknowledge the support of The Naval Center For Space Technology at the Naval Research Lab for their financial support through the Select Graduate Training Program. In developing the ideas presented here, I have received helpful conceptual input from Thanh Pham, Dr. George Kirby, Todd Krafchak and invaluable Q-DEIM algorithm assistance from Dr. Mark Embree and Dr. Serkan Gugercin. The authors would also like to thank the anonymous engineers who supplied their engineering judgement to be evaluated.

Conclusion

The methodology for parameter ranking, described in this paper, has been shown to be accurate, computationally efficient and reliable. The ranking used shows significant improvement over engineering judgment. This paper also demonstrates an improvement in the field of sensitivity analysis and has proven to be a viable method for parameter ranking. The resulting correlation method has been demonstrated and quantified using the Correlation Norm Error. Every possible ranking was calculated such that the optimal and worst case could be known, and the methodology could be compared. For this system, it was shown that the optimal ranking is [Thickness 1, Mass 2, Thickness 2, Mass 1, Damping]. This optimal ranking is correctly predicted through the use of the methodology proposed. The use of Q-DEIM in conjunction with a ten-parameter input set and linear weighting can predict the optimal case. Further work is needed to ensure that this specific ranking method proposed for this geometry holds for other more complex geometries but a substantial statistical analysis has confirmed its potential.

The quality of engineering judgment was quantified with the help of 16 engineers who provided their assessments of the optimal correlation order for this problem. To compare with engineering judgment, the true optimal and worst ranking were calculated by generating results for all 120 possible rankings as a function of the number of parameters correlated. Blind random evaluations lead to a Correlation Norm Error of 413.3 and engineering judgment produces a Correlation Norm Error of 334.3. This results in an improvement of the Correlation Norm Error of 79 compared to random with the use of engineering judgment. The use of Q-DEIM with a linear weight and ten input parameters produces a relative Correlation Norm Error of 0 resulting in an improvement of 413.3 over random and 334.4 improvement over engineering judgment. As shown, the quality of the ranking degrades as larger uncertainties are applied to the initial error bounds.

The robustness of the method is evaluated against uncertainty in the initially applied error bound. To achieve this, ten error bounds were generated using a randomly varied error bound with the variance limited between 0%, 5%, 10%, 25%, 50%, and 75%. These newly developed error bounds were used to generate 68 unique rankings. Those 68 rankings were calculated for each of the ten geometries and each of the six uncertainty values resulting in 4080 rankings. Through hypothesis testing, the Q-DEIM and DEIM rankings using linear weighting and five positive or 10 inputs is proven to be robust to changes in the uncertainty of the error bounds, proving the robustness of the method.

References

1. Tarazaga, P., Y. Halevi, and D. Inman. *Model updating with the use of principal submatrices*. in *Proceedings of the 22nd International Modal Analysis Conference*. 2004.
2. Tarazaga, P.A., Y. Halevi, and D.J. Inman. *Model Updating Using a Quadratic Form*. in *ASME 2005 International Design Engineering Technical Conferences and Computers and Information in Engineering Conference*. 2005. American Society of Mechanical Engineers.
3. Tarazaga, P., Y. Halevi, and D. Inman, *The quadratic compression method for model updating and its noise filtering properties.* Mechanical systems and signal processing, 2007. 21(1): p. 58-73.
4. Friswell, M. and J.E. Mottershead, *Finite element model updating in structural dynamics*. Vol. 38. 1995: Springer Science & Business Media.
5. Mayes, R.L. *Model Correlation and Calibration*. in *Proceedings of the 27th International Modal Analysis Conference*. 2009.
6. Farhat, C. and F.M. Hemez, *Updating finite element dynamic models using an element-by-element sensitivity methodology.* AIAA journal, 1993. 31(9): p. 1702-1711.
7. Mayes, R.L., et al. *A Structural Dynamics Model Validation Example with Actual Hardware*. in *Proceedings of the 27th International Modal Analysis Conference*. 2009.
8. Mottershead, J.E., M. Link, and M.I. Friswell, *The sensitivity method in finite element model updating: a tutorial.* Mechanical Systems and Signal Processing, 2011. 25(7): p. 2275-2296.
9. Ferregut, C.M., R.A. Osegueda, and J. Ortiz. *Artificial neural networks for structural damage detection and classification*. in *Smart Structures & Materials' 95*. 1995. International Society for Optics and Photonics.

10. Zhao, J., J.N. Ivan, and J.T. DeWolf, *Structural damage detection using artificial neural networks.* Journal of Infrastructure Systems, 1998. 4(3): p. 93-101.
11. Farrar, C.R. and K. Worden, *Structural health monitoring: a machine learning perspective*. 2012: John Wiley & Sons.
12. Sarlo, R. and P.A. Tarazaga, *A Neural Network Approach to 3D Printed Surrogate Systems*, in *Topics in Modal Analysis & Testing, Volume 10: Proceedings of the 34th IMAC, A Conference and Exposition on Structural Dynamics 2016*, M. Mains, Editor. 2016, Springer International Publishing: Cham. p. 215-222.
13. Lim, J.H., *A correlation study of satellite finite element model for coupled load analysis using transmissibility with modified correlation measures.* Aerospace Science and Technology, 2014. 33(1): p. 82-91.
14. Homma, T. and A. Saltelli, *Importance measures in global sensitivity analysis of nonlinear models.* Reliability Engineering & System Safety, 1996. 52(1): p. 1-17.
15. Iooss, B. and P. Lemaître, *A review on global sensitivity analysis methods*, in *Uncertainty Management in Simulation-Optimization of Complex Systems*. 2015, Springer. p. 101-122.
16. Ross, C.F., et al., *Modeling masticatory muscle force in finite element analysis: sensitivity analysis using principal coordinates analysis.* The Anatomical Record Part A: Discoveries in Molecular, Cellular, and Evolutionary Biology, 2005. 283(2): p. 288-299.
17. Ackermann, S., et al., *Principal component analysis for detection of globally important input parameters in nonlinear finite element analysis.* Optimisation and Stochastic Days, 2008. 5.
18. Calvi, A., *Uncertainty-based loads analysis for spacecraft: Finite element model validation and dynamic responses.* Computers & structures, 2005. 83(14): p. 1103-1112.
19. Borgonovo, E., *A new uncertainty importance measure.* Reliability Engineering & System Safety, 2007. 92(6): p. 771-784.
20. Austin Phoenix, D.B., Rodrigo Sarlo, Thanh Pham, and Pablo A. Tarazaga, *Optimal Parameter Identification for Model Correlation using Model Reduction Methods*, in *IMAC-XXXIV-Dynamics of Multiphysical Systems: From Active Materials to Vibroacoustics*. 2016, Springer: Orlando Fl.
21. D.B. Bales, P.A.T., M.E. Kasarda, D. Batra, A.G. Woolard, J.D. Poston, V.V.N.S. Malladi, , *Gender Classification of Walkers Via Underfloor Accelerometer Measurements.* IEEE Internet of Things Journal, 2016.
22. Snape, G., S. Clift, and A. Bramley, *Parametric sensitivity analyses for FEA of hot steel forging.* Journal of materials processing technology, 2002. 125: p. 353-360.
23. Snape, R., S.E. Clift, and A.N. Bramley, *Sensitivity of finite element analysis of forging to input parameters.* Journal of Materials Processing Technology, 1998. 82(1): p. 21-26.
24. Mottershead, J., et al., *Geometric parameters for finite element model updating of joints and constraints.* Mechanical Systems and Signal Processing, 1996. 10(2): p. 171-182.
25. Dascotte, E. and J. Strobbe. *Updating finite element models using FRF correlation functions*. in *17th International Modal Analysis Conference, Kissimmee, FL*. 1999.
26. Karamchandani, A. and C. Cornell, *Sensitivity estimation within first and second order reliability methods.* Structural Safety, 1992. 11(2): p. 95-107.
27. Haukaas, T. and A. Der Kiureghian, *Parameter sensitivity and importance measures in nonlinear finite element reliability analysis.* Journal of engineering mechanics, 2005. 131(10): p. 1013-1026.
28. Lund, B.F. and B.A. Foss, *Parameter ranking by orthogonalization—Applied to nonlinear mechanistic models.* Automatica, 2008. 44(1): p. 278-281.
29. McLean, K.A., S. Wu, and K.B. McAuley, *Mean-squared-error methods for selecting optimal parameter subsets for estimation.* Industrial & Engineering Chemistry Research, 2012. 51(17): p. 6105-6115.
30. Kuo, W. and X. Zhu, *Importance measures in reliability, risk, and optimization: principles and applications*. 2012: John Wiley & Sons.
31. Ewins, D., *Modal testing: theory, practice and application (mechanical engineering research studies: engineering dynamics series).* 2003.
32. Chaturantabut, S. and D.C. Sorensen. *Discrete empirical interpolation for nonlinear model reduction*. in *Decision and Control, 2009 held jointly with the 2009 28th Chinese Control Conference. CDC/CCC 2009. Proceedings of the 48th IEEE Conference on*. 2009. IEEE.
33. Sorensen, D.C. and M. Embree, *A DEIM Induced CUR Factorization.* arXiv preprint arXiv:1407.5516, 2014.
34. Drmac, Z. and S. Gugercin, *A New Selection Operator for the Discrete Empirical Interpolation Method--improved a priori error bound and extensions.* arXiv preprint arXiv:1505.00370, 2015.

35. Francis, J.G., *The QR transformation—part 2.* The Computer Journal, 1962. 4(4): p. 332-345.
36. Perinpanayagam, S. and D. Ewins. *Test Strategy for Component Modal Test for Model Validation*. in *Proceedings of the International Conference on Noise and Vibration Engineering ISMA*. 2004.
37. Chen, G., *FE model validation for structural dynamics*. 2001: University of London.
38. Dwork, C., et al. *Rank aggregation methods for the web*. in *Proceedings of the 10th international conference on World Wide Web*. 2001. ACM.
39. Lin, S., *Rank aggregation methods.* Wiley Interdisciplinary Reviews: Computational Statistics, 2010. 2(5): p. 555-570.
40. Fisher, R.A., *On the "Probable Error" of a Coefficient of Correlation Deduced from a Small Sample.* 1921.
41. Fisheh, R., *On the «Probable Error» of a coefficient of correlation deduced from a small sample.«.* Metron, 1921. 1(Pt 4): p. 1-32.
42. Tukey, J.W., *Comparing individual means in the analysis of variance.* Biometrics, 1949: p. 99-114.

Thermal Morphing Anisogrid Smart Space Structures Part 1: Introduction, Modeling, and Performance of the Novel Smart Structural Application.

Austin A. Phoenix
United States Naval Research Lab, Naval Center for Space Technology

Pablo A. Tarazaga
Virginia Tech, Vibrations, Adaptive Structures, and Testing Lab
310 Goodwin Hall, Blacksburg, VA, 24060

Abstract: To meet the requirements for the next generation of space missions, a paradigm shift is required from current structures that are static, heavy and stiff, to innovative structures that are adaptive, lightweight, versatile, and intelligent. The largest benefit provided by this new structural concept is in the ability to deliver high precision position stability. The conventional high precision structural design uses two decoupled systems to achieve positional stability. First, a high mass structure delivers the effectively infinite stiffness and thermal stability so that no deformations occur under all operational loading conditions. Second, to meet the morphing and on-orbit positional requirements, a supplementary mechanisms provide the micro and macro displacement control required. This paper proposes the use of a novel morphing structure, the thermally actuated anisogrid morphing boom, to meet the design requirements through actively morphing the primary structure in order to adapt to the on-orbit environment and meet both requirements in a consolidated structure. The proposed concept achieves the morphing control through the use of thermal strain to actuate the individual helical members in the anisogrid structure. Properly controlling the temperatures of multiple helical members can introduce six Degree of Freedom (DOF) morphing control. This system couples the use of low Coefficient of Thermal Expansion (CTE) materials with precise thermal control to provide the high precision morphing capability. This concept has the potential to provide substantial mass reductions relative to current methods and provide a way to meet the high precision displacement requirements of spacecraft systems. This paper will detail the concept itself, demonstrate the modeling procedure, and investigate the design space to quantify the potential of the thermally morphing anisogrid smart structure.

1. Introduction

While the field of smart adaptive structures has been well established in the spacecraft community, new adaptive structures are essential to meet the requirements for the next generation of space missions. In recent years, significant effort has been expended on the development of smart structures to address vibration isolation, thermal distortion, deployment control, and to provide intelligent environment control capability [1-17]. The introduction of adaptive, or morphing, capabilities to address the system requirements, relaxes the structural stiffness requirements resulting in significant mass savings. This mass saving provides significant cost savings and enable new mission architectures. The purpose of this work is to expand the capability of current adaptive structures, in order to build smart structure systems that meet the on-orbit design requirements by actively adapting to the changing environment. The present structural paradigm is to achieve static displacement, thermal distortion stability, and dynamic design requirements through the application of stiff, thermally invariant, heavy primary structures with secondary adaptive systems. This work is focused on developing a mass-efficient, integrated and active structure that can provide low-frequency vibration isolation and thermal distortion corrective control, while also meeting high-precision alignment and position control requirements. This morphing capability can be used to correct on-orbit alignment, manufacturing error, and structural, or thermal, distortion. The primary motivation of this initial study is to define the performance limits of the thermal morphing anisogrid structures.

The anisogrid morphing concept expands on well-established smart structural systems like the hexapod; also known as the Steward platform [18]. The anisogrid structure taken to its most basic element is a hexapod system. Hexapods have been implemented to deliver 6 DOF morphing control. The traditional kinematic hexapod system consists of six actuating legs that are connected with unconstrained rotational degrees of freedom to two parallel surfaces. As the six legs are actuated, the two surfaces' relative position and angle can be controlled in all six degrees of freedom. A recent example of the hexapod technology can be seen in the implementation of the hexapod system in telescopes

[19]; specifically the Hobby-Eberly Telescope [20-22]. The thermal morphing hexapod, discussed by the authors in [23], introduces rotational constraints in conjunction with thermal strain actuation to improve the minimum morphing capability. The thermal morphing anisogrid boom concept discussed here, expands and improves upon the thermal morphing hexapod concept through the introduction of increased structural coupling and a more complex actuation vector. These changes result in a distributed actuation force that reduces global deformation through the dissipation of strain energy in local deformations. A significantly reduced morphing displacement relative to the length of the input actuation can be achieved by this method.

This work proposes the use of thermal strain as the sole actuation mechanism to achieve six Degree of Freedom (DOF) morphing capability. The ability to achieve high precision morphing is possible through the use of low Coefficient of Thermal Expansion (CTE) materials in conjunction with a highly accurate thermal control system. To morph to the desired position, thermal gradients are applied to the helical members in the system to generate local and global thermal strains, which pushes and pulls the system into the desired configuration. The use of thermal strain as an actuation mechanism has been studied at the micro [24-31] and macro level [31-34] for both bi-material [31-35] and bistable structures [30, 36, 37]. This paper will investigate the capability of this novel thermal morphing anisogrid structure which can deliver both micro and macro morphing deformations. This paper will demonstrate the novel anisogrid concepts ability to meet design requirements through precise structural morphing control.

A parameterized Finite Element Model (FEM) was developed to generate, run, and evaluate the geometric configurations of interest for this work. The FEM is developed using linear assumptions where temperatures are directly applied to the system. These modeling assumptions allow superposition to be used to combine the base set of FEM outputs to create the large set of displacements used to evaluate the workspace and calculate the minimum morphing capability in all six degrees of freedom. This parameterized FEM code is used to sweep through the critical geometric parameters such that the parameters impact on the morphing quality and scale is defined. This parameter sweep will be used to indicate the morphing potential of the concept as well as better define the design space.

This paper will work to detail the concept, discuss the anisogrid geometry's heritage, and detail the structures potential for this thermal morphing concept. The parameterized FEM was developed to evaluate the material normalized single helical unit thermal strain morphing cases; the workspace and minimum morphing capability will also be discussed. A study into the thermal control requirements versus geometric morphing accuracy will be performed for three materials: low CTE carbon composite, invar, and aluminum. Finally, the nine parameter design space will be investigated and future work will be discussed.

2. Morphing Concept Explanation

The intent of the thermal morphing anisogrid concept is to replace the current structural paradigm, that consists of a heavy and rigid primary structure coupled with a secondary morphing system by using smart adaptive primary structure. This is achieved by integrating the adaptive capability directly into the primary structure. The adaptive structural concept achieves design requirements by predicting and adapting to thermal and structural loading environments in real time. This adaptive capability is achieved through the use of thermal strain as the active actuation mechanism to control the lengths of helical members in the anisogrid structure. High precision morphing is created through the use of low CTE materials and precisely controlled applied temperatures. The thermal morphing anisogrid structure is an evolution of the thermal morphing hexapod concept previously detailed by the authors [23]. The thermal morphing hexapod uses thermal gradients in each of its six legs to provide thermal strain as the actuation mechanism to enable six DOF morphing capabilities. The anisogrid structure uses each helical member as an active actuator to provide a multi-directional thermal strain vector in a constrained structure. By introducing structural coupling and a multi-directional thermal strain, the system can produce smaller displacements per applied thermal strain. While the introduction of structural coupling improves the structural control capability, it also introduces thermal coupling. In the intended space-based environment, standard radiation shielding and the absence of an atmosphere removes the radiation and convective coupling thermal losses. The conductive coupling that occurs at helical interface locations will have a significant effect, but it can be mediated through the material or structural choices that limit the conduction at those interfaces. Future work must address the impacts and mitigation of the convective coupling effects.

3. Anisogrid Structure

The tubular anisogrid structure is the complex structure under investigation. This geometrically complex structure has recently become more viable due to improvements in manufacturing capabilities [38, 39] and has shown great promise in structural applications where a lightweight structure is of critical importance [38-48]. The anisogrid structure is made up of three structural components, the clockwise helical tubular members, the counterclockwise helical tubular members, and the circumferential tubular members, as seen in Figure 32. The anisogrid has four buckling failure modes: global buckling, global wall buckling, local tube buckling, and local tube wall buckling. For structural applications, the overall geometry, including the helical and cylindrical cross sections, would be sized to achieve optimally reduced mass by ensuring all buckling failure load cases occur at the same input load. The low mass thermal morphing anisogrid case will not be constrained by the optimal mass condition to evaluate the limits of the morphing capability.

3.1 Anisogrid Geometric Parameters of Interest

To investigate this concept, a one-meter tall anisogrid structure's morphing capability is evaluated as a function of its geometric parameters. These parameters are listed in Table 8. The nine parameters, detailed in Figure 32, are given both maximum and minimum allowed values. The model uses material normalization in the load and model development, when possible, to allow for the evaluation of multiple materials using a single FEM. This is not possible in the development of the element stiffness parameters where the Young's Modulus for invar is used. The use of any other material requires scaling of the cross sections to ensure element axial and bending stiffness values are correct, and to ensure the same predicted morphing characteristics. To evaluate this design space, each parameter will be independently investigated.

Table 8. Parameter Nominal, Maximum, and Minimum allowed value in the design space.

Param. Number	Parameter Name	Nominal Value	Max Value	Min Value	Units
1	# of Helicals	20	34	6	-
2	Radius	0.25	0.5	0.0625	(m)
3	Pitch	π	$3.25\ \pi$	$.25\ \pi$	(m)
4	Hel ID	0.01	0.05	0.001	(m)
5	Hel Thickness	0.01	0.05	0.001	(m)
6	Cyl ID	0.01	0.05	0.001	(m)
7	Cyl Thickness	0.01	0.05	0.001	(m)
8	Base Constraint	123	123456	123	DOF
9	Top Constraint	123	123456	123	DOF

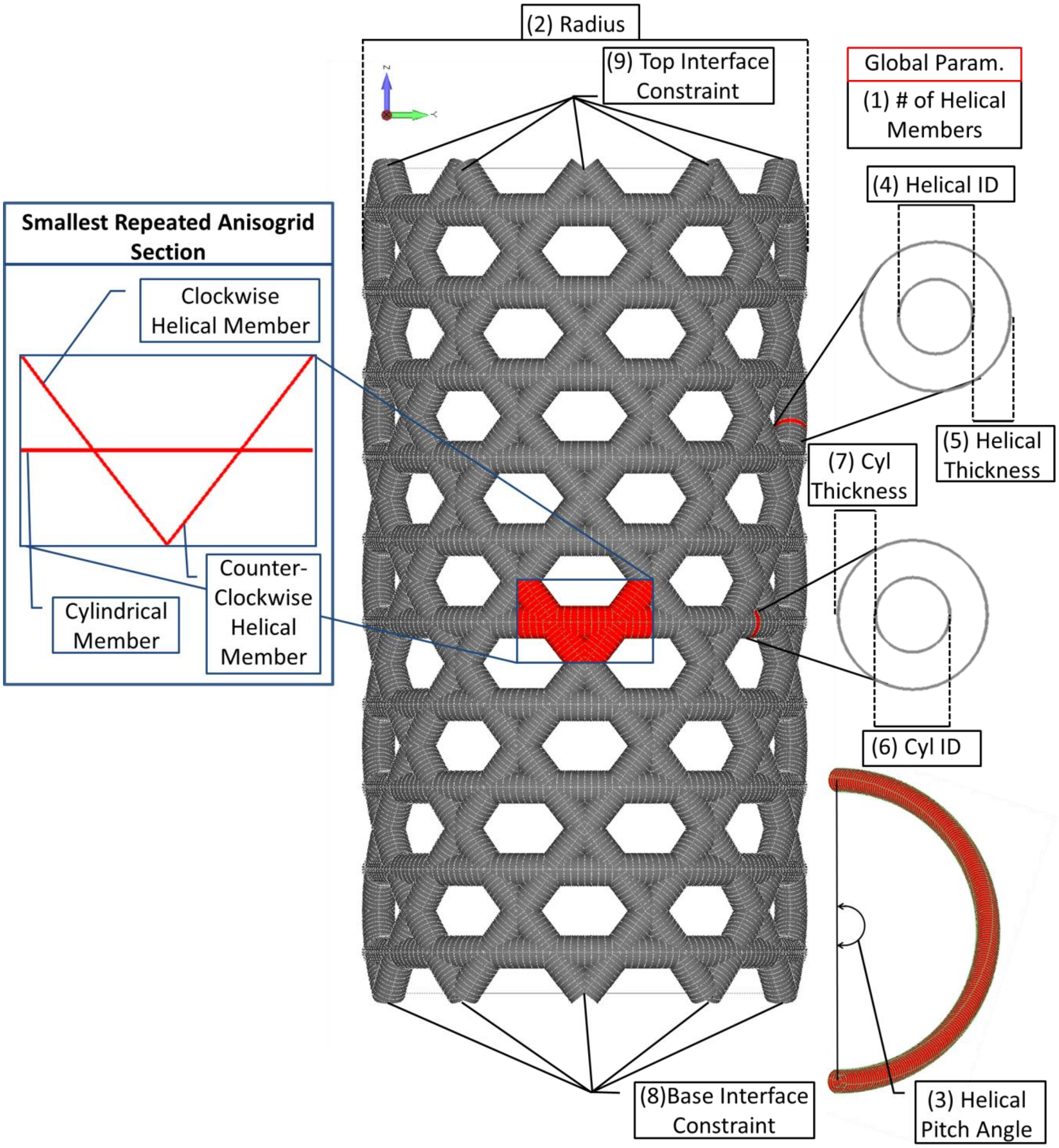

Figure 32. Anisogrid Geometry with all nine Geometric Parameters of Interest and the Smallest Repeated Anisogrid Section shown in Detail.

4. Parameterized Finite Element Model

A code was developed to utilize the nine geometric parameters listed in Table 8 as inputs and outputs of the corresponding FEM text. The Matlab parameterization code uses the geometric parameters as inputs, generates a text-based MSC Nastran input file, tells MSC Nastran to run the file, and then reads the text based results file back into Matlab for post-processing. The resulting output from the parameterized FEM model, as seen in Figure 33, is comprised of linear CBEAM elements, which make up the helical and circumferential members of the system. Two rigid RBE2 elements are used to model the two boundary conditions at the tip and base of the anisogrid boom. The 6 DOF fixed boundary condition, is located at the center base node, attached to each of the base interface nodes with all translational degrees of freedom fixed. The tip node displacement defines the morphing displacement and is connected to the tip interface nodes in all translational degrees of freedom. One of the parameters evaluated in this study is the rotational fixity between the tip and base nodes to their respective rigid elements.

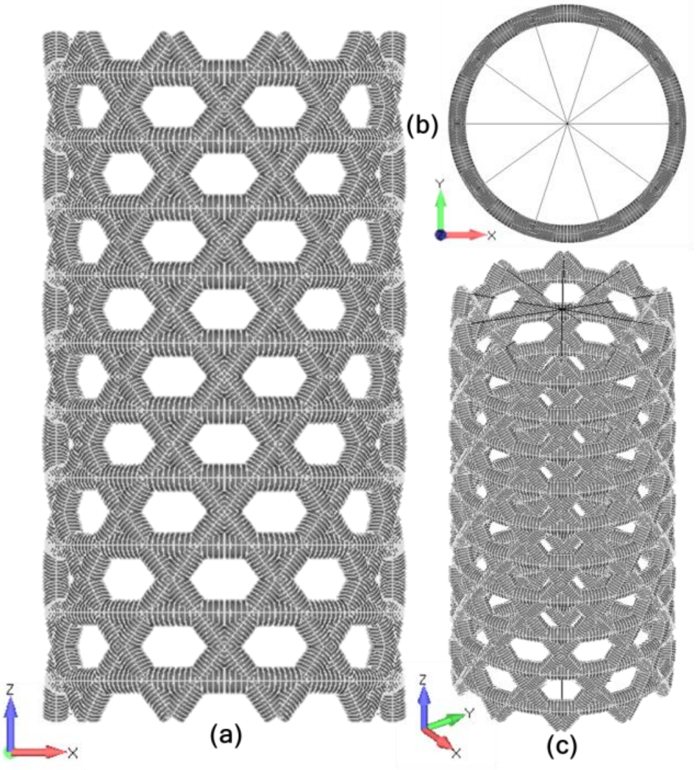

Figure 33. Finite Element Anisogrid for the 20 Helical Nominal Structure, (a) Side View, (b) Top View, (c) Isometric View.

In the development of the parameterized FEM code, the number of elements between each intersection point is defined as an adjustable variable in the FEM development code. While a convergence study was performed, the use of nine elements was more than the required to achieve convergence. The driving factor behind the choice for ten nodes per intersection was to simplify the discretization of the pitch angle. As the number of elements between each intersection increases, the variability or noise measured in the gradient of the cost function is reduced. The decision to use ten nodes between intersection points reduces future optimization complexity by increasing the number of stable pitch angles.

4.1 FEM Loading Environment and Assumptions

Several key assumptions have been made to simplify the model's complexity associated with the applied thermal load. Given that the operational conditions are in an on-orbit space environment where standard radiation shielding is used, both convective and radiative coupling between the active members is assumed to be zero. The second key modeling simplification is that conductive losses within the structure are assumed to be negligible. This assumption is a valid first approximation if specific care is placed to limit the thermal conduction in the design. Two methods to limit the coupling exist through the use of anisotropic conductive material properties or the design of low conduction structural interfaces. These assumptions simplify the computation by allowing for the thermal strain to be directly applied to the system rather than calculated from external thermal loading. Under these conditions, static linear modeling can capture the various morphing configurations with minimal computational resources using superposition. These assumptions can later be relaxed once the structural behavior has been fully understood.

To directly apply this thermal strain in the FEM, each helical member is independently loaded with $1℃\,\Delta T$ in conjunction with a Coefficient of Thermal Expansion (CTE) of 1 m/m/℃ resulting in a unit thermal strain $\varepsilon_{\Delta T}$ of 1 m/m. A single FEM output is therefore able to compute the true displacements of multiple material CTE values and thermal control capabilities by appropriately scaling the FEM results. Future work will include the incorporation of more realistic thermal loading environments to quantify the errors associated with these assumptions.

4.2 Superposition

Superposition is used to combine the individual helical loading cases into higher order loading cases and thus reduce the computational costs of developing multiple loading cases within the FEM code. These combined loading cases are used to evaluate the quality of the workspace and to find the minimum displacement capability resulting from a desired response. The linear modeling used does not require an evaluation of the accuracy of the superposition, one was performed for completeness, but is not detailed here. An example of the combination of two single helical loading cases (heated members shown in red) into a two-member loading case can be seen in Figure 34.

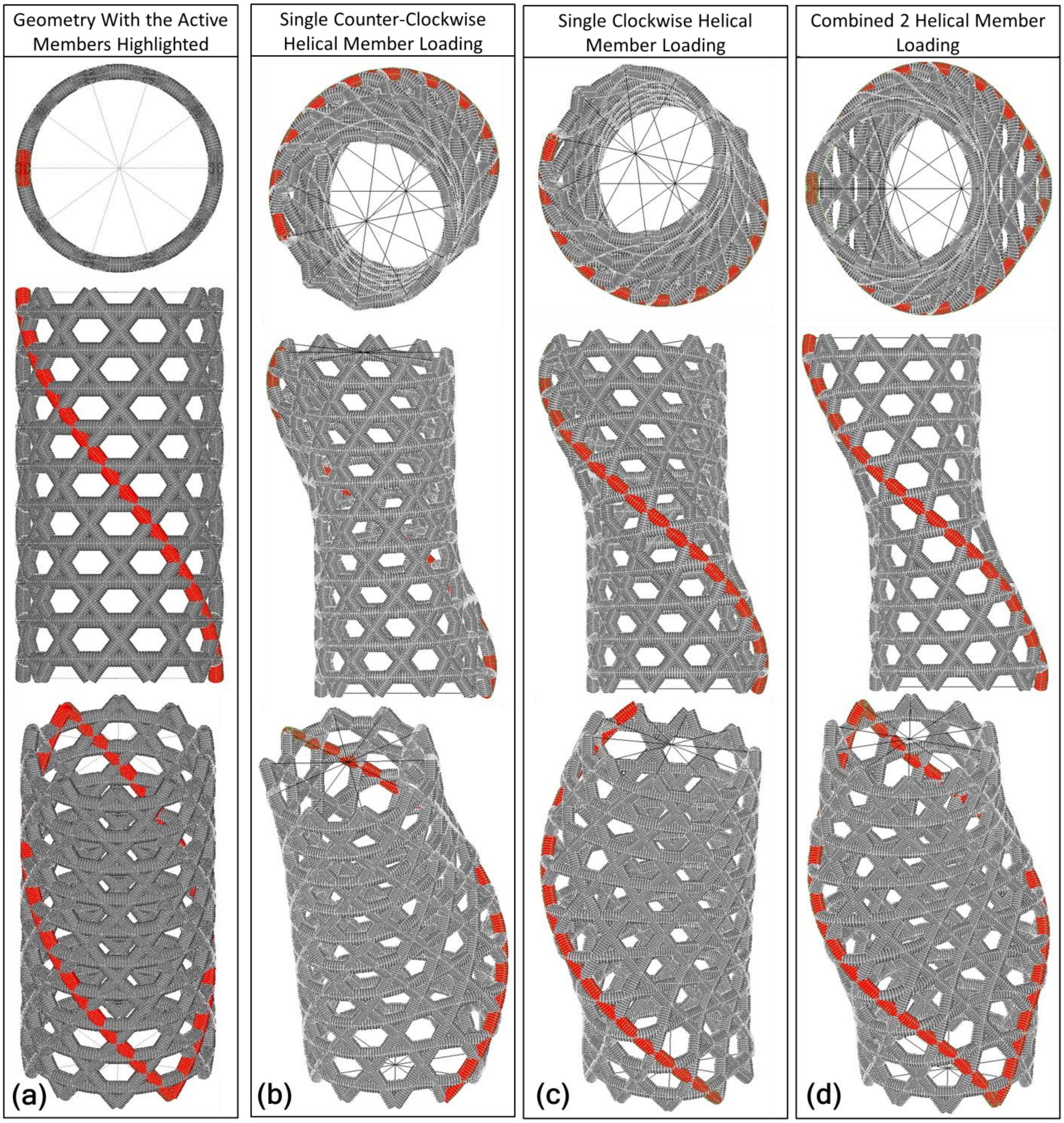

Figure 34. Finite Element Model Response to Three Loading Cases with the Heated Elements shown in Red. (a) Unloaded Geometry (b) Single Counter Clockwise Helical Loading, (c) Single Clockwise Helical Loading, (d) A Symmetric Combination of Clockwise and Counter Clockwise Helical Loading.

The clockwise and counter-clockwise helical loadings, as seen in Figure 34 (a) and (b), have symmetric displacement vectors. Two displacment vectors with compontents in all six DOF can be combined to generate a displacement in only the X and Z axis, as seen in Figure 34 (c). Multiple combinations of loadings will be evaluated in more depth in Section 5.2.

5. Nominal Geometry Investigation

The first step in the evaluation of this concept, is to explore the performance of the nominal geometry. The first phase of this investigation requires the assessment of the single helical morphing performance. The single helical morphing outputs can then be used to calculate the workspace and the minimum morphing capability.

5.1 Single Helical Loading Case

To evaluate the structure, each helical member is independently loaded with a thermal strain of ± 1m/m. To calculate all possible loading combinations, the linear FEM is only required to calculate $2n$ single helical morphing cases, where n is the number of helical members. This significantly reduces the overall computational costs, which enables iterative evaluation. Through the development of these base displacements, the full workspace can be constructed by combining and scaling these 40 inputs, as seen in Figure 35.

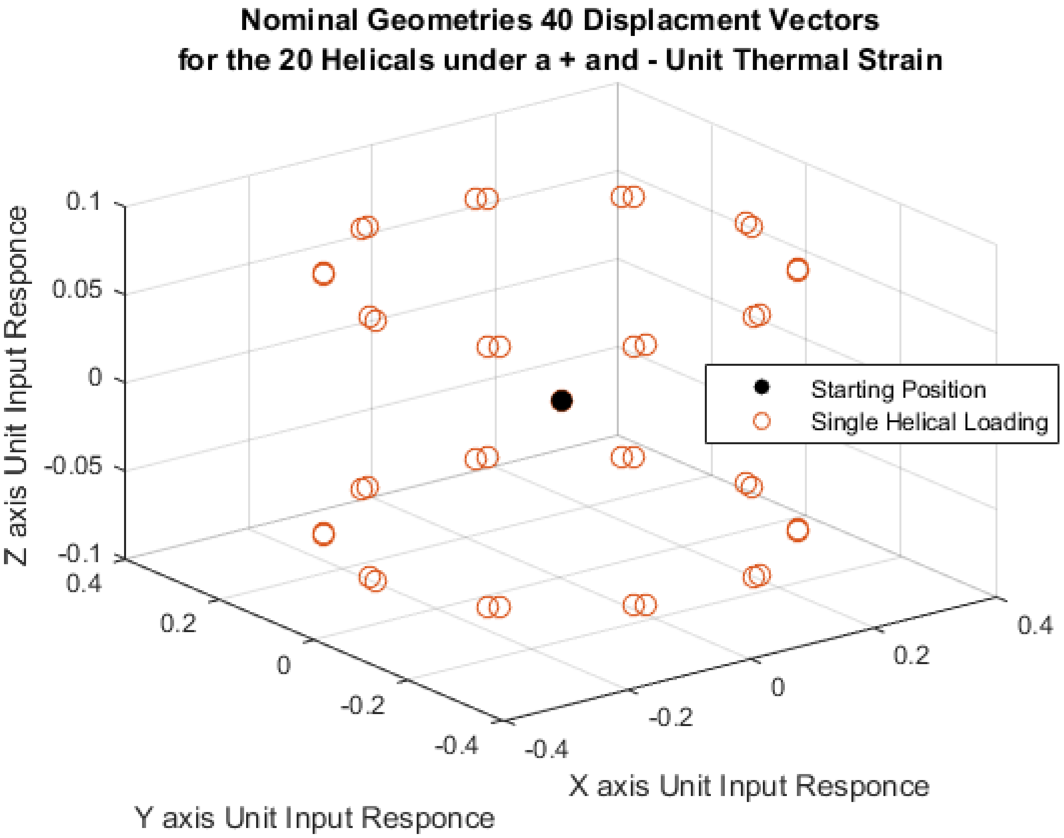

Figure 35. All 40 Positive and Negative Nominal Geometry Single Helical Morphing Displaced Positions Under a Unit thermal strain load.

5.2 Workspace Evaluation

The workspace size and properties can be computed from the single helical displacement cases to define the operational or reachable volume. For this complex anisogrid structure, which has 20 helical members, the number of possible loading combinations can be computationally prohibitive. To limit the computational cost of this investigation, the evaluation is restricted to only 4 combined helical loadings at a given time. Additionally, a globally applied temperature change loading case, which induces a uniform thermal strain, is included. The global thermal strain loading is combined with the single helical loading, as seen in Figure 36, to develop the overall inputs used to frame the workspace. A short study is performed to evaluate the impact that the scale of the applied thermal strain has on the shape and size of the workspace. The first workspace evaluation, as seen in Figure 37 (a), investigates the workspace under all possible permutations of 4 of the 20 helical members loaded with a thermal strain of [-2ε, -1ε, 0, 1ε, 2ε] m/m resulting in $2.6x10^6$ loading cases. The second evaluation, as seen in Figure 37 (b), expands the thermal loading to [-3ε, -2ε, -1ε, 0, 1ε, 2ε, 3ε] m/m resulting in $12x10^6$ loading cases. The third and final evaluation, as seen in Figure 37 (c), expands the thermal loading to [-4ε, -3ε, -2ε, -1ε, 0, 1ε, 2ε, 3ε, 4ε] m/m resulting in $36x10^6$ loading cases.

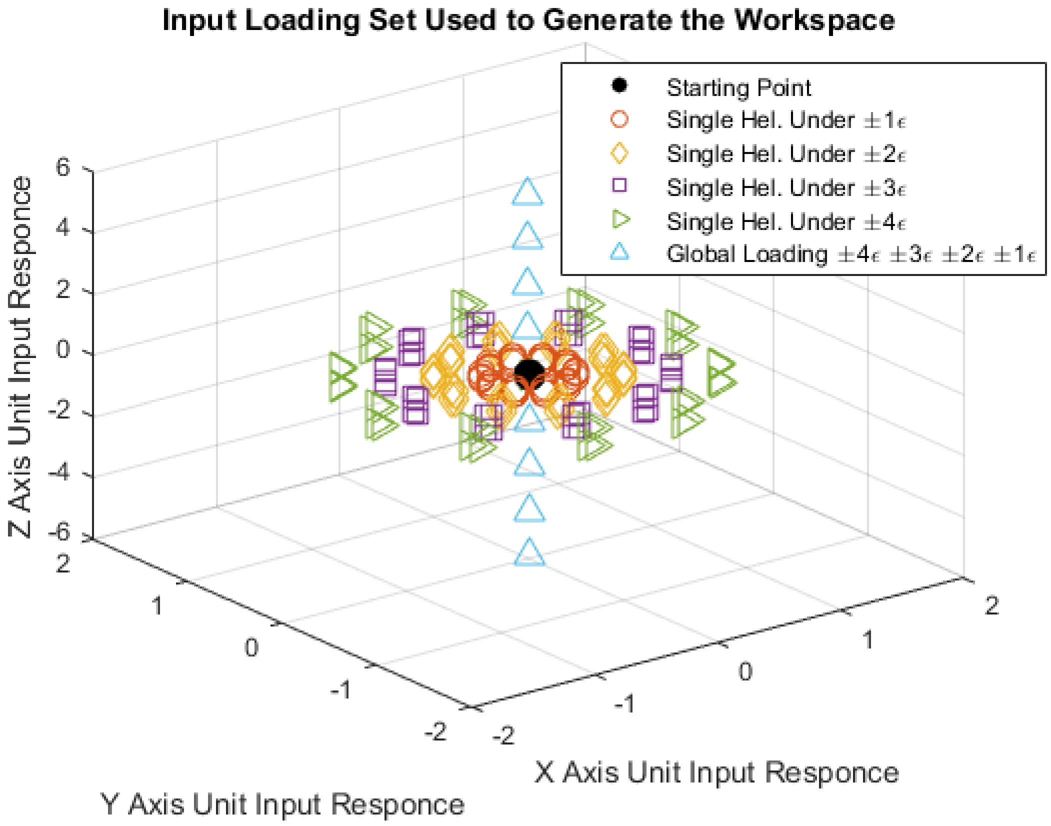

Figure 36. All Input Loading Cases for the Workspace and Minimum Morphing Evaluation Cases.

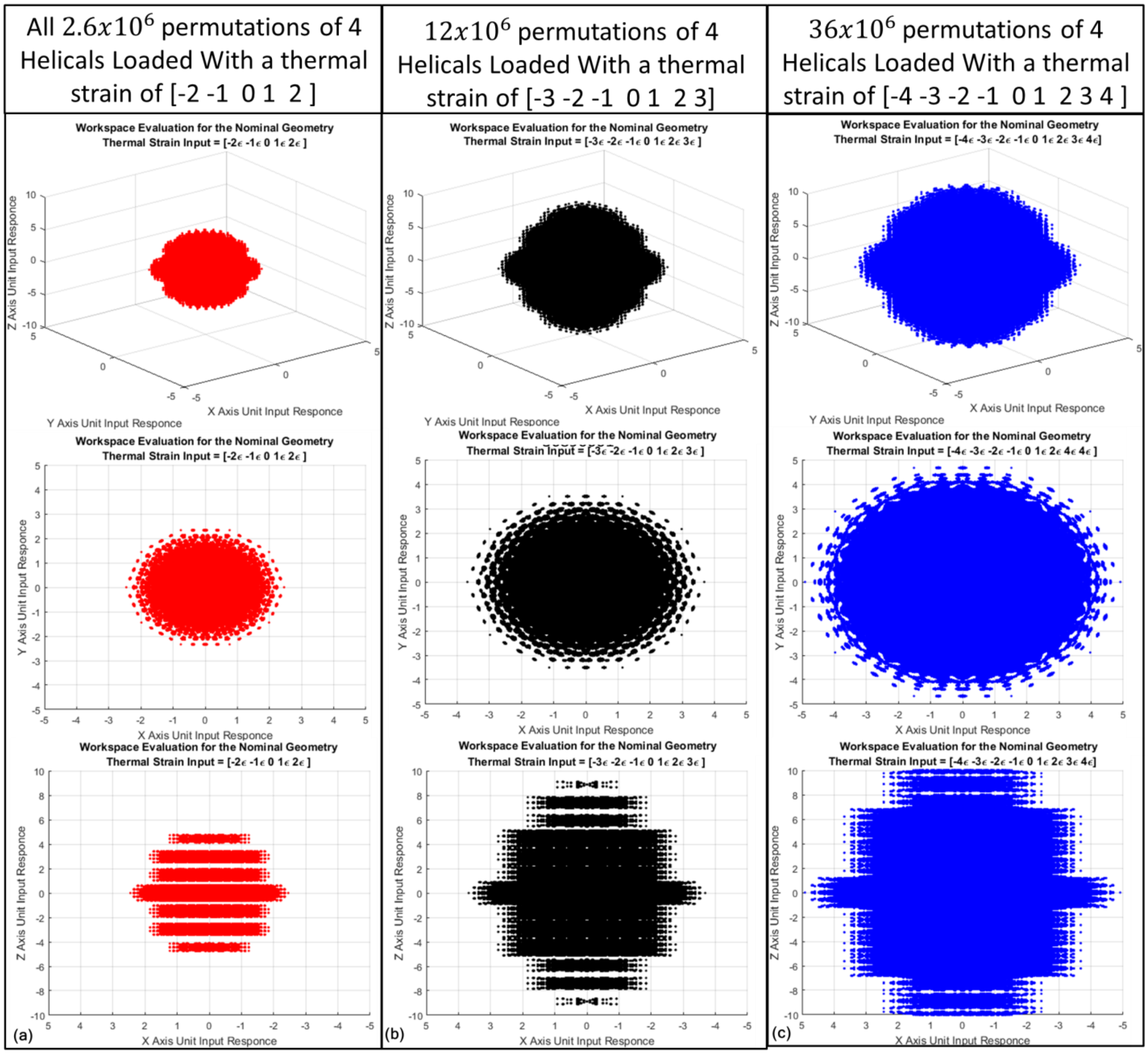

Figure 37. The Nominal Geometry Workspace with (a) An Applied Thermal Strain Sweep from -2 to 2 m/m, (b) An Applied Thermal Strain Sweep from -3 to 3 m/m, (c) An Applied Thermal Strain Sweep from -4 to 4 m/m.

As expected, the larger the applied thermal strain is on the system, the larger the resulting workspace. It can also be seen that gaps in the smaller strain sweep cases exist in the Z axis. For the larger loading cases, where more cases are evaluated, a sufficient loading set is provided to fill the gaps between the global thermal loading displacements. The workspace developing the full thermal strain sweep of [-4ε, -3ε, -2ε, -1ε, 0, 1ε, 2ε, 3ε, 4ε] m/m is used for future evaluation of the structure.

5.3 Minimum Morphing Capability

To quantify the minimum morphing capability in each of the six degrees of freedom, the $34x10^6$ morphing cases developed for the workspace evaluation using a thermal strain sweep of [-4ε, -3ε, -2ε, -1ε, 0, 1ε, 2ε, 3ε, 4ε] m/m is used. The workspace pointcloud is searched to find the single axis minimum morphing cases for all non-zero morphing positions, where the in axis term is an order of magnitude larger than all the off-axis terms. The minimum single axis displacement for each axis can be seen in Table 9.

Table 9. Minimum Displacement Vectors for all Six Degrees of Freedom Loaded using a Material Normalized Unit Strain of 1 m/m.

	Minimum Morphing Displacement Vector					
	Response to a Material Normalized Unit Strain of 1m/m					
	X	Y	Z	RX	RY	RZ
X Min Displacement Case	0.3014	0.0000	0.0000	0.0000	0.0000	0.0000
Y Min Displacement Case	0.0000	0.5733	0.0000	0.0000	0.0000	0.0000
Z Min Displacement Case	0.0000	0.0000	0.2958	0.0000	0.0000	0.0000
RX Min Displacement Case	0.0000	0.0093	0.0000	0.3728	0.0000	0.0000
RY Min Displacement Case	0.0176	0.0000	0.0000	0.0000	0.7091	0.0000
RZ Min Displacement Case	0.0000	0.0000	0.0000	0.0000	0.0000	1.5519

Depending on the application, the design space could change the search parameters to define the application specific minimum morphing capability. This investigation also calculates the helical members that, when loaded, produce the minimum displacement case. Figure 38 is an example of the minimum morphing control case in the X axis, where two helical members are loaded with a positive thermal strain (shown in red) and two members loaded with a negative thermal strain (shown in blue).

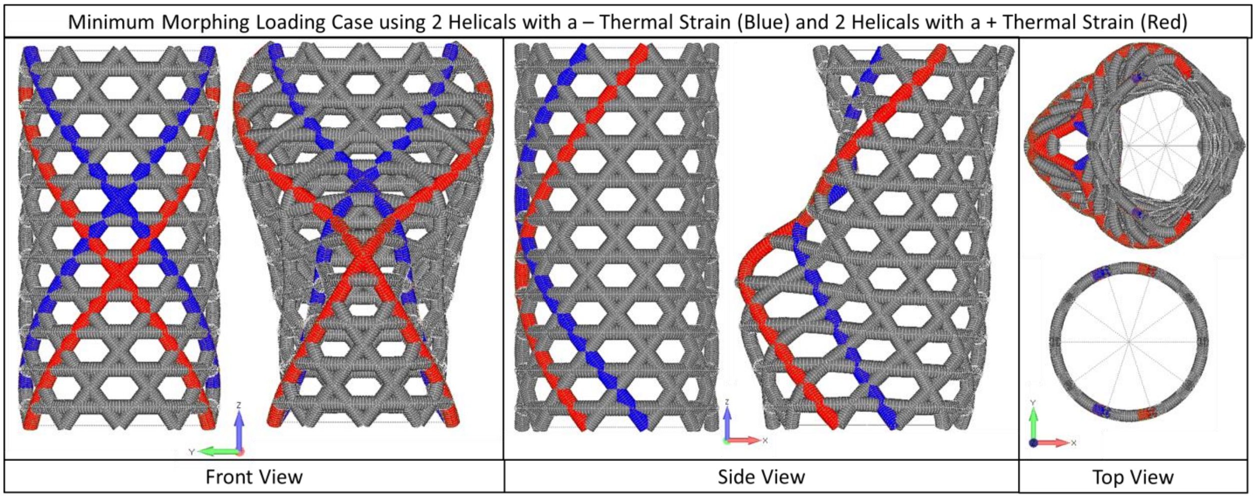

Figure 38. Visualization of the Loaded Helical Members and the Resulting X Axis Minimum In-Plane Displacement Capability for the Nominal Geometry.

5.4 Representative CTE and Thermal Control Evaluation

The use of a normalized unit input loading, allows scaling of the workspace and minimum displacement results to evaluate systems with a variety of material choices, displacement control goals, and thermal control requirements. The method to scale the original unit thermal strain and to calculate the properties of a specific material and thermal control capability is detailed in Equation 1 through Equation 3. The classically applied thermal strain calculation can be seen in Equation 1 as,

$$\varepsilon = \alpha \Delta T \, , \qquad [1]$$

where ε is the resulting thermal strain (m/m), α is the material CTE (m/m/°C), and ΔT is the thermal control capability (°C). For the development of the model α = 1 m/m/°C and $\Delta T = 1\ ^{\circ}C$ resulting in a thermal strain of 1m/m. To calculate the required thermal strain needed to achieve a specific displacement, the output of the FEM is scaled. Once the required thermal strain is known, the required material and thermal control capability can be calculated.

$$\frac{D_{FEM}}{\varepsilon_{input}} = \frac{D_{desired}}{\varepsilon_{required}} = \frac{D_{desired}}{\alpha \Delta T}\ , \tag{2}$$

where D_{FEM} (m) is the FEM output from a unit $\varepsilon_{input} = 1\ m/m$, the desired output is $D_{desired}$ (m) and the required material and control properties are α (m/m/°C)and ΔT(°C). For a given thermal control capability, the resulting equation can be rearranged to produce a relationship between the desired morphing control, and the required thermal control for a given material as,

$$\Delta T = \frac{D_{desired}\varepsilon_{input}}{D_{FEM}\alpha} \tag{3}$$

Using the FEM output detailed in Section 5.2, D_{FEM}, the other properties of the system can be evaluated. The first investigation is into the thermal control as a function of material CTE for a given displacement goal of 1 μm. The thermal control versus CTE evaluation in the six morphing DOF can be seen in Figure 39

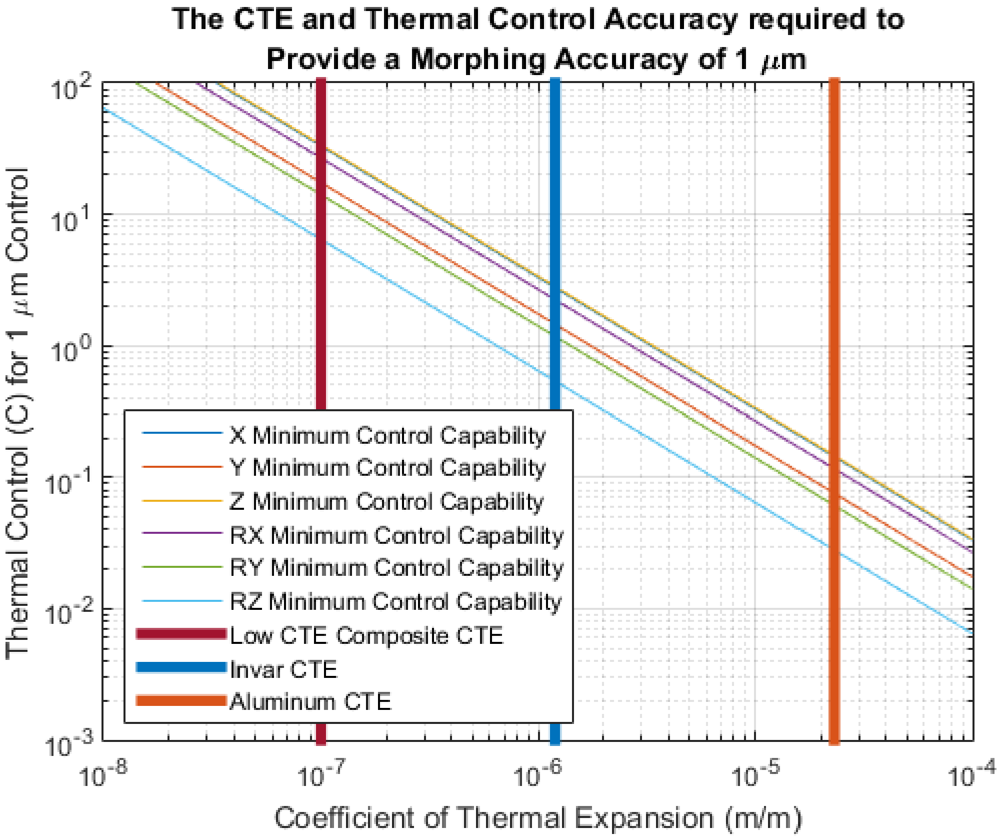

Figure 39. Evaluation of the Six DOF Thermal Control and Material CTE Required to Achieve 1 μm Displacement Control.

Low CTE carbon composite, invar, and aluminum are the three materials chosen to represent the overall CTE range. The three materials can achieve 1 μm displacement control in all six degrees of freedom, through the use of a thermal control system with an accuracy of, 20 °C, 2 °C, and .1 °C, respectively. To investigate the full geometric control for these three material properties, a study is performed relating thermal control capability versus displacement control capability. To define the maximum morphing capability, the maximum allowed ΔT is set to ten times the thermal control capability. The limiation of the maximum thermal load limits the total allowable system

ΔT to twenty times the thermal control capability. The minimum and maximum control capabilities for the three material properties for the X axis can be seen in Figure 40.

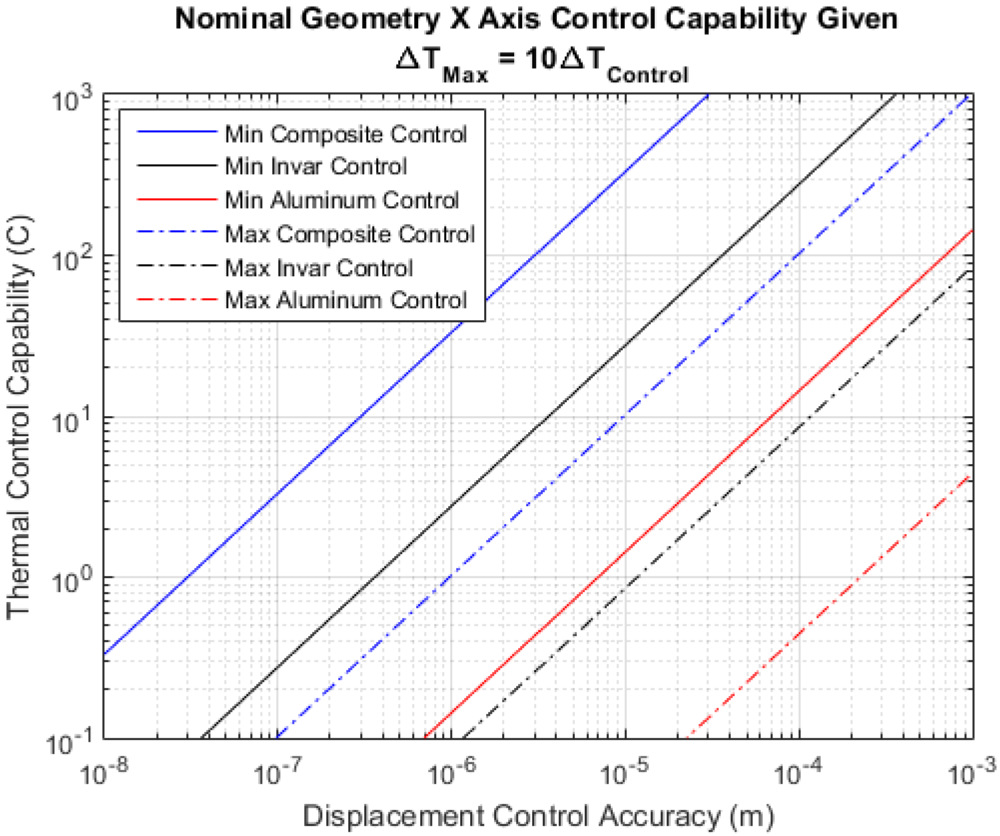

Figure 40. X Axis Displacement Control Accuracy vs. Thermal Control for the Minimum Control and Maximum Displacement for Each Material.

The distance between the minimum morphing line and the maximum morphing line in the X-axis represents the full morphing design space. The displacement control for the 1 °C control case for all 6 DOF can be seen in Table 10. This study provides the key pieces of information that can be used to evaluate the morphing capability of a system developed using one of the three chosen materials. The complex nature of the non-symmetric morphing capability will have to be addressed in the control system.

Table 10. Minimum and Maximum Displacement Control for all Three Materials of Interest and all 6 DOF given a thermal control capability of 1 °C.

	Displacement Control Capability given a Thermal Control of 1 C (meters)					
	Minimum Displacement Capability			Maximum Displacement Capability		
	Composite	Invar	Aluminum	Composite	Invar	Aluminum
X Disp.	3.01E-08	3.62E-07	6.96E-06	9.75E-07	1.17E-05	2.25E-04
Y Disp.	5.73E-08	6.88E-07	1.32E-05	9.28E-07	1.11E-05	2.14E-04
Z Disp.	2.96E-08	3.55E-07	6.83E-06	3.70E-06	4.44E-05	8.54E-04
RX Disp.	3.73E-08	4.47E-07	8.61E-06	1.21E-06	1.45E-05	2.79E-04
RY Disp.	7.09E-08	8.51E-07	1.64E-05	1.15E-06	1.38E-05	2.65E-04
RZ Disp.	1.55E-07	1.86E-06	3.58E-05	1.55E-06	1.86E-05	3.58E-04

Although the performance of the nominal geometries is now well understood, the design space is not. To better define the capability of this system, alternate geometries need to be investigated. The first investigation into this structure is performed by sweeping each of the nine parameters through the design space to determine each parameters effect on the morphing behavior.

6. Design Space Investigation

Further insight can be gained by evaluating the impact that each of the nine geometric parameters has on the overall system's performance. A cost function is developed to quantify the size of the displacement vector of the single helical morphing case so that a geometries morphing performance can be quickly evaluated. To investigate the resulting single helical loading morphing pattern as well as the geometries cost function, a parameter sweep is performed.

6.1 Cost Function Development

The helical system's minimum morphing loading input is given by a complex combination of helical loading combinations. To define the minimum control capability, an optimization would need to be performed on each geometry. Rather than implement this complex optimization, the geometry's minimum morphing capability will be quantified by evaluating the single helical displacement vector. Minimizing the cost function, as seen in Equation 4, will minimize the displacement vector length of single helical displacement vectors that are combined to generate geometry specific minimum morphing case.

$$Cost\ Function = \frac{D_x^2 + D_y^2 + D_z^2 + D_{rx}^2 + D_{ry}^2 + D_{rz}^2}{6}, \qquad [4]$$

where D is the six degree of freedom single helical loading displacement vector, measured at the master RBE2 node located at the tip of the anisogrid boom. This cost function can be calculated on any of the n singular helical displacements; this is because the overall length of each single helical displacement is constant for a given geometry, as seen in Figure 35.

6.2 Parameter Sweep

The impact that each geometric parameter has on the resulting single helical morphing position can be quantified through a parameter sweep. To perform the parameter sweep, each of the nine parameters of interest, as seen in Table 8, were swept through the full design space. The parameter sweep morphing position, calculated from the nine parameter sweeps, and their resulting cost functions are shown in Figure 41 through Figure 49.

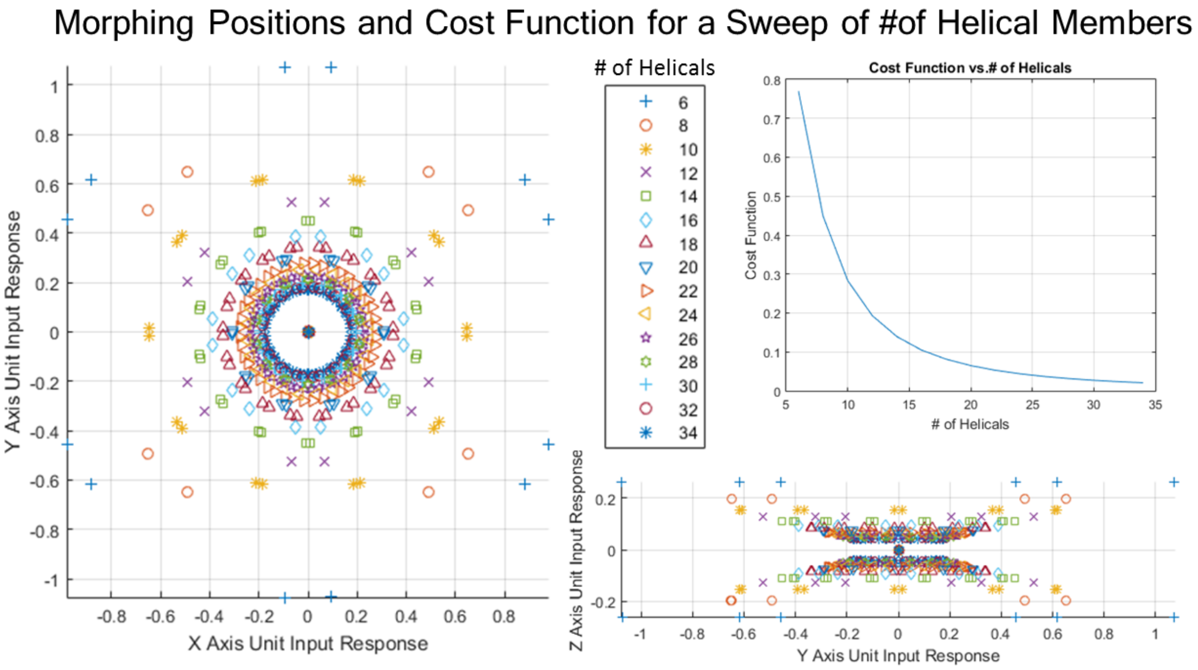

Figure 41. Number of Helical Member Parameter Sweep: Tip Displacement and Resulting Cost Function Under all n Helical Actuations with a unit thermal load applied using a 1 °C ΔT and a CTE of 1 m/m.

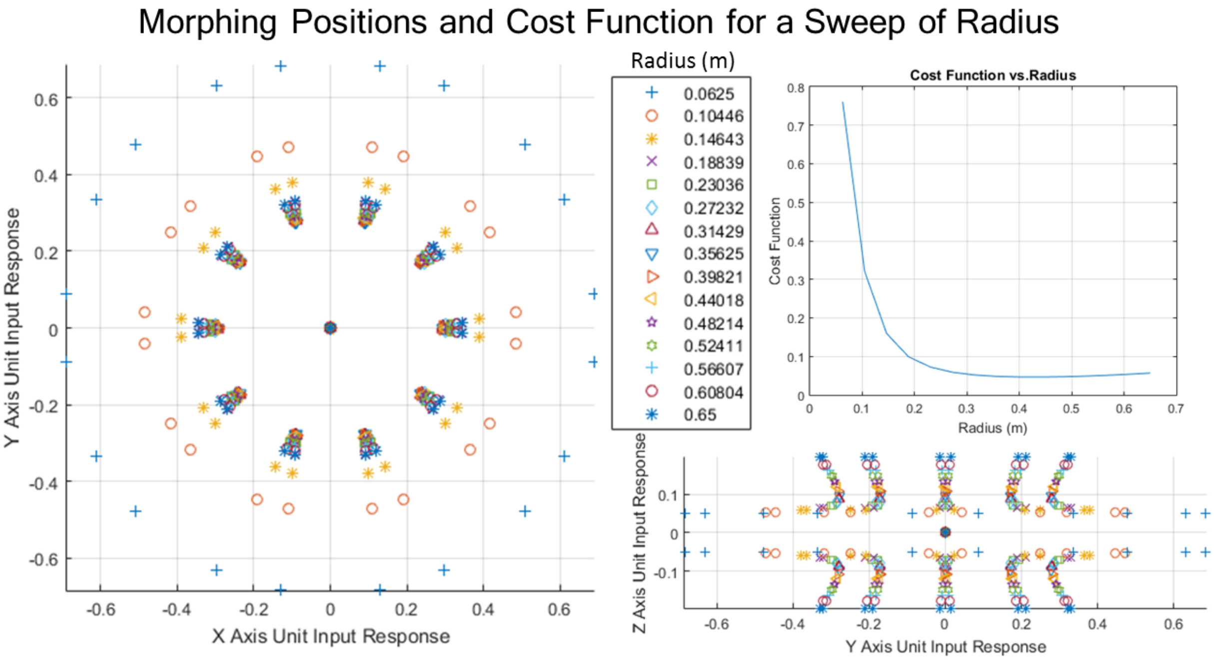

Figure 42. Radius Parameter Sweep: Tip Displacement and Resulting Cost Function Under all n Helical Actuations with a unit thermal load applied using a 1 °C ΔT and a CTE of 1 m/m.

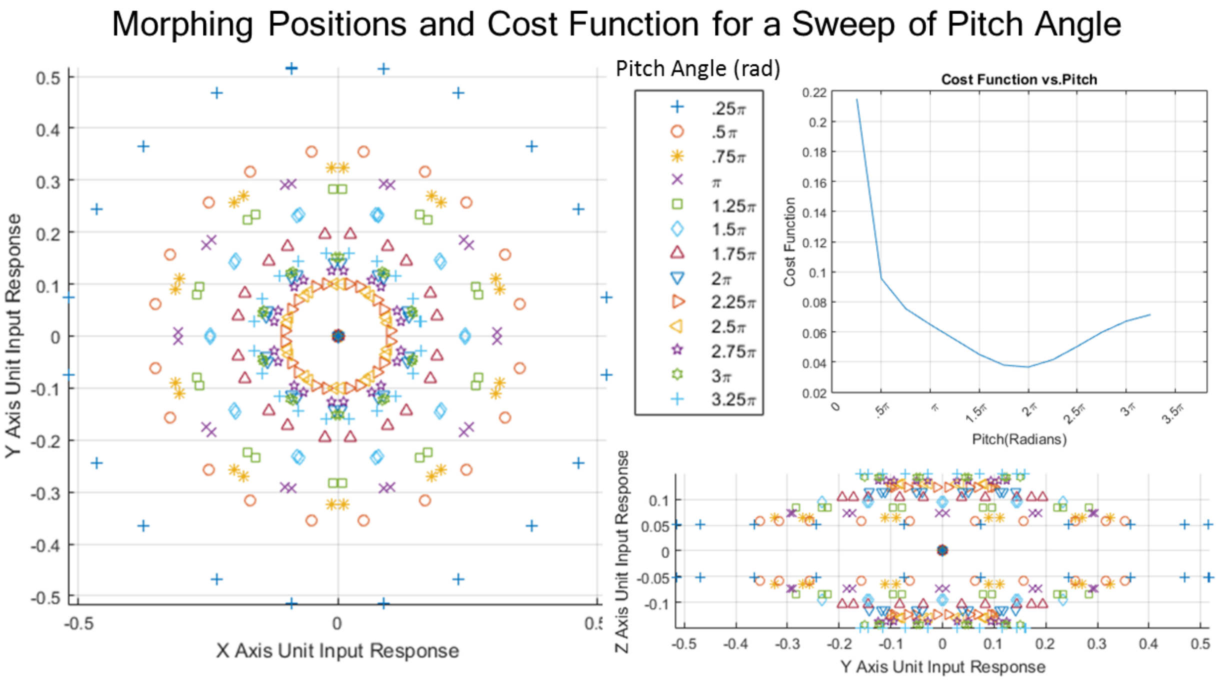

Figure 43. Helical Member Pitch angle Parameter Sweep: Tip Displacement and Resulting Cost Function Under all n Helical Actuations with a unit thermal load applied using a 1 °C ΔT and a CTE of 1 m/m.

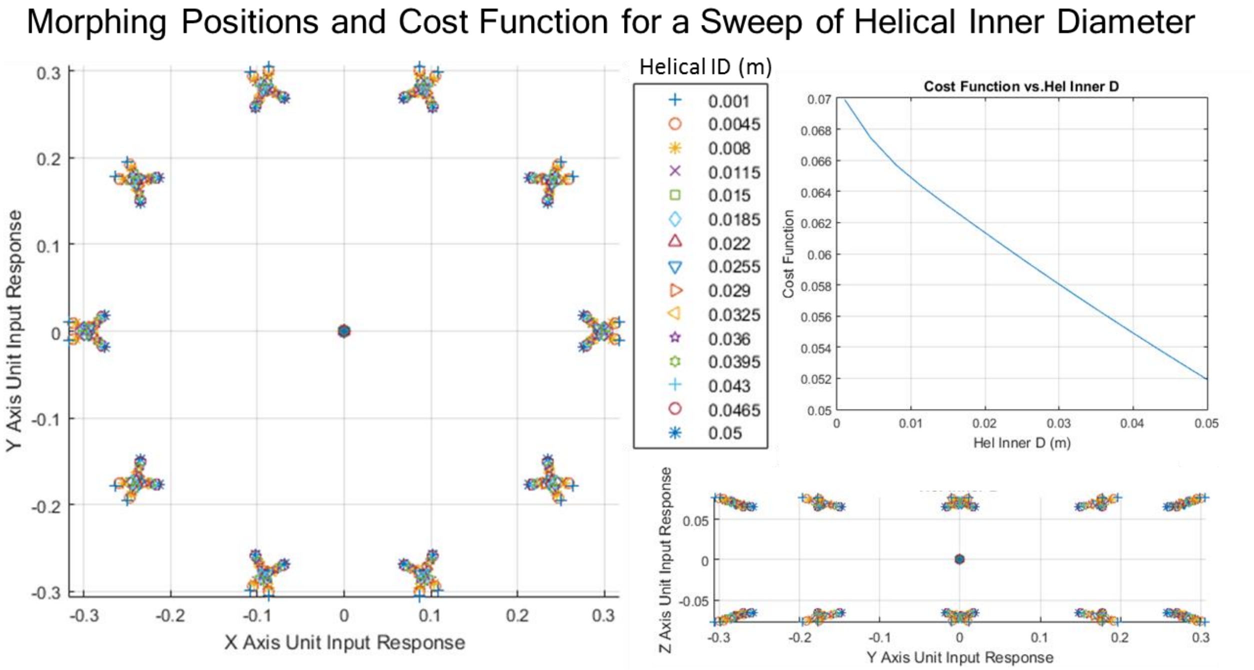

Figure 44. Helical Member Inner Diameter Parameter Sweep: Tip Displacement and Resulting Cost Function Under all n Helical Actuations with a unit thermal load applied using a 1 °C ΔT and a CTE of 1 m/m.

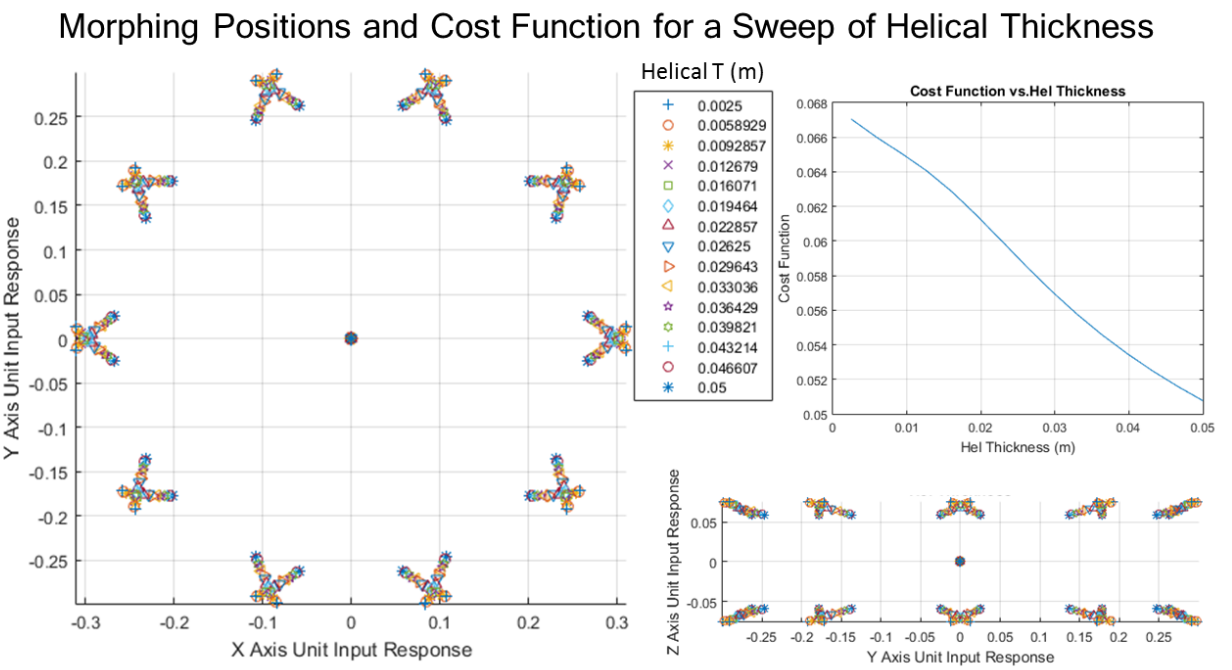

Figure 45. Helical Member Pitch angle Parameter Sweep: Tip Displacement and Resulting Cost Function Under all n Helical Actuations with a unit thermal load applied using a 1 °C ΔT and a CTE of 1 m/m.

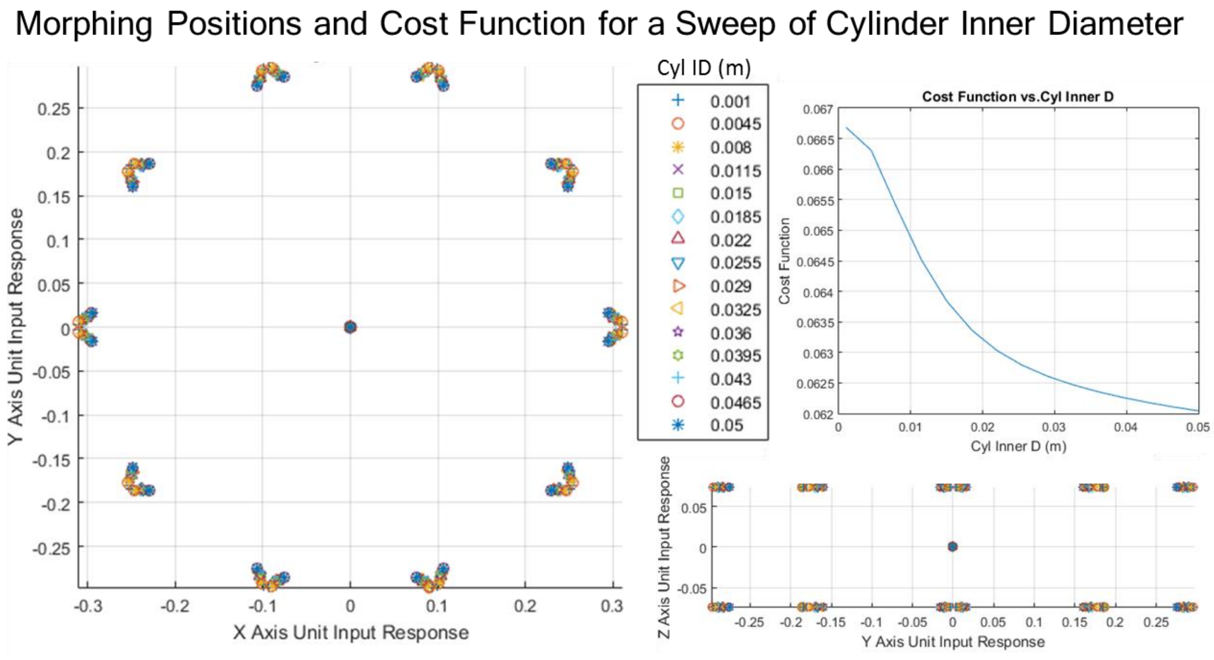

Figure 46. Cylindrical Member Inner Diameter Parameter Sweep: Tip Displacement and Resulting Cost Function Under all n Helical Actuations with a unit thermal load applied using a 1 °C ΔT and a CTE of 1 m/m.

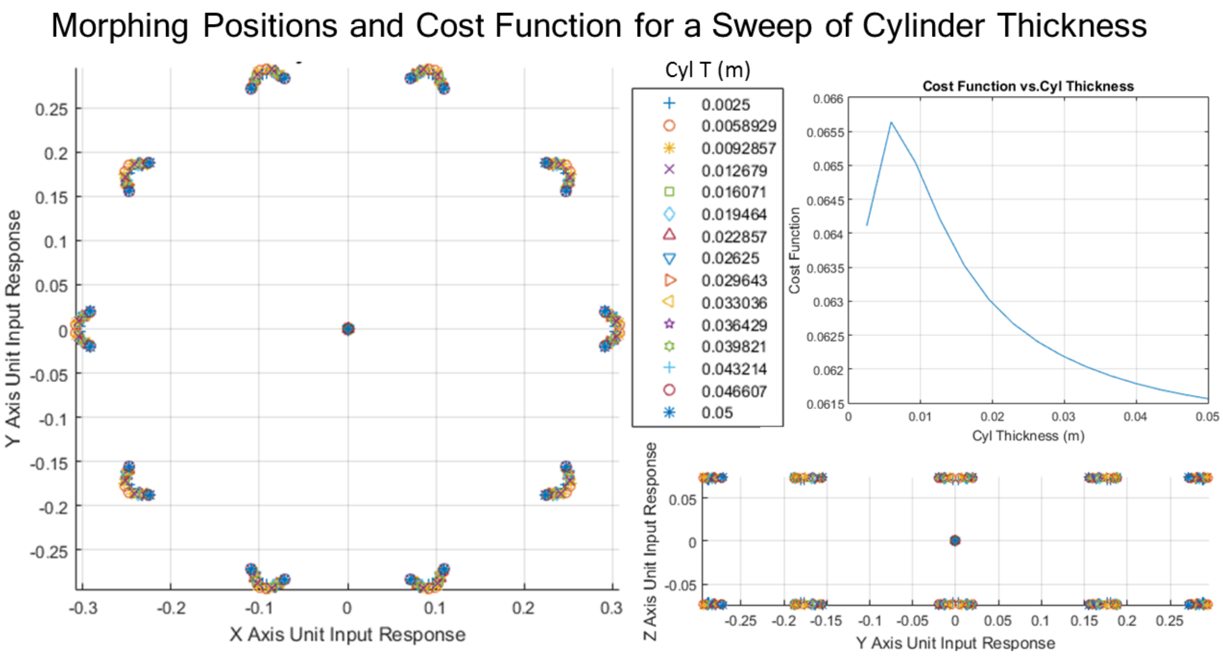

Figure 47. Cylindrical Member Thickness Parameter Sweep: Tip Displacement and Resulting Cost Function Under all n Helical Actuations with a unit thermal load applied using a 1 °C ΔT and a CTE of 1 m/m.

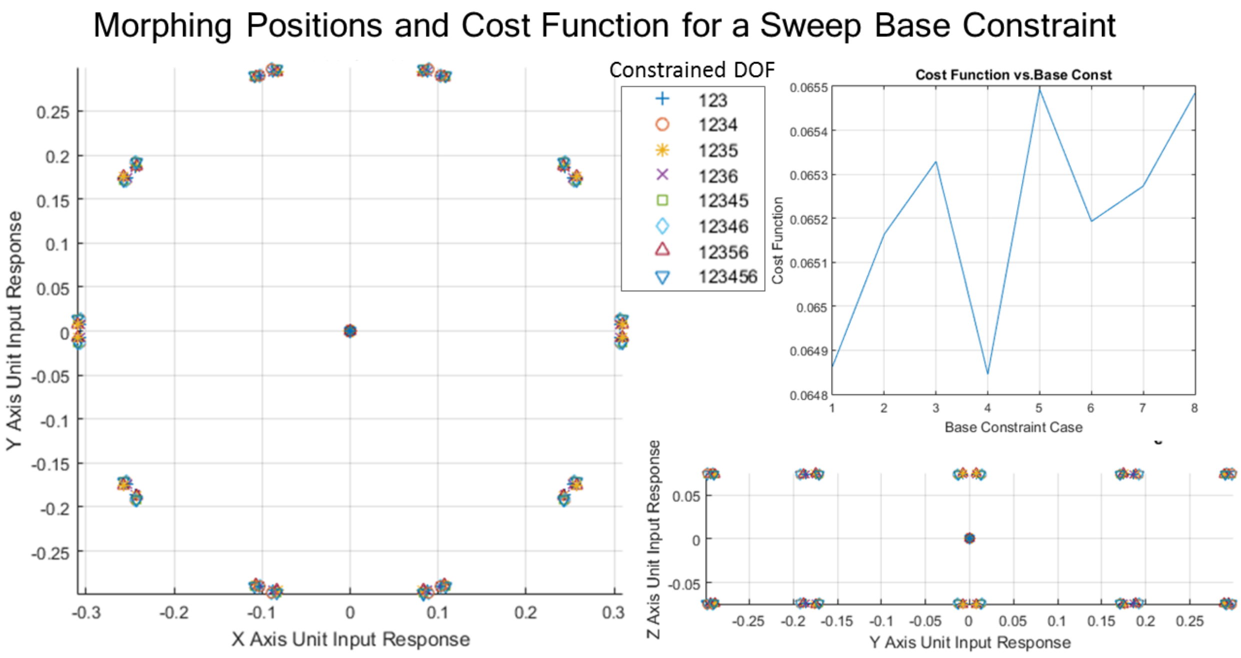

Figure 48. Base Boundary Condition Parameter Sweep: Tip Displacement and Resulting Cost Function Under all n Helical Actuations with a unit thermal load applied using a 1 °C ΔT and a CTE of 1 m/m.

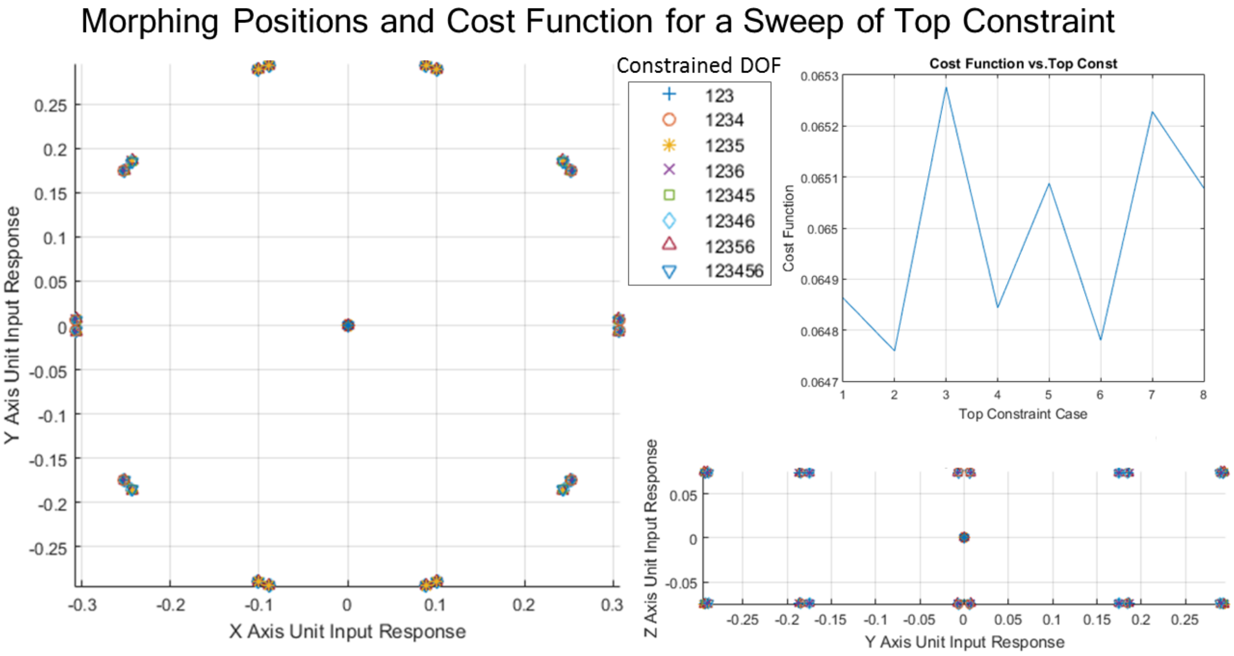

Figure 49. Tip Boundary Condition Parameter Sweep: Tip Displacement and Resulting Cost Function Under all n Helical Actuations with a unit thermal load applied using a 1 C° ΔT and a CTE of 1 m/m.

The nine parameter sweeps demonstrate the various parameter's impact on the overall morphing of the system. While each of these parameters has an effect on global stiffness, the effect of the parameter on the overall input loading can be discussed with increased depth. An increase in the number of helical members is expected to increase the system stiffness, through, not only the greater number of helical members, but also through an increase in the number of cylindrical members required to maintain anisogrid hexagonal pattern. These factors result in an exponential growth in overall stiffness. This impact can be seen in an exponential reduction in the cost function as the number of helical members increase, as demonstrated in Figure 41. The pitch angle affects multiple components in the morphing evaluation. Firstly, the pitch angle has a coupled stiffness effect between the axial, circumferential, and bending stiffness. Secondly, the pitch angle dictates the angle of the thermal strain vector. Finally, the pitch angle affects the length of the helical member resulting in control over the overall thermal strain applied to the system. The complex coupling between the pitch angle and the cost function, as seen in Figure 43, is due to the complex coupling of these multiple factors. As the radius increases, the total bending stiffness increases; but, an important secondary effect is the change in the effective thermal strain direction by changing the circumferential travel distance of the helical. These complex dynamics can be seen in Figure 42. The impact of the helical cross-section inputs, seen in Figure 44 and Figure 45, as well as the cylindrical cross section, as seen in Figure 46 and Figure 47, have local and global effects. The overall helical and cylindrical stiffness has an impact on the total stiffness and the axial stiffness of the helical member. This dictates the effective actuation force provided by the applied thermal strain and the effective global stiffness acting against that actuation force. Due to the nature of the top and base fixity parameters, as seen in Figure 48 and Figure 49, no distinct pattern appears in the cost function parameters sweep. Identifying the parameters' effect on the cost function, as well as the nature of the structural coupling, provides insight into the importance of each of these parameters. Once a basic understanding of the parameters' impact on the system is obtained, an investigation into the full design space of the system can begin.

7. Heuristic Optimization / Design Space Evaluation

A full optimization would have to be performed on all nine parameters to develop the true optimal geometry that maximizes the structures performance capability. Further complicating the optimization task, the design space contains three non-continuous parameters: the number of helical members, top constraint, and bottom constraint. Therefore, a more basic method will be employed to evaluate the scale of the design space, and the full optimization is left for future work. This simplified heuristic optimization is not a fully coupled optimization, but rather an uncoupled parameter optimization where each of the nine parameters are optimized independently. To generate this heuristic optimization, the minimum and maximum cost function in each parameter sweep is recorded. To then generate the global minimum cost function system, each of the nine minimum values from the nine parameter sweeps are used to generate the minimum cost function geometry. This is repeated for the maximum cost function in the nine parameter sweep to generate the maximum cost function geometry. These two cases are then evaluated to generate the heurstic optimized cost function cases.

Table 11. Evaluation of Each Parameter Maximum and Minimum Cost Function in the Parameter Sweep and the Resulting Total Change in the Cost Function. Highlighted Entries Exist at the Borders of the Design Space.

	Minimum C-F In Design Space		Maximum C-F In Design Space			
	Param Value	Cost Function	Param Value	Cost Function	Units	Cost Function Δ
# of Helical Members	34	0.02078	6	0.7699	-	0.74912
Radius	0.4402	0.04648	0.0625	0.7612	(m)	0.71472
Pitch Angle	1.898π	0.03634	0.25π	0.215	(m)	0.17866
Hel Inner D	0.05	0.05192	0.001	0.06991	(m)	0.01799
Hel Thickness	0.05	0.05076	0.001	0.06705	(m)	0.01629
Cyl Inner D	0.05	0.06204	0.001	0.06668	(m)	0.00464
Cyl Thickness	0.05	0.06156	0.005893	0.06564	(m)	0.00408
Base Constraint	1236	0.06485	12345	0.06549	DOF	0.00064
Top Constraint	1234	0.06476	1235	0.06528	DOF	0.00052
Nominal Geometry	-	0.0649	-	-	-	-
Heuristic Optimization	-	0.007697	-	513.083	-	513.07528

The minimum morphing case, which uses the nine minimum cost functions, found in the nine parameter sweeps, was calculated to have a cost function value of 0.007697. The maximum morphing case that uses the maximum cost functions found in the nine parameter sweeps was calculated to have a cost function of 513.083. These cost functions do not demonstrate the true potential of the system, but rather provide an indication of the performance range in the design space. It can be seen that a five order of magnitude overall displacement length difference can be seen within the design space. This is indicative that this geometry can solve a wide variety of morphing problems. Future efforts will address the full geometric optimization and further investigate the design space.

Conclusions

This paper has shown that the thermal morphing anisogrid high precision morphing concept has significant promise for high precision thermal control in the space environment. This method for modeling and evaluation is shown to be feasible and have a low computational cost. Assuming linearity and directly applying thermal strains allows for computationally efficient evaluation of the structure; however, further expansion of the model is needed to include more complex thermal loads and will improve the performance of model predictions. The parameterized FEM development code, used in this initial study, has been validated through these initial efforts and can provide further study into the structure's performance.

The thermal morphing anisogrid structure has been demonstrated to be a potential replacement for the current structural highly precise paradigm. For this structure to demonstrate sufficient improvement on current capability, the true limits of the system need to be identified. A robust optimization is required in the future to evaluate the coupling of the input parameters. Current evaluation of the nominal geometry, which uses low CTE composite was shown to have a minimum morphing capability of 30 nm in the X-axis given a thermal control capability of 1 °C.

The maximum displacement capability for the same system could deliver a maximum X displacement of 1 μm. While further investigation is required, the current thermal morphing anisogrid structure has shown great potential to deliver significantly improved performance relative to the existing capability.

Through the parameter sweep, a deeper understanding of the current structure and the potential of the concept has been developed. The parameter sweep also provides a rough estimate on the overall importance of each of the parameters. By looking at the cost function range, it can be seen that the number of helical members, the radius, and the pitch angle has a more significant effect on the systems performance. For future optimization efforts, these parameters should be a focus.

A cost function was developed to quantify all nine parameters impact on the morphing capability of the structure. The cost function associated with the nominal geometry was shown to be 0.065. Through the simplified Heuristic optimization, it was shown that the minimum cost function in the design space was found to be 0.007697. The maximum cost function was found to be 513.083. This represents structures with five orders of magnitude variation in the overall displacement vector. This demonstrates the morphing range that the anisogrid thermal morphing system can address. The potential for improvement over the nominal geometry has been demonstrated and a full optimization to define the minimum morphing capability is the next step in the evaluation of this concept. The work in this paper has laid a solid foundation for further investigations into this concept. Future work to address the complex optimization problem will improve the understanding of the limits of this concept. The ability for the concept to achieve nano, micro, and macro displacements through further optimization should be investigated. A limiting factor that needs to be addressed is the frequency response capability as a function of the available power. The frequency response study will identify the possible range of vibration isolation and provide limits to the concept's applications. Overall, these efforts will provide a complete view of the thermal morphing anisogrid structures capability to address the structural needs of future space systems.

Acknowledgements

The authors would like to acknowledge the support by the Naval Research Laboratory through the Select Graduate Training Program.

References

1. Wada, B.K., *Adaptive structures-An overview.* Journal of spacecraft and rockets, 1990. 27(3): p. 330-337.
2. Thayer, D., et al., *Six-axis vibration isolation system using soft actuators and multiple sensors.* Journal of spacecraft and rockets, 2002. 39(2): p. 206-212.
3. Thill, C., et al., *Morphing skins.* The Aeronautical Journal, 2008. 112(1129): p. 117-139.
4. Kuder, I.K., et al., *Variable stiffness material and structural concepts for morphing applications.* Progress in Aerospace Sciences, 2013. 63: p. 33-55.
5. Li, W. and H. Huang, *Integrated optimization of actuator placement and vibration control for piezoelectric adaptive trusses.* Journal of Sound and Vibration, 2013. 332(1): p. 17-32.
6. Tarazaga, P.A., D.J. Inman, and W.K. Wilkie, *Control of a space rigidizable inflatable boom using macro-fiber composite actuators.* Journal of Vibration and Control, 2007. 13(7): p. 935-950.
7. Ruggiero, E.J. and D.J. Inman, *Gossamer spacecraft: recent trends in design, analysis, experimentation, and control.* Journal of Spacecraft and Rockets, 2006. 43(1): p. 10-24.
8. Ramrakhyani, D.S., et al., *Aircraft structural morphing using tendon-actuated compliant cellular trusses.* Journal of aircraft, 2005. 42(6): p. 1614-1620.
9. Korkmaz, S., *A review of active structural control: challenges for engineering informatics.* Computers & Structures, 2011. 89(23): p. 2113-2132.
10. Hiroaki, T., et al., *Development of a smart reconfigurable reflector prototype for an extremely high-frequency antenna.* Journal of Intelligent Material Systems and Structures, 2015: p. 1045389X15580660.
11. Chopra, I., *Review of state of art of smart structures and integrated systems.* AIAA journal, 2002. 40(11): p. 2145-2187.
12. Li, D.-X. and R. Xu, *Optimal Design and Control of Smart Space Structures: A Memetic Evolution Approach.* Intelligent Systems, IEEE, 2014. 29(1): p. 40-46.
13. Garba, J.A., B.K. Wada, and J.L. Fanson, *Adaptive structures for precision controlled large space systems.* Journal of intelligent material systems and structures, 1992. 3(2): p. 348-366.

14. Tarazaga, P.A., et al. *Structural health monitoring of an inflatable boom subjected to simulated micrometeoroid/orbital debris damage*. in *Nondestructive Evaulation for Health Monitoring and Diagnostics*. 2006. International Society for Optics and Photonics.
15. Tarazaga, P.A., M.E. Johnson, and D.J. Inman, *Vibro-acoustics of a pressurized optical membrane.* Mechanical Systems and Signal Processing, 2012. 30: p. 373-392.
16. Tarazaga, P.A., D.J. Inman, and W.K. Wilkie, *Control of a space rigidizable-inflatable boom using embedded piezoelectric composite actuators.* AIAA Paper, 2006(2006-1976).
17. Tarazaga, P.A., M.E. Johnson, and D.J. Inman, *Experimental validation of the vibro-acoustic model of a pressurized membrane.* Mechanical Systems and Signal Processing, 2014. 45(2): p. 330-345.
18. Stewart, D., *A platform with six degrees of freedom.* Proceedings of the institution of mechanical engineers, 1965. 180(1): p. 371-386.
19. Yang, J., et al., *Design of a Vibration Isolation System for the Space Telescope.* Journal of Guidance, Control, and Dynamics, 2015: p. 1-8.
20. Wedeking, G.A., J.J. Zierer, and J.R. Jackson. *Kinematic optimization of upgrade to the Hobby-Eberly Telescope through novel use of commercially available three-dimensional CAD package*. in *SPIE Astronomical Telescopes+ Instrumentation*. 2010. International Society for Optics and Photonics.
21. Zierer, J.J., et al. *The development of high-precision hexapod actuators for the Hobby-Eberly Telescope Wide Field Upgrade*. in *SPIE Astronomical Telescopes+ Instrumentation*. 2010. International Society for Optics and Photonics.
22. Zierer, J.J., et al. *Design, testing, and installation of a high-precision hexapod for the Hobby-Eberly Telescope dark energy experiment (HETDEX)*. in *SPIE Astronomical Telescopes+ Instrumentation*. 2012. International Society for Optics and Photonics.
23. Austin A. Phoenix, S.G., Pablo A. Tarazaga, *Dynamic Model Reduction Using Data-Based Loewner-SVD Methods applied to Thermally Morphing Structures.* Journal of sound and vibration, 2016.
24. Zhu, Y., A. Corigliano, and H.D. Espinosa, *A thermal actuator for nanoscale in situ microscopy testing: design and characterization.* Journal of Micromechanics and Microengineering, 2006. 16(2): p. 242.
25. Bühler, J., et al., *Thermally actuated CMOS micromirrors.* Sensors and Actuators A: Physical, 1995. 47(1): p. 572-575.
26. Schweizer, S., et al., *Thermally actuated optical microscanner with large angle and low consumption.* Sensors and Actuators A: Physical, 1999. 76(1): p. 470-477.
27. Rahafrooz, A., et al. *Thermal actuation, a suitable mechanism for high frequency electromechanical resonators*. in *Micro Electro Mechanical Systems (MEMS), 2010 IEEE 23rd International Conference on*. 2010. IEEE.
28. Kim, D.H., Y.C. Park, and S. Park, *Design and fabrication of twisting-type thermal actuation mechanism for micromirrors.* Sensors and Actuators A: Physical, 2010. 159(1): p. 79-87.
29. Moulton, T. and G. Ananthasuresh, *Micromechanical devices with embedded electro-thermal-compliant actuation.* Sensors and Actuators A: Physical, 2001. 90(1): p. 38-48.
30. Schmid, P., F. Hernandez-Guillen, and E. Kohn, *Diamond switch using new thermal actuation principle.* Diamond and related materials, 2003. 12(3): p. 418-421.
31. Singh, J., et al., *3D free space thermally actuated micromirror device.* Sensors and Actuators A: Physical, 2005. 123: p. 468-475.
32. Toropova, M.M., *THERMAL ACTUATION THROUGH BIMATERIAL LATTICES*, in *SMASIS*. 2015.
33. Toropova, M.M. and C.A. Steeves, *Adaptive bimaterial lattices to mitigate thermal expansion mismatch stresses in satellite structures.* Acta Astronautica, 2015. 113: p. 132-141.
34. Toropova, M. and C. Steeves, *Bimaterial lattices with anisotropic thermal expansion.* Journal of Mechanics of Materials and Structures, 2014. 9(2): p. 227-244.
35. Eckstein, E., A. Pirrera, and P.M. Weaver, *Thermally Driven Morphing with Hybrid Laminates and Metal Matrix Composites.* Mechanics, 2015. 2: p. 11.
36. Pirrera, A., D. Avitabile, and P. Weaver, *On the thermally induced bistability of composite cylindrical shells for morphing structures.* International Journal of Solids and Structures, 2012. 49(5): p. 685-700.
37. Eckstein, E., et al., *THERMALLY-DRIVEN SNAP-THROUGH AND MULTISTABILITY USING LAMINATED FIBRE-METAL SHELLS.*
38. Sorrentino, L., et al., *Design and Manufacturing of an Isogrid Structure in Composite Material: Numerical and Experimental Results.* Composite Structures, 2016.
39. Totaro, G. and F. De Nicola, *Recent advance on design and manufacturing of composite anisogrid structures for space launchers.* Acta Astronautica, 2012. 81(2): p. 570-577.

40. Totaro, G., *Local buckling modelling of isogrid and anisogrid lattice cylindrical shells with triangular cells.* Composite structures, 2012. 94(2): p. 446-452.
41. Zhang, Y., et al., *Deformation and failure mechanisms of lattice cylindrical shells under axial loading.* International Journal of Mechanical Sciences, 2009. 51(3): p. 213-221.
42. Vasiliev, V. and A. Razin, *Anisogrid composite lattice structures for spacecraft and aircraft applications.* Composite Structures, 2006. 76(1): p. 182-189.
43. Morozov, E., A. Lopatin, and V. Nesterov, *Finite-element modelling and buckling analysis of anisogrid composite lattice cylindrical shells.* Composite Structures, 2011. 93(2): p. 308-323.
44. Vasiliev, V.V., V.A. Barynin, and A.F. Razin, *Anisogrid composite lattice structures–development and aerospace applications.* Composite structures, 2012. 94(3): p. 1117-1127.
45. Vasiliev, V., V. Barynin, and A. Rasin, *Anisogrid lattice structures–survey of development and application.* Composite structures, 2001. 54(2): p. 361-370.
46. Vigliotti, A. and D. Pasini, *Mechanical properties of hierarchical lattices.* Mechanics of Materials, 2013. 62: p. 32-43.
47. Jeon, S.K., J. Banik, and M. Peterson. *Free deployment of a sparse-isogrid column with high strain composite ribs*. in *3rd AIAA Spacecraft Structures Conference*. 2016.
48. Totaro, G., *Flexural, torsional, and axial global stiffness properties of anisogrid lattice conical shells in composite material.* Composite Structures, 2016.

Thermal Morphing Anisogrid Smart Space Structures Part 2: Ranking of Geometric Parameter Importance, Trust Region Optimization, and Performance Evaluation.

Austin A. Phoenix
United States Naval Research Lab, Naval Center for Space Technology

Jeff Borggaard, Pablo A. Tarazaga
Virginia Tech, Vibrations, Adaptive Structures, and Testing Lab
310 Goodwin Hall, Blacksburg, VA, 24060

Abstract: As future space mission structures are required to achieve more with scarcer resources, new structural configurations and modeling capabilities will be needed to meet the next generation space structural challenges. A paradigm shift is required away from the current structures that are static, heavy and stiff, to innovative lightweight structures that meet requirements by intelligently adapting to the environment. As the complexity of these intelligent structures increases, the computational cost of the modeling and optimization efforts become increasingly demanding. Novel methods that identify and reduce the number of parameters to only those most critical, considerably reduce these complex problems allowing highly iterative evaluations and in-depth optimization efforts to be computationally feasible. This parameter ranking methodology will be demonstrated on the optimization of the thermal morphing anisogrid boom. The proposed novel morphing structure provides high precision morphing through the use of thermal strain as the sole actuation mechanism. The morphing concept uses the helical members in the anisogrid structure to provide complex constrained actuations that can achieve 6 Degree of Freedom (DOF) morphing capability. This structure provides a unique potential to develop an integrated structural morphing system, where the adaptive morphing capability is integrated directly into the primary structure. To identify parameters of interest, the Q-DEIM model reduction algorithm is implemented to rank the model parameters based on their impact on the morphing performance. This parameter ranking method provides insight into the system and enables the optimal allocation of computational and engineering resources to the most critical areas of the system for optimization. The methodology, in conjunction with a Singular Value Decomposition (SVD), provides a ranking and identifies parameters of relative importance. The SVD is used to truncate the nine parameters problem at two locations, generating a five parameter optimization problem and a three parameter optimization problem. To evaluate the ranking a parameter sweep in conjunction with a simple minimum cost function search algorithm will compare all 120 five parameter ranking orders to the Q-DEIM ranking. This reduced parameter set significantly reduces the parameter complexity and the computational cost of the model optimization. This paper will present the methodology to define the resulting performance of the optimal thermal morphing anisogrid structure, minimum morphing control, and the systems frequency response capability as a function of available power.

1. Introduction

The intent of this work is to define the limits of the morphing accuracy achievable by this novel thermal morphing anisogrid smart structure, initially discussed by the authors in [1] and [2]. Previous work has introduced the morphing concept, identified the geometric parameters of interest, defined the modeling and loading requirements, developed the thermal morphing performance metrics, and demonstrated the capability of the parameterized finite element model used (FEM) to optimize this complex structure. The Matlab code used to develop the FEM model and loading input can be found at (https://github.com/A-Phoenix/Anisogrid-Model). The critical technical challenges to be addressed include morphing accuracy, power requirements, workspace quality, and thermal control accuracy requirements. These challenges associated with the thermal morphing anisogrid smart structure are to be addressed through a reduced optimization methodology [3, 4] used to define minimum morphing performance. The intent of this investigation is to contribute an alternate morphing concept to address the smart structural challenges in future space missions.

The field of adaptive smart structures has been established in the vibration isolation, thermal distortion, deployment control, and intelligent control fields [5-20]. Adaptive smart hexapod systems [19] have been implemented in high precision applications [20]; specifically the Hobby-Eberly Telescope [21-23] with great success. The intent of this concept is to expand on the hexapod concept by providing a significantly reduced global morphing displacement relative to the length of the input actuation. This high morphing capability is achieved through the use of thermal strain as the sole actuation mechanism. Thermal strain has been implemented as the actuation mechanism at the micro and macro scales with both biomaterial and bi-stable structures [24-36]. Depending on the morphing application, this concept can be implemented using low Coefficient of Thermal Expansion (CTE) materials to achieve high precision morphing, or use high strain materials, such as shape memory alloys, to achieve large displacement morphing capability. Shape memory alloys have been shown to provide the force and large displacements required for high displacement applications [37-41]. While the large displacement application shows potential, this effort is focused on the high precision morphing application more closely related to large-scale optics control [11, 42-44]. Low CTE materials in conjunction with precise thermal control capability are conceptually implemented in this work to achieve high precision morphing. These thermal strains are applied to helical members through the direct application of local and global temperature gradients. These thermal strains push, pull and twist the system providing 6 DOF morphing capability.

This paper looks to develop methods that reduce the overall complexity of the model optimization while maintaining accurate behavior through identifying and allocating resources to the most critical input parameters. The model reduction methodology used herein was initially developed by the authors in [3, 4] to reduce the number of parameters used for a complex model correlation processes.

The complex morphing optimization with six continuous and three non-continuous parameters is computationally expensive. This is addressed by implementing a method to reduce the number of optimization parameters. The method chosen to reduce the optimization is a parameter ranking method using the model reduction method Q-DEIM [45] to generate a parameter ranking as detailed in [2] and [4]. The resulting ranking, in conjunction with a Singular Value Decomposition (SVD) analysis, defines two reasonable truncation points, reducing the number of parameters to three and five parameters, respectively. A parameter sweep is used to define approximate optimized cost functions for all possible combinations of the 120 ranking paths. This paper will demonstrate and determine the resulting quality of this novel parameter ranking methodology as applied to the thermal morphing optimization.

There is a significant body of work on the various sensitivity analysis sampling methods[46-51] focused on both deterministic methods [52] and statistical methods[53]. To solve this problem local, rather than global, sensitivity analysis methods [54] were chosen because the computational cost of the FEM prohibits the use of global or statistical methods due to the many more simulations required to obtain representative results. The sampling choice to use the minimum and maximum allowed parameter value in the design space was chosen based on the sampling choice study provided in [3]. This specific choice is important as this sampling method, in conjunction with the Q-DEIM method, enables an engineer to develop a ranking using only $2n + 1$ FEM runs, where n is the number of parameters to be ranked. The Q-DEIM ranking inputs can be generated by hand and prevents the development of an iterative FEM capability for all parameters to be ranked. The Q-DEIM method in conjunction with the chosen sampling method is computationally efficient and provides quality ranking results without the need for iterative FEM capability.

A trust-region optimization code is implemented to solve the non-convex optimization problem. Due to the nature of the non-continuous parameter, independent optimization problems are solved for feasible, fixed numbers of helical members, then corresponding optimal results are compared to select the final design. The optimization is performed on the three and the five parameter design space, and the resulting morphing quality is discussed.

This paper will detail the morphing concept and the modeling decisions in Section 2. The method to define the parameter importance and parameter reduction method is described in depth in Section 3, and the parameter ranking, shown in Section 4, is used to determine the resulting ranking quality in Section 5. The optimization method is outlined in section 6. The resulting optimized geometry and the corresponding performance of the concept are covered in Section 7.

2. Morphing Concept Configuration

The morphing concept used in this study is based on the configuration described and detailed in [2]. The configuration and all input parameters, seen in Figure 50, will be discussed briefly for completeness. The anisogrid morphing structural FEM is built by defining the nine geometric parameters, listed in Table 8, with a parameterized Matlab code to generate the element-by-element model. The design space is limited to ensure satisfaction of model assumptions to guarantee the final structure is coherent. Material normalization is used to enable the output of a single FEM to represent a wide variety of material choices by scaling the results. The only parameters affected by the initial material selection of invar are those parameters defining the cross section of the individual helical and cylindrical members. If a material is chosen other than invar, the helical and cylindrical cross sections will need to be scaled to provide the same axial and bending stiffness values.

Table 12. Parameter Nominal, Maximum, and Minimum allowed value in the design space.

Param. Number	Parameter Name	Nominal Value	Max Value	Min Value	Units
1	# of Helicals	20	34	6	-
2	Radius	0.25	0.5	0.0625	(m)
3	Pitch	π	3.25 π	.25 π	(m)
4	Hel IR	0.005	0.05	0.001	(m)
5	Hel Thickness	0.005	0.05	0.001	(m)
6	Cyl IR	0.005	0.05	0.001	(m)
7	Cyl Thickness	0.005	0.05	0.001	(m)
8	Base Constraint	123	123456	123	DOF
9	Top Constraint	123	123456	123	DOF

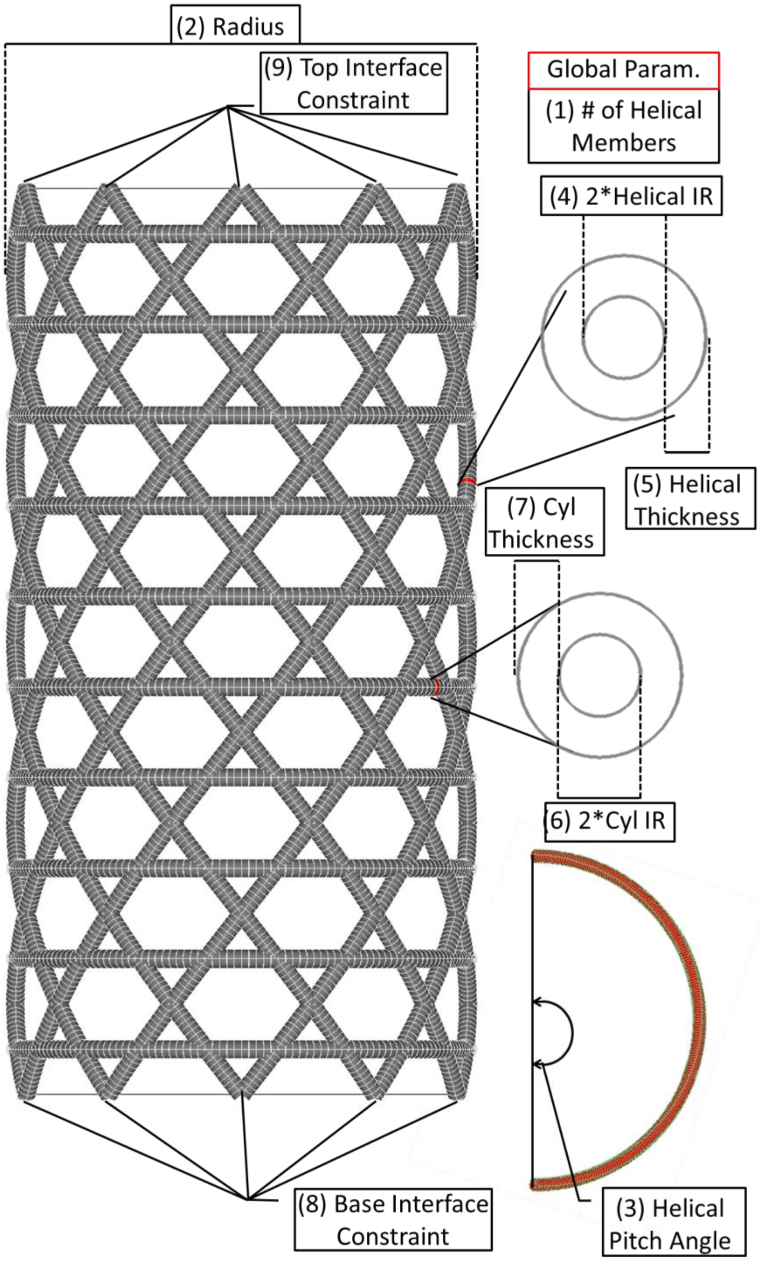

Figure 50. Anisogrid Geometry with all 9 Geometric Parameters of Interest.

3. Parameter Ranking

A sensitivity analysis provides insight into an individual parameter's impact on the system and quantifies the relative parameter importance. The methodology used here takes advantage of the Q-DEIM model reduction method [55] to identify the parameters that have the most independent impact on a set of normalized single helical loading output displacement vectors. In this case, that independence is used as an indicator for the parameters relative importance for a subsequent geometric optimization. The ranking is used in conjunction with an SVD analysis to identify the minimum number of required parameters for optimization, thereby reducing the computational cost and the resulting optimization complexity. This methodology has been previously demonstrated by the authors on model correlation in [3] and [4], as well as ranking sensor importance [56].

The first step in the parameter ranking is the development of the Sensitivity Input Matrix as seen in Figure 51. Through previous work [3, 4], it was discovered that the evaluation of each parameter's individual importance could be done by calculating the normalized parameter impact at the maximum and minimum values in the design space. This small input set has been shown to produce accurate parameter ranking with minimal computational cost. To build an input for the Q-DEIM reduction method, the maximum and minimum parameter values are evaluated independently, as detailed in Equation 1 and seen in Figure 52.

$$S_{input}(1:19,:) = [P_1, P_2, \dots, P_9]\,, for\ i = 1:9\ S_{input}(i+1, i) = P_i^{Max} \qquad [1]$$

$$and\ for\ i = 10:19\ S_{input}(i+1, i-9) = P_{i-9}^{Min} \qquad [2]$$

Where S_{input} is the Sensitivity Input Matrix, P_i is the i^{th} input parameter, and P_i^{Max} and P_i^{Min} are the max and minimum allowed value for the i^{th} input parameter. Equation 1 and 2 are used to develop the Sensitivity Input Matrix (S_{input}) as visualized in Figure 51.

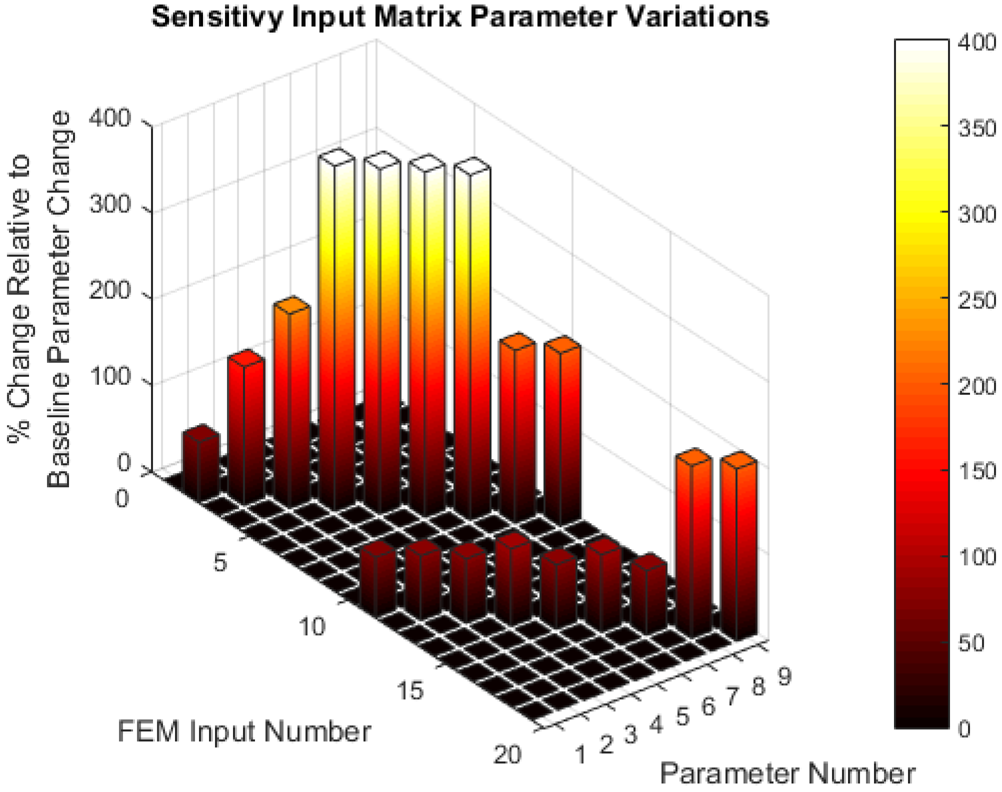

Figure 51. Sensitivity Input Matrix Visualization.

Each row of the S_{input} matrix is the nine parameter inputs for each of the *n* FEM models where *n* is the number of rows in the S_{input} matrix. The resulting 6 DOF outputs from the FEM model are all normalized by the nominal response (seen in yellow in Figure 52) resulting in 18 normalized 6×1 displacement vectors that are concatenated into a single matrix to generate the 9×12 Sensitivity matrix, S, as seen in Figure 52. This sensitivity matrix is then input to a Q-DEIM reduction algorithm that generates a 9 parameter ranking. The process is schematically laid out in detail in Figure 52.

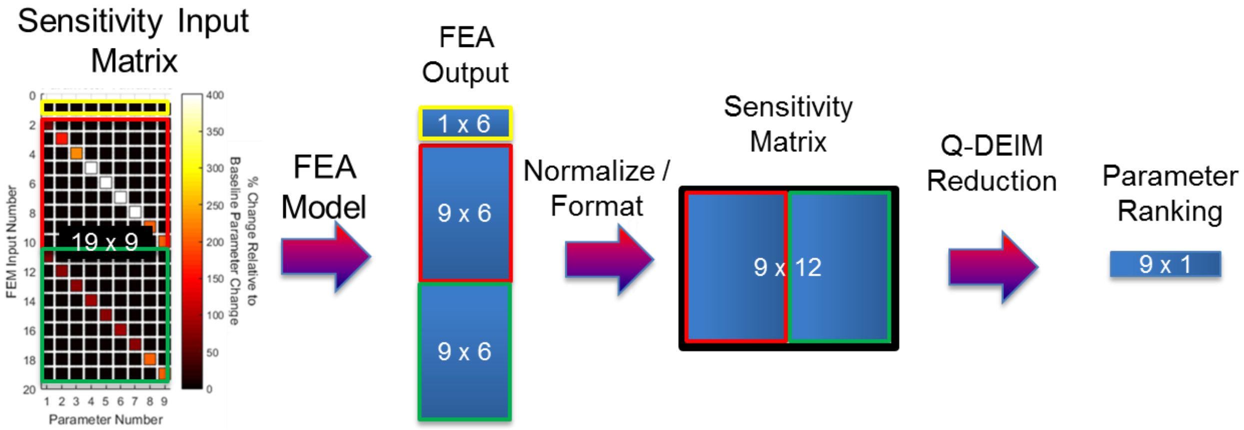

Figure 52. Parameter Ranking Data flow from the Sensitivity Input matrix to the Parameter Ranking with the Nominal Geometry shown in Yellow, the Maximum Input values shown Red and the Minimum Input Values shown in Green.

Equation 3 shows the normalization method used on the raw FEM output. The i^{th} 6 DOF displacement vector is normalized by the nominal displacement vector. The difference is then scaled by the percentage of the i^{th} parameter change versus the nominal i^{th} parameter value as,

$$\frac{D_{(i)} - D_1}{(P_i - P_1)/P_1}, \qquad [3]$$

where $D_{(i)}$ is the i^{th} displacement vector, D_1 is the nominal displacement vector, P_i is the i^{th} parameter value, and P_1 is the nominal parameter value. To identify the number of important parameters in the system an SVD analysis, shown in Figure 53, is performed on the 9×12 Sensitivity matrix.

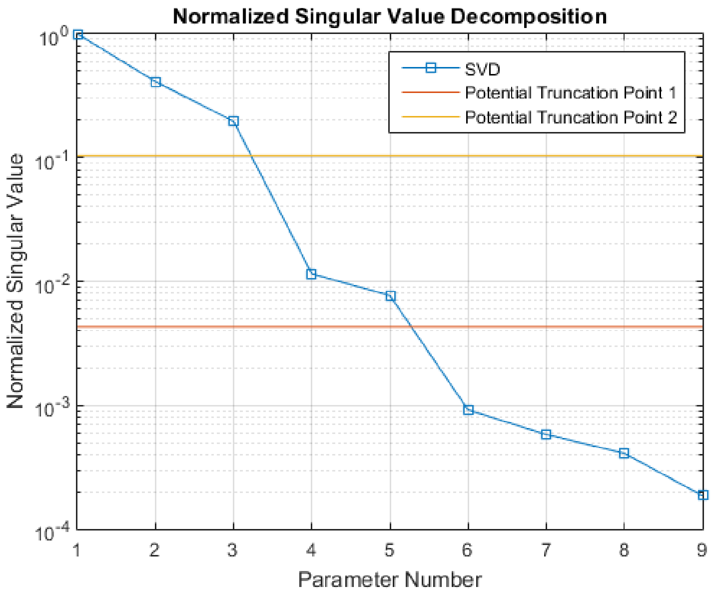

Figure 53. Normalized Sensitivity Matrix SVD using all Positive Parameter Changes with the Two Possible Truncation Points Identified.

While the Q-DEIM algorithm provides a ranking of the parameters, the relative importance of the parameters can only be determined in conjunction with the SVD analysis. The SVD analysis decomposes the system via its singular values and vectors to identify and maintain the most important modeling information in the reduced model. This importance is linked to the relative values associated with the singular values of the decomposition. To incorporate the dominant behavior of the total model relative to the scale of the reduced model, truncation points are placed where a drop in the singular values occur. In this case, as seen in Figure 53, a truncation at five and three parameters should be evaluated as candidate points. Thus, through a Q-DEIM and SVD analysis, the parameters are ranked, and a relative importance can be found allowing for a parameter reduction to take place via truncation of the model. The resulting ranking from the Q-DEIM method can be seen in Table 13.

Table 13. The Q-DEIM Parameter Ranking from Most Independent to Least Independent Parameter.

Param. Number	Parameter Name	Param. Number
1	# of Helicals	1
2	Pitch	3
3	Radius	2
4	Hel Thickness	5
5	Cyl Thickness	7
6	Base Constraint	8
7	Hel ID	4
8	Top Constraint	9
9	Cyl ID	6

While previous work indicated that the number of helical members, the helical pitch angle, and the radius were important parameters the rest of the ranking does not match intuitive assessments. This was the experience in previous work [3, 4] where the intuitive order was not often the correct order. This demonstrates the need for algorithms that provide parameter ranking due to the complexity of this relatively simple system. It is possible that the parameter may be ranked higher than it should due to the method evaluating both the scale of the effect and the uniqueness of the effect on the morphing. To prevent incorrect rankings, parameters with a unique but minimal effect, like the top and base constraint parameters, could be evaluated further.

4. Parameter Sweep

Now that the parameters of importance have been identified in Section 3, a parameter sweep is performed to gain further insight into the cost function (developed in [2] and shown in Equation 4) relative to the three parameters and five truncation points. The first design space contains the top three parameters of interest: the number of Helical Members, the Helical Pitch Angle, and the Radius. The second design space includes the first three ranked parameters as well as the Helical Member Thickness, and the Cylindrical Member Thickness. The sweep provides insight into appropriate initialization points and locations for potential local and global optimization minima. The five parameter sweep also provides the opportunity to quantify the ranking quality of Q-DEIM relative to all other possible five parameter ranking orders.

The geometry's minimum morphing capability will be quantified by evaluating the single helical displacement vector. Minimizing the cost function, as seen in Equation 4, will minimize the displacement vector length of single helical displacement vectors that are combined to generate geometry specific minimum morphing case.

$$Cost\ Function = \frac{D_x^2 + D_y^2 + D_z^2 + D_{rx}^2 + D_{ry}^2 + D_{rz}^2}{6}, \qquad [4]$$

where D is the six degree of freedom single helical loading displacement vector, measured at the tip of the anisogrid boom.

4.1 Three Parameter Sweep

To generate the three parameters sweep, 13 radius values, 13 pitch angles, and 15 different helical numbers were combined to generate 2535 unique geometries. The parameter sweep in Figure 54, is a 4D plot with the number of helical members, the anisogrid radius, and the helical pitch angle on the X, Y, and Z axis, respectively. The size and color of the marker is plotted as the inverse of the cost function to visualize the cost function as the 4th dimension. As can be seen in Figure 54 (b) through (c), the plot allows viewing of the variation through the thickness of the plot showing change along each axis and allowing the identification of the regions of local and global optimal cost functions.

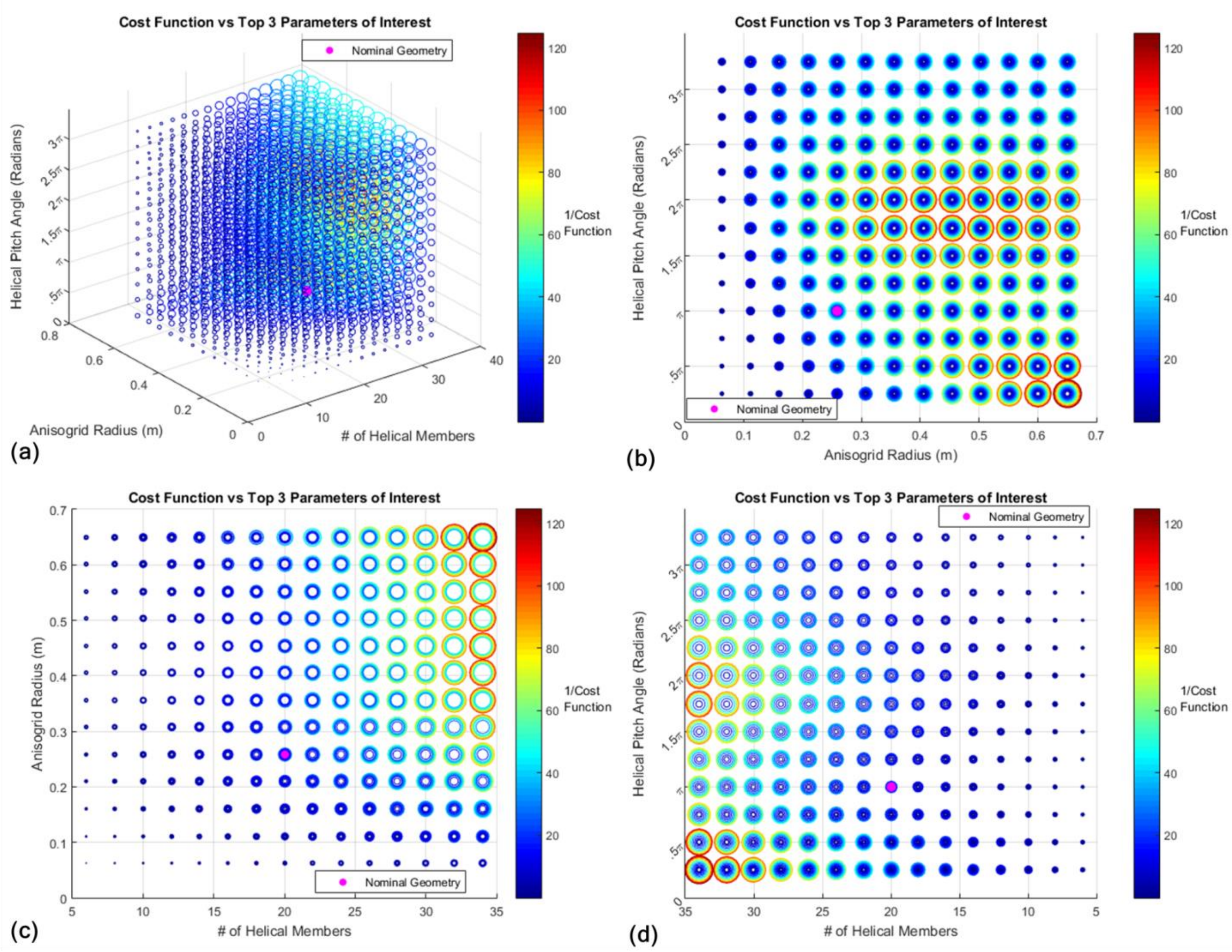

Figure 54. (a) Cost Function in the Three-Parameter Design Space, (b) Helical Pitch vs. Anisogrid Radius, (c) Anisogrid Radius vs. # of Helical Members, (d) Helical Pitch Angle vs. # of Helical Members.

4.2 Five Parameter Sweep

Since it is computationally prohibitive to develop a five parameter sweep while maintaining the sweep density used in the three parameter sweep, a reduced sweep density is used. This reduced sweep density, for the five parameter system, consists of a total of 5000 evaluation points. This is a sweep of five parameters for Helical Pitch Angle, Anisogrid Radius, Helical thickness, and Cylindrical thickness, with an eight parameter sweep for the number of Helical Members. To plot this increased density data with six dimensions, Figure 55 consists of six figures; the overall system plot and a plot for each anisogrid sweep. At each sweep point in Figure 55 (a) 25 cost functions are plotted, one for each of the possible combinations of helical thickness and cylindrical thickness. To visualize the variation in the cost function as the fourth and fifth parameters are varied, Figure 55 (b) through Figure 55(f) demonstrate the change in the cost function as the radius is held constant and all other parameters are varied.

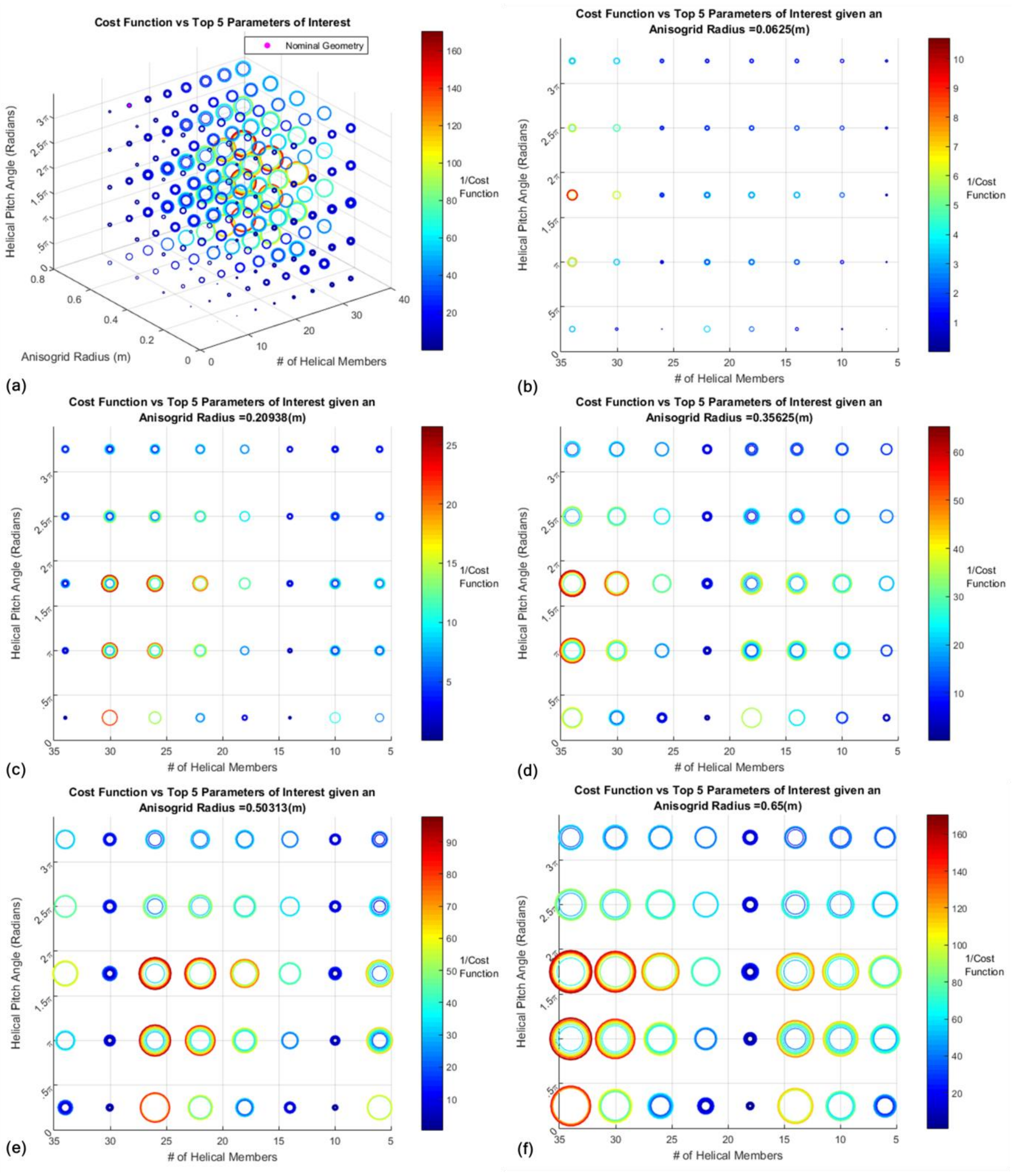

Figure 55. Five Parameter Sweep Design Space for (a) Full Isometric View, (b) Anisogrid Radius of .0625 m, (c) Anisogrid Radius of .2 m, (d) Anisogrid Radius of .36 m, (e) Anisogrid Radius of .5 m, (f) Anisogrid Radius of .65 m.

5. Parameter Ranking Quality Evaluation

To better understand the effect that the optimization parameter order has on the morphing quality, and define the quality of the Q-DEIM ranking, it is important to comprehend how the optimized cost function varies as a function of the number and order of parameters optimized. The intent of this investigation is to find the minimum optimization path from the nominal geometry to a sufficiently optimized structure. A true optimization of all possible parameter orders is computationally too expensive, so the simple method of searching is used through the five-dimensional parameter space, developed in Section 4.4.2. For the Q-DEIM ranking [1, 3, 2, 5, 7] the parameter ranking method searches through the top ranked parameters dimension (the # of Helical Members) in the five-dimensional parameter sweep. The minimum value in this search defines the Q-DEIM ranking's one parameter optimized cost function. This is repeated for the two parameter sweep dimensions associated with the top two ranked parameters (number of Helical Members, Helical Pitch Angle), generating the two parameters optimized cost function. This is then repeated for the top 3, 4, and all five parameters. These values are plotted for all 120 possible ranking orders in Figure 56.

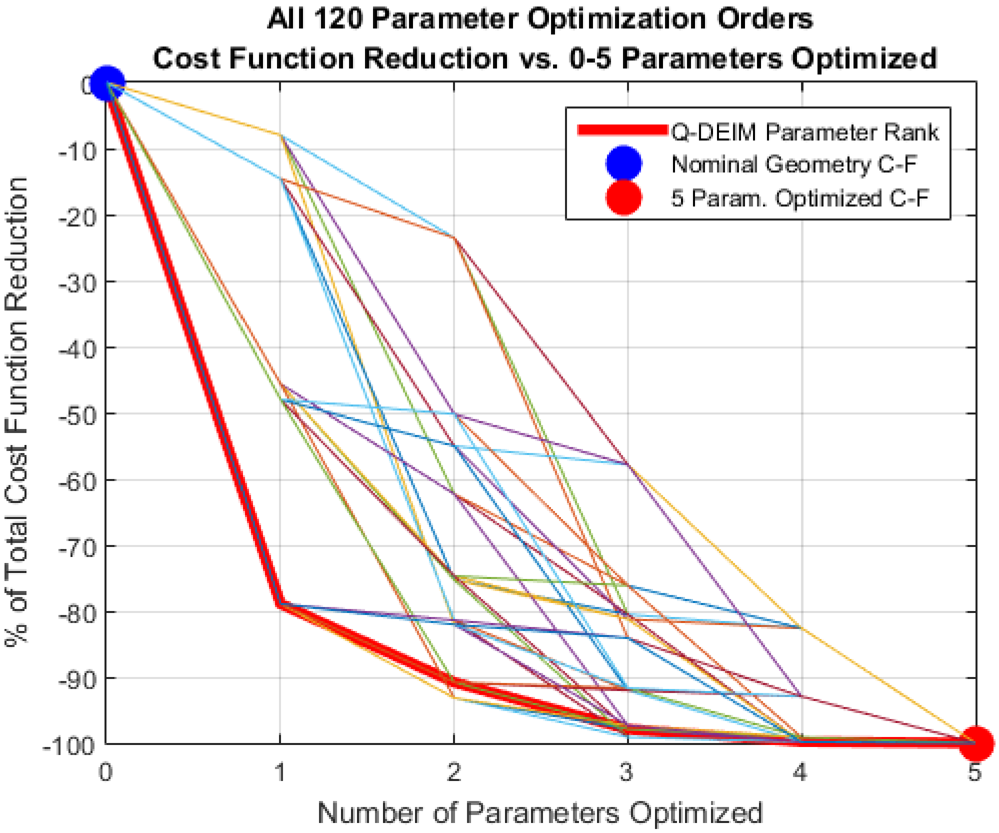

Figure 56. All 120 Parameters Optimization Orders and the Resulting Optimized Cost Function.

Through this investigation, it is apparent that the parameter ranking order used to optimize the structure has a significant effect on the resulting quality of the optimization. All 120 rankings follow a path from the nominal geometry to the five parameters optimized cost function, but the area under that curve indicates how efficiently that path was taken. The use of an efficient optimization path reduces the overall optimization effort by identifying the right optimization parameters and the correct number of optimization parameters upon initial assessment. While the Q-DEIM does not provide the absolute optimal ranking, the Q-DEIM three parameter ranking achieves 97.9% of the total five parameters ranking cost function reduction. This justifies the use of Q-DEIM ranking and the three parameter truncation point. The best, worst, and Q-DEIM rankings results are detailed in Table 14.

Table 14. The Percent of Cost Function Reduction Relative to the 5 Parameter Optimized Cost Function Sweep for the Q-DEIM ranking, the Best Overall Ranking, and the Worst Overall Ranking.

	% of Total Cost Function Reduction For Three Param Ranking Orders					
	Q-DEIM Ranking		Best Ranking		Worst Ranking	
# of Params Optimized	% of Total Reduction	Param Optimized	% of Total Reduction	Param Optimized	% of Total Reduction	Param Optimized
1	78.9	1	78.9	1	8.0	7
2	90.8	3	93.2	2	23.5	5
3	97.9	2	99.1	5	57.8	3
4	99.8	5	99.8	7	82.6	2
5	100	7	100	3	100	1

The Q-DEIM ranking method performs well compared to the optimal ranking for this specific design space resulting in a difference of less than 3% of the total cost function reduction capability. Further study is required to better define the ability of this methodology as applied to the ranking of optimization parameters. The differences between the optimized cost function and the Q-DEIM ranking could be due to the differences between the minimum parameter sweep search value, used here, and a true optimization. A larger set of data where the Q-DEIM ranking is used on various optimization problems could provide a much more detailed representation of the ranking capability.

6. Optimization

This geometry does not present a simple optimization problem due to the variable design space limits, non-continuous parameters, structural discontinuities, and the black box nature of the FEM algorithm. Furthermore, as we describe below, changes in geometry through the finite element mesh leads to numerical noise in the objective function, cf. [56].To address these issues, a trust-region optimization is used to optimize the morphing capabilities [57]. Further complicating the optimization problem, parameter bounds need to be functions of the input parameters, such as the number of helical members, to ensure only reasonable geometries are developed. Bound constraints on the optimization parameters are applied to ensure consistent geometric outputs, resulting in a reduced design space for the helical pitch angle as well as the cylindrical and helical outer radii as functions of the number of helical members. A trust-region optimization algorithm with bound constraints is implemented through the use of the Matlab optimization code *entrust* based on the pseudocode in [58]. This software is open source code and can be found at (https://github.com/jborggaard/entrust).

6.1 Trust Region Optimization Method

The trust-region algorithm described in [57, 58] develops a quadratic approximation of the cost function in the constrained optimization problem. If the predicted reduction in the model does not match the actual reduction of the function within a sufficient tolerance, the trust region radius is reduced until the reduction obtained with the quadratic model adequately matches the actual reduction of the function. Once the simplified quadratic model is verified, it is used to choose the next step direction, and the process is repeated until the overall optimization criteria are met. Likewise, if the predicted reduction is found to be a good representation of the actual reduction, the trust region radius is increased. The key factors for the trust-region algorithm are the initial values for the n parameters, the n optimization bounds, the trust region radius, the n parameter gradients, the initial cost function, the step size used to evaluate the gradient, and the convergence tolerances. Given the large number of parameters, the hessian is too computationally expensive to calculate for this problem. Thus, we make use of a Secant method (we selected the BFGS algorithm), to replace the second derivative with a suitable approximation. The BFGS algorithm is implemented as described in [59].

Due to the nature of the FEM development, numerical noise in the optimization is to be expected. It has been shown that numerical noise issues can be mitigated through careful selection of the step size used to calculate the gradient [59-61]. A gradient study is performed in Section 6.2 to choose an appropriate step size. The intent of the gradient evaluation is to find a step size that accurately predicts the local gradient despite the numerical noise and discontinuities. This method effectively provides an implicit filtering mechanism, as described in [62], by smoothing the cost function to combat the known structural discontinuities and numerical noise inherent in the FEM.

For each optimization run, $1 + n$ files, where n is the number of optimization parameters, are created to calculate the cost function and the n gradients. The first FEM simply evaluates the cost function at the point requested by the optimization code. Then for $i = 1{:}\, n$ parameters of interest, n additional FEMs are generated with a delta applied to the i^{th} parameter. This delta or step size is an important choice to ensure stability of the optimization code, as is discussed in Section 906.2. The resulting n cost functions are used to generate the gradient in each of the n parameters of interest using a simple forward difference calculation.

6.2 Gradient Evaluation

A study was performed to identify the proper step size for the gradient calculation in the optimization analysis. There is a known discontinuity associated with the helical pitch angle and the global stiffness properties. As the pitch angle increases beyond π rad, the end segment of the helical member acts as a cantilever beam of increasing length until another helical member is intersected. As the beam intersects the next helical member, the local stiffness increases, resulting in a minor increase in global stiffness and a discontinuity in the cost function. A dense pitch sweep was performed through 1% of the helical pitch angle design space using 1000 points located around a value of π rad. The resulting cost function can be seen in Figure 57.

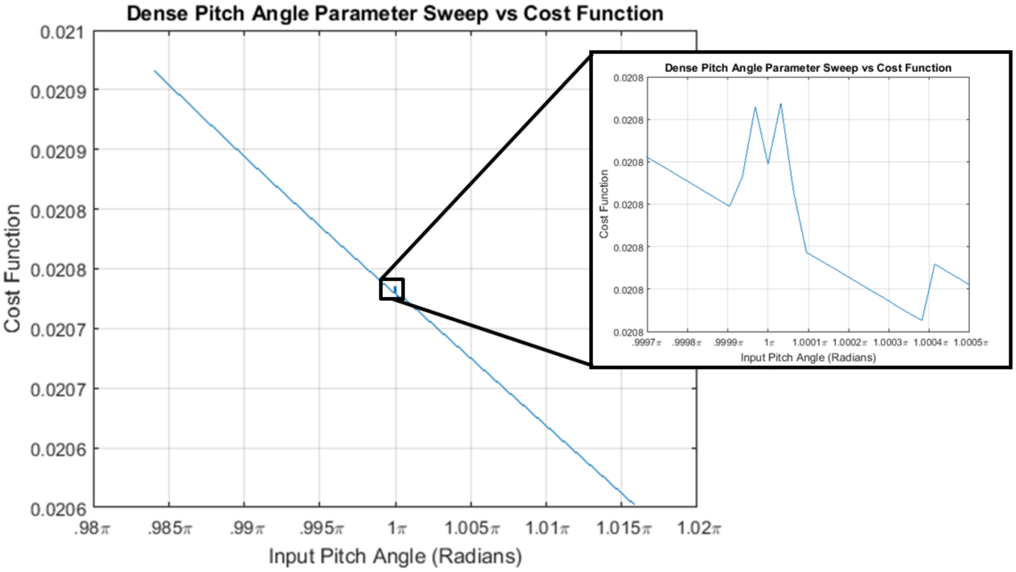

Figure 57. Dense Pitch Angle Sweep to Identify the Minor discontinuity in the cost function.

The resulting impact on the cost function is more complex than expected due to local imperfections in the modeling of the region directly around the discontinuity. These imperfections are caused by the merging of nodes that do not perfectly align and result in short or angled elements. These modeling choices have little to no effect on the actual cost function, but introduce minor discontinuities at the scale investigated in this parameter sweep. While the overall cost function in the full pitch parameter sweep changes less than $5x10^{-6}$ at that discontinuity, the small variation around the discontinuity induces gradient issues if the step size is not chosen intelligently. The gradient study is performed using an input pitch angle step of $1 \times 10^{-4}\, rad$ and 1000 steps. This allows a variety of step sizes to be evaluated. The step sizes chosen for the evaluation are listed in Figure 58 (a).

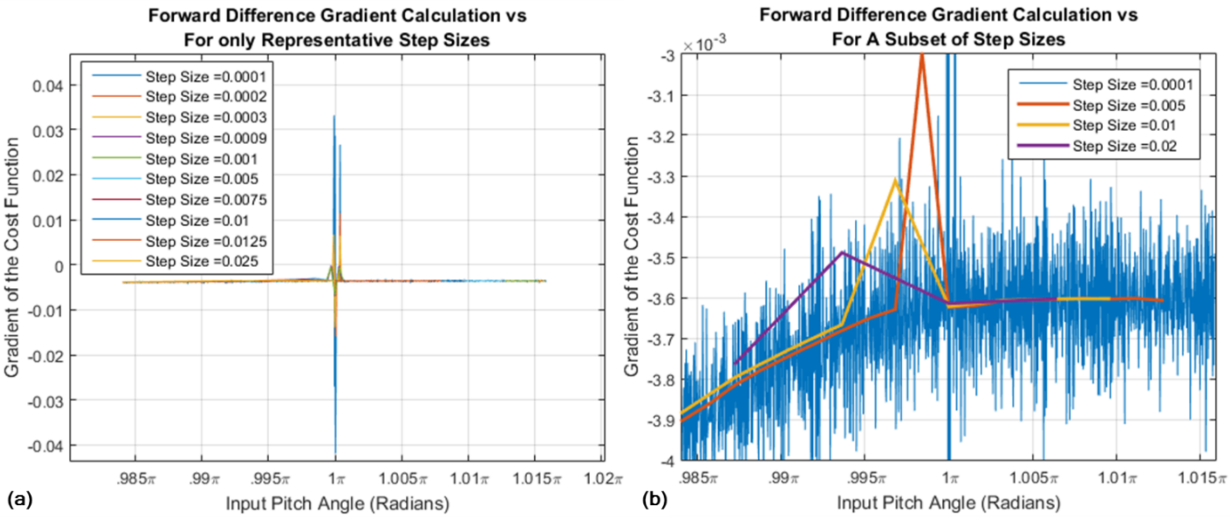

Figure 58. Gradient Investigation under a variety of Gradient Step Sizes Calculated Using Forward Difference for (a) all Possible Step sizes, (b) View of Numerical Noise and the Step Sizes that are Sufficiently Small to Represent the Step Sizes Accurately.

The choice in step size has a significant effect on the optimization as is proven in Figure 58 (a). If the step size is too small, local deviations introduce false gradient values, and if the step size is too large, local effects can be missed. By investigating the numerical noise in the system, demonstrated by the .0001 rad step size, a step size of .02 radians was chosen. This choice ensures that the errors associated with the discontinuity are less than the numerical noise measured in the smallest step size seen in Figure 58 (b). The step size choice is made for the discontinuity in the helical pitch angle but is applied to all variables in the optimization for simplicity.

6.3 Three Parameter Optimization

The first optimization evaluates three parameters: the number of helical members, the helical pitch angle, and radius, given by the Q-DEIM ranking. Due to the nature of the number of helical members, this variable is optimized iteratively by performing 15 two-parameter optimizations at all even values of the parameter in the design space. A limit is applied to the design space, as described in Section 6.3.1, to ensure all geometric configurations are reasonable. The resulting limits and optimized geometries can be seen in Table 16.

6.3.1 Three Parameter Design Space Limit Development

The original design space contains geometric combinations that exceed the limits of feasibility and result in breaches in modeling assumptions. This occurs when the cylindrical and helical members are close enough, or the radius is large enough that they fill the majority of the volume. The FEM assumptions loose viability and manufacturing becomes impossible. Therefore, a cylindrical vertical fill factor (detailed in Equation 6) is limited to 66%. A design space limit is developed as a function of the Number of Helical Parameters. The number of cylindrical members can be calculated using the number of helical members and the helical pitch angle as

$$N_{Cyl} = N_{Hel}\frac{Pitch}{2\pi} \quad , \qquad [5]$$

where the number of cylindrical members is N_{Cyl}, the number of helical members is N_{Hel}, and $Pitch$ is the helical pitch angle in radians. A second key factor in defining the radius limit is identifying the ratio of the radius to the gap between cylindrical members, also known as the Fill Factor and described as,

$$Fill\ Factor = \frac{2R_{Cyl}}{Z_{Cyl}(2) - Z_{Cyl}(1)} \qquad [6]$$

where the Radius of the cylindrical members in meters is R_{Cyl}, and $Z_{Cyl}(i)$ is the Z axis location of the i^{th} cylindrical member. This *Fill Factor* is a dimensionless parameter used to limit the structure to ensure reasonable geometric configurations. Another way to evaluate this equation is listed below.

$$D_{max} = \frac{Height}{N_{Cyl}} * Fill\ Factor, \quad R_{max} = \frac{D_{max}}{2} \qquad [7]$$

where D_{max} is the maximum diameter in meters, R_{max} is the maximum radius in meters, and $Height$ is the anisogrid boom height in meters. This equation can be used to generate a given limit to the design space. This is demonstrated for the three parameter case where the helical and cylindrical parameters are held at the nominal value. To meet the desired $Fill\ Factor$, and maintain the helical and cylindrical radius above the nominal value, the helical pitch angle is limited as a function of the number of helical members. This limit only occurs when the number of helical members exceeds 20 as seen in Figure 59 and Table 15.

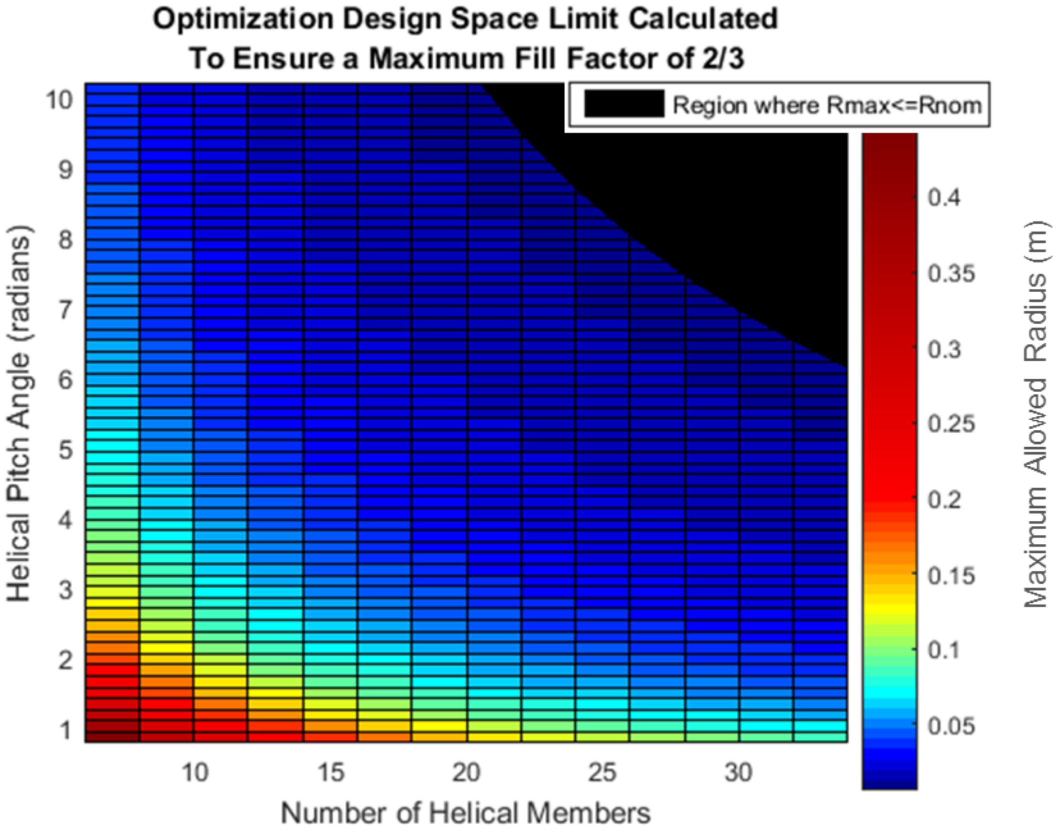

Figure 59. Three Parameter Optimization Design Space with the Limit On the Design Space Shown in black where $\boldsymbol{R_{Max} \leq R_{Nominal}}$ resulting in a Fill Factor of Less than 66% for the Nominal Geometry.

This discrete parameter (Number of Helical Members) is evaluated through iterative optimization to limit the optimization complexity. This provides a simple method to limit the three parameter optimization. The bound on the three parameter optimization, applied for the Max Helical Pitch angle, is updated for all fifteen iterations of the Number of Helical Members. The resulting Helical Pitch Angle Limits are seen in Table 15.

Table 15. Max Helical Pitch Angle to Achieve a Fill Factor of 66% as a Function of Number of Helical Members with Global Design Space Parameter Limits Highlighted in Black.

	3 Parameter Optimization Design Space Limit														
Max Helical Pitch Angle (π rad)	1.96	2.07	2.21	2.36	2.56	2.77	3.01	3.25	3.25	3.25	3.25	3.25	3.25	3.25	3.25
Number of Helical Members	34	32	30	28	26	24	22	20	18	16	14	12	10	8	6

Using the parameter space limits in conjunction with the Entrust optimization code, a three parameter optimization can be performed. This optimization requires 15 unique optimization runs, one for each of the number of helical members under investigation. The results from the 15 optimization runs are seen in Table 16.

Table 16. Global Optimal Results for the 3 Parameter Optimization with Pitch Angle Limits Highlighted in Black.

3 Parameter Optimization Design Space Limit		Global Optimum		
Number of Helicals	Max Helical Pitch Angle	Optimized Radius	Optimized Pitch Angle	Cost Function
34	1.96 π	6.250E-01	1.030E+00	8.288E-03
32	2.07 π	6.250E-01	1.006E+00	9.387E-03
30	2.21 π	6.250E-01	1.008E+00	1.070E-02
28	2.36 π	6.250E-01	1.018E+00	1.231E-02
26	2.56 π	6.250E-01	1.012E+00	1.431E-02
24	2.77 π	6.250E-01	1.019E+00	1.683E-02
22	3.01 π	6.250E-01	1.012E+00	2.006E-02
20	3.25 π	6.250E-01	1.006E+00	2.435E-02
18	3.25 π	6.250E-01	1.021E+00	3.012E-02
16	3.25 π	6.250E-01	9.944E-01	3.823E-02
14	3.25 π	6.250E-01	1.016E+00	5.014E-02
12	3.25 π	6.250E-01	1.018E+00	6.860E-02
10	3.25 π	6.250E-01	1.023E+00	1.004E-01
8	3.25 π	6.250E-01	9.899E-01	1.594E-01
6	3.25 π	6.250E+00	9.429E-01	2.974E-01

The three parameter optimal geometry is found to have 34 helical members, a radius of .625 m, and a helical pitch angle of 1.03 radians. This geometry results in an optimal cost function of 8.288e-3. The resulting optimal geometric configuration is seen in Figure 60.

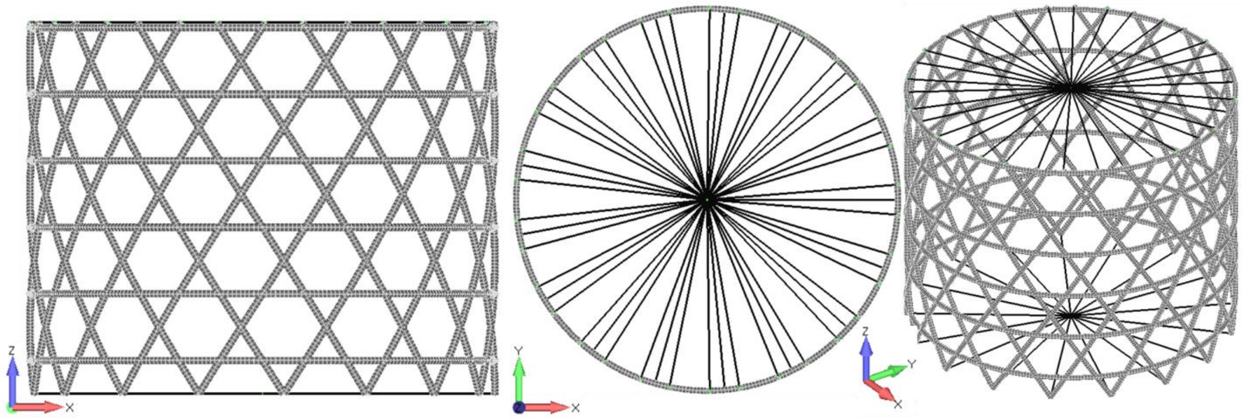

Figure 60. Three Parameter Global Optimal Geometry with 34 Helical M Radius of .625 m and a Helical Pitch angle of 1.03 rad.

6.4 Five Parameter Optimization

The five parameter optimization adds the two additional optimization parameters, helical member thickness, and cylindrical member thickness. The addition of the member thickness increases the complexity of the required design space limit. To ensure reasonable geometries, cylindrical and helical member radius will be limited along with the allowed helical pitch angle. The three parameter optimized value will be used as the initial point to define the member radius limit, as described in Section 946.4.1, to achieve reasonable geometries.

6.4.1 Five Parameter Design Space Limits

The five parameter limits use the helical pitch angle from the three parameter optimization to provide an initial estimation on the cylindrical and helical maximum allowed radius, as seen in Figure 61. A given three parameter optimization point is projected onto the 66% fill factor maximum radius curve to define the maximum allowable radius at that point in the design space. The corresponding radius limit of the projected point is used to set the initial cylindrical thickness and helical thickness limits for the five parameter optimization. If the resulting five parameter's optimal geometry does not meet the design space limit, the resulting cylindrical thickness and helical thickness limit will be updated, and the optimization will continue to iterate until design requirements are met.

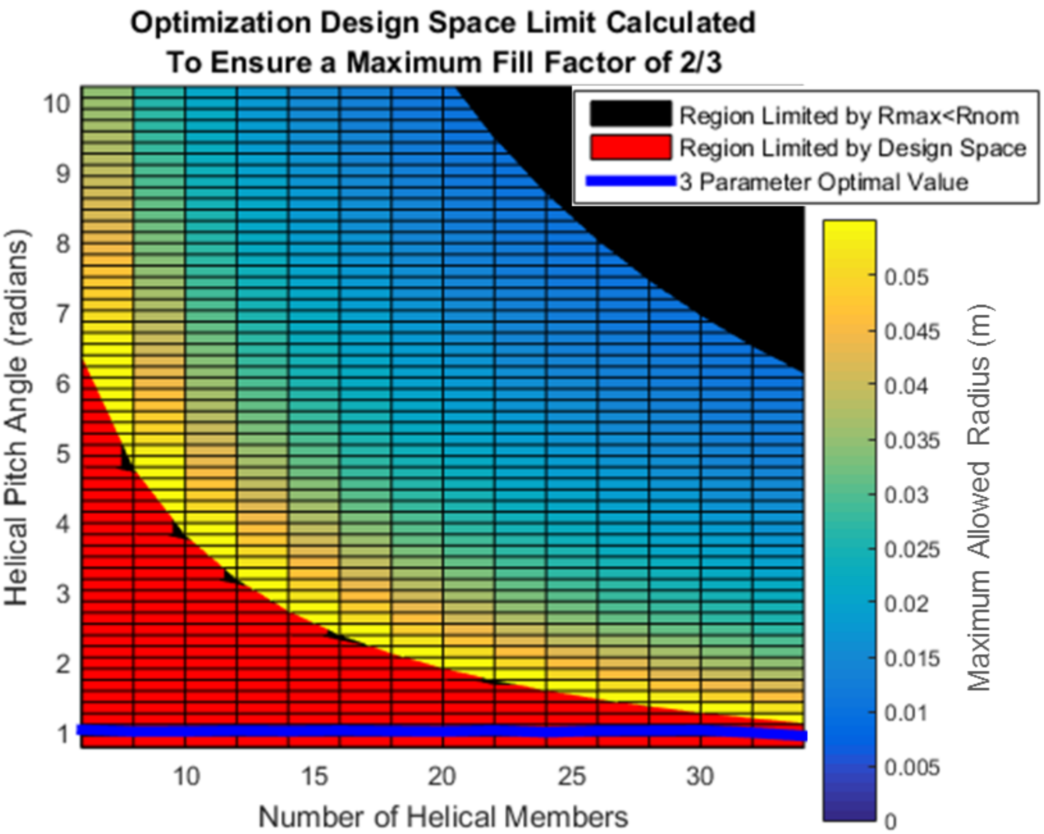

Figure 61. Five Parameter Optimization Design Space Limit.

There are three separate regions as a function of helical pitch angle and the number of helical parameters. The first region, shown in black in the upper right of Figure 61, is a region that is unable to meet the maximum fill factor of 66% through the use of the nominal parameter values. The second region, shown in red in the bottom left of Figure 61, is only limited by the full design space. The third region, shown between the first and second region, can create viable geometric cases but requires limiting the maximum helical and cylindrical radius. To calculate a specific limit, an initial limit on the design space is dictated by the optimal three parameter optimization value. In this case, the three parameter optimization value occurs where the limit is defined as the design space limit. Therefore, the design space limit is the assumed initial limit for the five parameter optimization. The resulting optimization geometries, shown in Table 17 and plotted in Figure 62, remains within the design space ensuring a fill factor of less than 66%.

Table 17. Five Parameter Optimal Geometry with the Resulting Cost Function.

5 Parameter Optimal Geometry						
Number of Helicals	Max Helical Pitch Angle (rad)	Radius (m)	Pitch Angle (Rad)	Helical Member Thickness (m)	Cylidrical Member Thickness (m)	Cost Function
34	1.96 π	0.63	1.024	0.05	0.05	0.0066

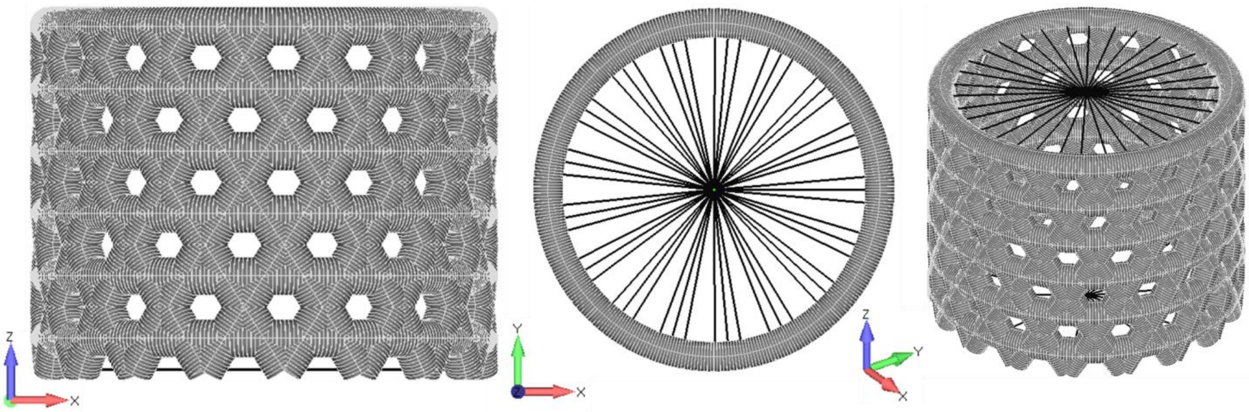

Figure 62. Five Parameter Optimized Geometry with 34 Helical M Radius of 0.625 m, a Helical Pitch angle of 1.03 rad, Helical member thickness of 0.05 m and a Cylindrical member thickness of 0.05 m.

The five parameter optimization and the three parameter optimization produce the same optimal number of helical members, the helical pitch angle, and the radius. This results in similar loading cases with minimum variations in the single helical loading displacement. These two optimized geometries morphing workspace, minimum morphing capability, and frequency response capability are evaluated in Section 7.

7. Optimized Geometry Evaluation

The morphing parameters of interest that are investigated here are: the workspace evaluation, the minimum morphing capability, configuration specific performance, and the frequency response capability. The development of the metrics is covered in more detail in [2].

7.1 Workspace Evaluation

The workspace is evaluated by applying local and global strains equal to [-4ε, -3ε, -2ε, -1ε, 0, 1ε, 2ε, 3ε, 4ε] m/m. These eight individual helical loading inputs are combined to generate every possible combination of four loaded helical members. An additional loading case of global thermal strains with the same input loading case is also applied. The resulting point cloud is plotted to determine the workspace shape and size and can be seen in Figure 63. A full description of the workspace loading development can be found in [2].

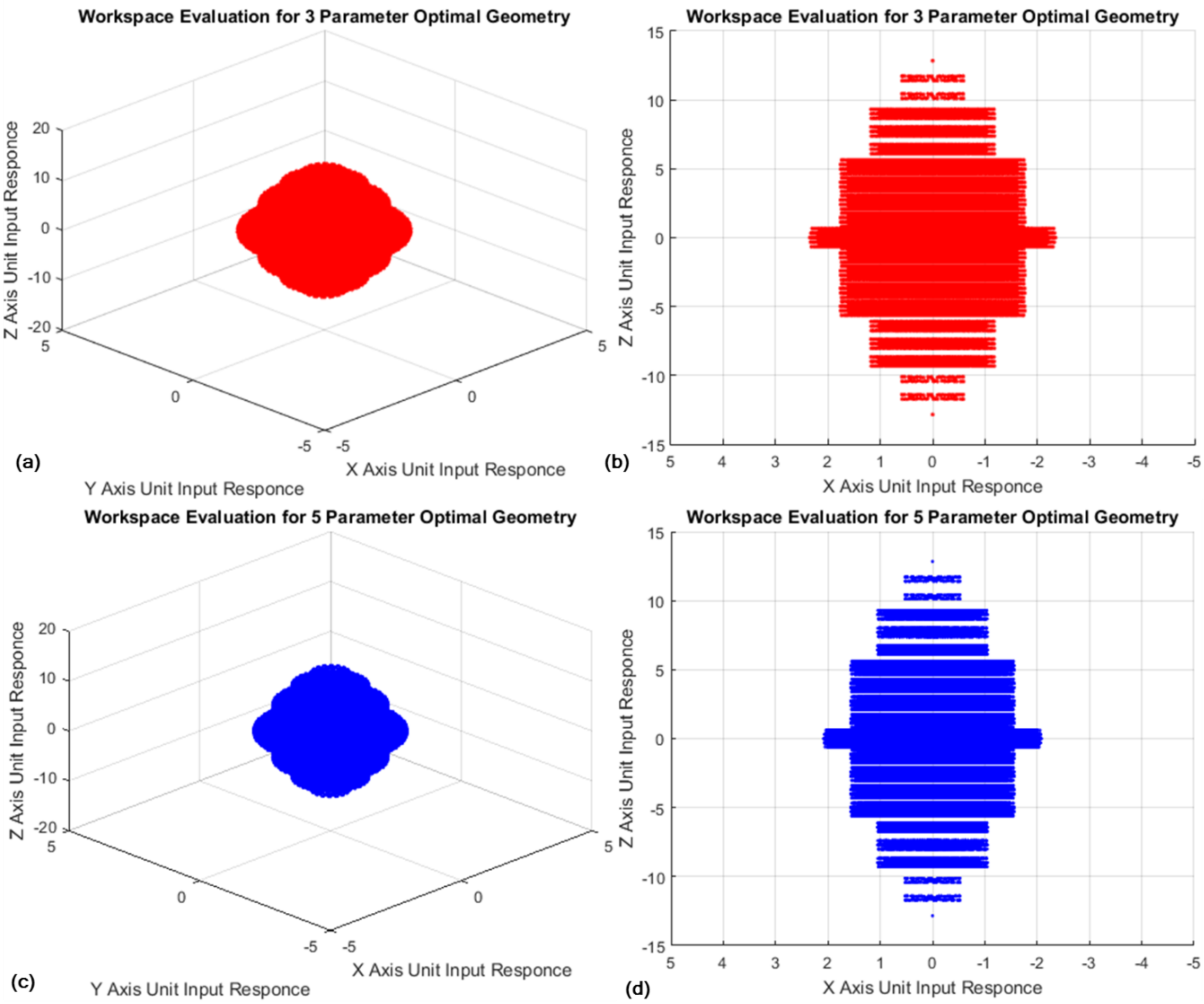

Figure 63. Workspace Evaluation for (a) 3 Parameter Optimization Isometric View, (b) 3 Parameter Optimization Side View, (c) 5 Parameter Optimization Isometric View, and the (d) 5 Parameter Optimization Side View.

7.2 Minimum Morphing Evaluation

The workspace is searched for the smallest displacements in each of the 6 DOF to evaluate the minimum morphing capability of the geometry. The minimum morphing case for both the three and five parameter optimized structures is achieved through balanced positive and negative thermal loads as demonstrated in Figure 64. The resulting minimum morphing capability in all 6 DOF for both the three and five parameter optimal geometries are seen in Table 18. The intent of this investigation is to determine the morphing limit associated with the geometric configuration. This allows material properties to be incorporated in post processing rather than requiring multiple FEM runs.

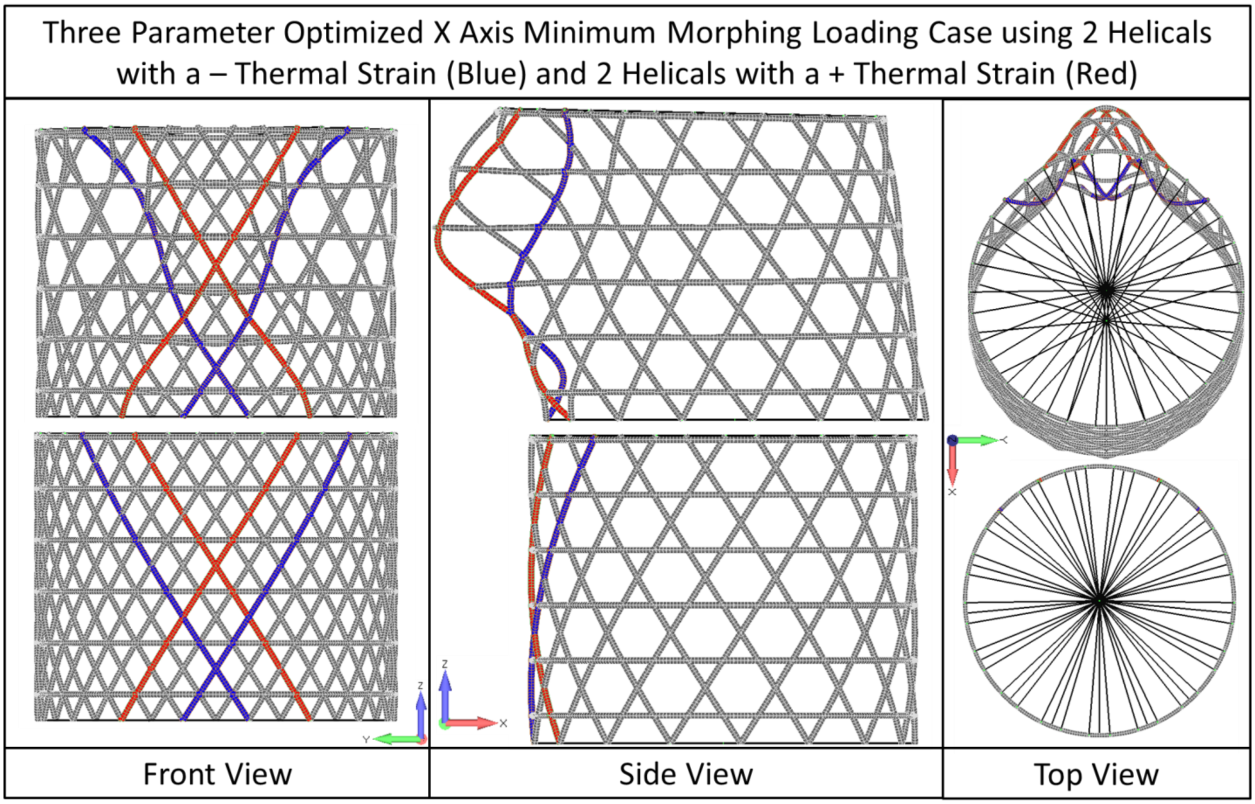

Figure 64. Minimum X Axis Morphing Control Case with a Positive Strain applied to Helical 15, and 22, and a Negative Strain applied to Helical 17 and 20.

Table 18. Optimized Minimum Morphing Vector for each of the 6 DOF and both Optimized Geometries.

	3 Parameter Optimal Geom Minimum Morphing Displacement Vector						5 Parameter Optimal Geom Minimum Morphing Displacement Vector					
	Response to a Unit Strain of 1m/m						Response to a Unit Strain of 1m/m					
	X	Y	Z	RX	RY	RZ	X	Y	Z	RX	RY	RZ
X Min Disp. Case	0.100	0.000	0.000	0.000	0.004	0.000	0.100	0.001	0.000	0.010	0.008	0.000
Y Min Disp. Case	0.009	0.099	0.000	0.004	0.000	0.000	0.001	0.097	0.000	0.001	0.010	0.000
Z Min Disp. Case	0.008	0.016	0.165	0.030	0.015	0.000	0.008	0.015	0.227	0.030	0.015	0.000
RX Min Disp. Case	0.000	0.020	0.000	0.461	0.000	0.000	0.033	0.029	0.000	0.449	0.008	0.000
RY Min Disp. Case	0.020	0.002	0.000	0.043	0.459	0.000	0.044	0.027	0.000	0.032	0.447	0.000
RZ Min Disp. Case	0.005	0.012	0.000	0.034	0.013	0.408	0.056	0.051	0.038	0.062	0.024	0.626

7.3 Scaled Morphing Capability

Once a baseline geometric response to a unit thermal strain input has been determined in Section 7.2, the specific morphing accuracy for a given material in conjunction with a given thermal control capability can be evaluated. As can be seen in Figure 65, each material property provides a different application displacement range. The carbon composite, invar, and aluminum structures can achieve 1μm displacement control in the X-axis with thermal control system accuracy of 100 °C, 8.5 °C, and 4.5 °C respectively. The resulting morphing control capabilities for the three materials in the 6 DOF, given a thermal control capability of 1°C, are documented in Table 19 and Table 20.

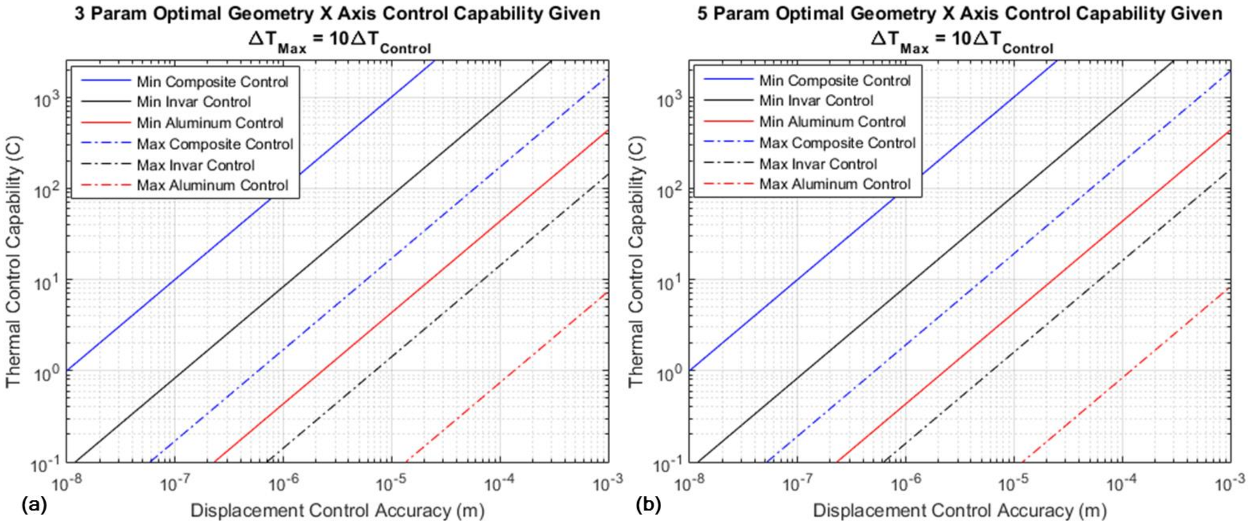

Figure 65. The Minimum and Maximum Morphing range for the X Axis Given a Maximum Applied Loading Equal to Ten Times the Control Capability for the (a) 3 Parameter Optimized Geometry and the (b) 5 Parameter Optimized Geometry.

Table 19. The 3 Parameter Optimized Displacement Control given a 1°C Thermal Control Capability for Carbon Composites, Invar, and Aluminum Material Properties.

	3 Param Displacement Control Capability (m) with 1 C Control					
	Minimum Displacement Capability			Maximum Displacement Capability		
	Composite	Invar	Aluminum	Composite	Invar	Aluminum
X Disp.	1.00E-08	1.20E-07	2.30E-06	6.00E-07	7.00E-06	1.35E-04
Y Disp.	1.00E-08	1.20E-07	2.29E-06	6.00E-07	7.00E-06	1.35E-04
Z Disp.	2.00E-08	3.00E-07	5.71E-06	3.20E-06	3.85E-05	7.42E-04
RX Disp.	7.00E-08	8.00E-07	1.54E-05	5.00E-07	6.00E-06	1.16E-04
RY Disp.	7.00E-08	8.30E-07	1.59E-05	5.00E-07	6.00E-06	1.16E-04
RZ Disp.	6.00E-08	7.40E-07	1.42E-05	4.00E-07	4.90E-06	9.43E-05

Table 20. The 5 Parameter Optimized Displacement Control given a 1°C Thermal Control Capability for Carbon Composites, Invar, and Aluminum Material Properties.

	5 Param Displacement Control Capability (m) with 1 C Control					
	Minimum Displacement Capability			Maximum Displacement Capability		
	Composite	Invar	Aluminum	Composite	Invar	Aluminum
X Disp.	1.00E-08	1.20E-07	2.31E-06	5.00E-07	6.20E-06	1.20E-04
Y Disp.	1.00E-08	1.20E-07	2.23E-06	5.00E-07	6.20E-06	1.20E-04
Z Disp.	2.00E-08	2.70E-07	5.24E-06	3.20E-06	3.85E-05	7.42E-04
RX Disp.	4.00E-08	5.40E-07	1.04E-05	5.00E-07	5.50E-06	1.06E-04
RY Disp.	4.00E-08	5.40E-07	1.03E-05	5.00E-07	5.50E-06	1.06E-04
RZ Disp.	6.00E-08	7.50E-07	1.45E-05	4.00E-07	4.30E-06	8.27E-05

7.4 Frequency Response vs. Power Requirements

The final performance metric to be evaluated is the frequency response capability of this system as a function of the available power. The specific heat capacity, for each material, is multiplied by the volume of a given active member and by the temperature change in °C to calculate the total energy required. In this case, the minimum morphing case contains four active helical members actuated by 1°C. The total energy to heat the four members by 1°C is used to calculate the power and frequency response capability for the two materials and three geometric configurations.

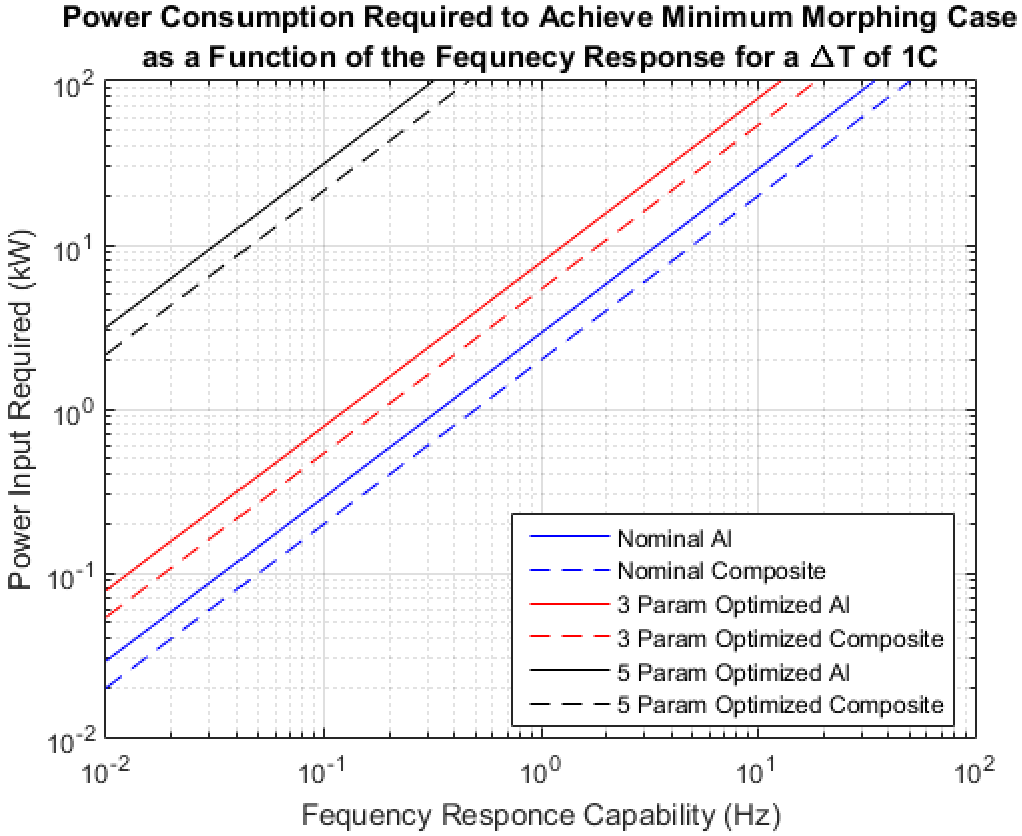

Figure 66. Frequency Response Capability for the Nominal Geometry, the Three-Parameter Optimized Geometry, and the Five Parameter Optimized Geometry.

The key driver in the frequency response capability is the helical mass. The variation in the three geometric frequency response capabilities is highly correlated to the helical cross-section. As can be seen, the three parameters optimal geometry can deliver 1 Hz frequency response capability using 6 kW.

Conclusion

This paper successfully demonstrates an efficient optimization methodology for the thermal morphing anisogrid smart structure. This work applies a parameter ranking and parameter reduction methodology previously implemented on model correlation to rank and identify the parameters critical for optimization. The ranking from this method was compared to all possible ranking orders to quantify the ranking quality. The following ranking method was used to reduce the nine parameter problem to a three and five parameter optimization problem. The resulting reduced problems are optimized using a trust-region optimization algorithm. A gradient study is done to ensure the forward difference gradient calculation step size produces stable results before optimization. The optimized geometries are then evaluated for the resulting morphing workspace, minimum morphing capability, and the frequency response capability.

The ranking methodology used in this paper was verified through the utilization of a simplified minimum search algorithm applied to five parameter design space sweep. This simplified optimization algorithm was able to quantify the relative ranking quality of all 120 possible ranking orders relative to the Q-DEIM ranking. It was shown that the Q-DEIM ranking was not the optimal ranking for the second and third parameter optimization, but the relative ranking difference was minor. Further use of this method on other problems, using a more accurate comparison may show the Q-DEIM ranking performs better than this initial evaluation. The three parameter optimized geometries cost function achieves 98.2% of the five parameters optimized cost function reduction. This justifies the use of the three parameter truncation of normalized singular values below 0.01. This methodology has been shown to accurately identify the critical pieces of complex problems and allow a more optimal use of computational and engineering resources to solve these complex problems.

The Entrust trust-region optimization method has been demonstrated with a complex optimization problem. The gradient evaluation was shown to be a successful method for identifying an appropriate step size to address discontinuities and numerical noise in a difficult optimization problem. This optimization was performed on 16 different geometric cases to ensure the full design space was evaluated.

The thermal morphing anisogrid structure was optimized to define the minimum morphing capability of the structure. The resulting three parameters and five parameter optimized geometries have been assessed for the workspace, minimum morphing capability, and the frequency response function capabilities. It was shown that the resulting five parameter geometry had a slight improvement over the three parameter optimization's performance. The three parameter system was shown to be able to achieve 10 nm displacement control in the X and Y axis with 1°C thermal control using low CTE composite materials. The available morphing design space for this structure was shown to range from 10 nm to 600 nm given an allowable maximum input loading of 10°C. A larger morphing workspace could be achieved through the use of larger temperature gradients, or through combinations of material properties in the structure itself, to provide the nano, micro, and macro morphing capabilities. Finally, this system was shown to be able to achieve 1 Hz frequency response capabilities given an input power of 6 kW.

This work has demonstrated the foundation and tools required to provide an optimized thermal morphing anisogrid structure for a wide variety of potential applications. Once a specific application is defined, the methodology in this paper can be implemented to provide an optimized structure with a broad range of power, workspace size, mass, frequency response, and minimum morphing constraints.

Acknowledgements

The authors would like to acknowledge the support by the Naval Research Laboratory through the Select Graduate Training Program.

References

1. Phoenix, A.A., S. Gugercin, and P.A. Tarazaga, *Dynamic Model Reduction Using Data-Based Loewner-SVD Methods applied to Thermally Morphing Structures.* Journal of Sound and Vibration, 2016.
2. Phoenix, A.A. and P.A. Tarazaga, *Thermal Morphing Anisogrid Smart Space Structures Part 1: Introduction, Modeling, and Performance of the Novel Smart Structural Application.* Journal of Vibration and Control, 2016.
3. Phoenix, A.A., et al., *Improved Model Correlation through Optimal Parameter Ranking using Model Reduction Algorithms: Augmenting Engineering Judgment.* Journal of Vibration and Control, 2016.
4. Phoenix, A.A., et al., *Optimal Parameter Identification for Model Correlation Using Model Reduction Methods*, in *Topics in Modal Analysis & Testing, Volume 10*. 2016, Springer. p. 281-292.
5. Wada, B.K., *Adaptive structures-An overview.* Journal of spacecraft and rockets, 1990. 27(3): p. 330-337.
6. Thayer, D., et al., *Six-axis vibration isolation system using soft actuators and multiple sensors.* Journal of spacecraft and rockets, 2002. 39(2): p. 206-212.
7. Thill, C., et al., *Morphing skins.* The Aeronautical Journal, 2008. 112(1129): p. 117-139.
8. Kuder, I.K., et al., *Variable stiffness material and structural concepts for morphing applications.* Progress in Aerospace Sciences, 2013. 63: p. 33-55.
9. Li, W. and H. Huang, *Integrated optimization of actuator placement and vibration control for piezoelectric adaptive trusses.* Journal of Sound and Vibration, 2013. 332(1): p. 17-32.
10. Toropova, M.M., *THERMAL ACTUATION THROUGH BIMATERIAL LATTICES*, in *SMASIS*. 2015.

11. Tarazaga, P.A., D.J. Inman, and W.K. Wilkie, *Control of a space rigidizable inflatable boom using macro-fiber composite actuators.* Journal of Vibration and Control, 2007. 13(7): p. 935-950.
12. Ruggiero, E.J. and D.J. Inman, *Gossamer spacecraft: recent trends in design, analysis, experimentation, and control.* Journal of Spacecraft and Rockets, 2006. 43(1): p. 10-24.
13. Ramrakhyani, D.S., et al., *Aircraft structural morphing using tendon-actuated compliant cellular trusses.* Journal of aircraft, 2005. 42(6): p. 1614-1620.
14. Korkmaz, S., *A review of active structural control: challenges for engineering informatics.* Computers & Structures, 2011. 89(23): p. 2113-2132.
15. Hiroaki, T., et al., *Development of a smart reconfigurable reflector prototype for an extremely high-frequency antenna.* Journal of Intelligent Material Systems and Structures, 2015: p. 1045389X15580660.
16. Chopra, I., *Review of state of art of smart structures and integrated systems.* AIAA journal, 2002. 40(11): p. 2145-2187.
17. Li, D.-X. and R. Xu, *Optimal Design and Control of Smart Space Structures: A Memetic Evolution Approach.* Intelligent Systems, IEEE, 2014. 29(1): p. 40-46.
18. Garba, J.A., B.K. Wada, and J.L. Fanson, *Adaptive structures for precision controlled large space systems.* Journal of intelligent material systems and structures, 1992. 3(2): p. 348-366.
19. Stewart, D., *A platform with six degrees of freedom.* Proceedings of the institution of mechanical engineers, 1965. 180(1): p. 371-386.
20. Yang, J., et al., *Design of a Vibration Isolation System for the Space Telescope.* Journal of Guidance, Control, and Dynamics, 2015: p. 1-8.
21. Wedeking, G.A., J.J. Zierer, and J.R. Jackson. *Kinematic optimization of upgrade to the Hobby-Eberly Telescope through novel use of commercially available three-dimensional CAD package*. in *SPIE Astronomical Telescopes+ Instrumentation*. 2010. International Society for Optics and Photonics.
22. Zierer, J.J., et al. *The development of high-precision hexapod actuators for the Hobby-Eberly Telescope Wide Field Upgrade*. in *SPIE Astronomical Telescopes+ Instrumentation*. 2010. International Society for Optics and Photonics.
23. Zierer, J.J., et al. *Design, testing, and installation of a high-precision hexapod for the Hobby-Eberly Telescope dark energy experiment (HETDEX)*. in *SPIE Astronomical Telescopes+ Instrumentation*. 2012. International Society for Optics and Photonics.
24. Zhu, Y., A. Corigliano, and H.D. Espinosa, *A thermal actuator for nanoscale in situ microscopy testing: design and characterization.* Journal of Micromechanics and Microengineering, 2006. 16(2): p. 242.
25. Bühler, J., et al., *Thermally actuated CMOS micromirrors.* Sensors and Actuators A: Physical, 1995. 47(1): p. 572-575.
26. Schweizer, S., et al., *Thermally actuated optical microscanner with large angle and low consumption.* Sensors and Actuators A: Physical, 1999. 76(1): p. 470-477.
27. Rahafrooz, A., et al. *Thermal actuation, a suitable mechanism for high frequency electromechanical resonators*. in *Micro Electro Mechanical Systems (MEMS), 2010 IEEE 23rd International Conference on*. 2010. IEEE.
28. Kim, D.H., Y.C. Park, and S. Park, *Design and fabrication of twisting-type thermal actuation mechanism for micromirrors.* Sensors and Actuators A: Physical, 2010. 159(1): p. 79-87.
29. Moulton, T. and G. Ananthasuresh, *Micromechanical devices with embedded electro-thermal-compliant actuation.* Sensors and Actuators A: Physical, 2001. 90(1): p. 38-48.
30. Schmid, P., F. Hernandez-Guillen, and E. Kohn, *Diamond switch using new thermal actuation principle.* Diamond and related materials, 2003. 12(3): p. 418-421.
31. Singh, J., et al., *3D free space thermally actuated micromirror device.* Sensors and Actuators A: Physical, 2005. 123: p. 468-475.
32. Toropova, M.M. and C.A. Steeves, *Adaptive bimaterial lattices to mitigate thermal expansion mismatch stresses in satellite structures.* Acta Astronautica, 2015. 113: p. 132-141.
33. Toropova, M. and C. Steeves, *Bimaterial lattices with anisotropic thermal expansion.* Journal of Mechanics of Materials and Structures, 2014. 9(2): p. 227-244.
34. Eckstein, E., A. Pirrera, and P.M. Weaver, *Thermally Driven Morphing with Hybrid Laminates and Metal Matrix Composites.* Mechanics, 2015. 2: p. 11.
35. Pirrera, A., D. Avitabile, and P. Weaver, *On the thermally induced bistability of composite cylindrical shells for morphing structures.* International Journal of Solids and Structures, 2012. 49(5): p. 685-700.
36. Eckstein, E., et al., *THERMALLY-DRIVEN SNAP-THROUGH AND MULTISTABILITY USING LAMINATED FIBRE-METAL SHELLS.*

37. Malladi, S.V. and P.A. Tarazaga. *Sensorless Control of SMA Using Seebeck Voltage*. in *ASME 2012 Conference on Smart Materials, Adaptive Structures and Intelligent Systems*. 2012. American Society of Mechanical Engineers.
38. Malladi, S.V.N. and P.A. Tarazaga, *Modeling of Hysteresis Effect of SMA using Neuro Fuzzy Inference System.* 2013.
39. Malladi, V.S. and P.A. Tarazaga. *Control of Strain Characteristics of SMA Wires Using Seebeck Voltage*. in *ASME 2013 Conference on Smart Materials, Adaptive Structures and Intelligent Systems*. 2013. American Society of Mechanical Engineers.
40. Malladi, V.S. and P.A. Tarazaga, *ANFIS driven strain control of thin-SMA wires using Seebeck voltage of an SMA-Constantan thermocouple.* 2014.
41. Malladi, V.V.N.S., *Development and Design of Self-Sensing SMAs using Thermoelectric Effect.* 2013.
42. Renno, J.M., et al. *A new approach for changing structural properties of a membrane mirror strip for adaptive optics applications*. in *ASME 2007 International Design Engineering Technical Conferences and Computers and Information in Engineering Conference*. 2007. American Society of Mechanical Engineers.
43. Tarazaga, P.A., M.E. Johnson, and D.J. Inman, *Vibro-acoustics of a pressurized optical membrane.* Mechanical Systems and Signal Processing, 2012. 30: p. 373-392.
44. Tarazaga, P.A., M.E. Johnson, and D.J. Inman, *Experimental validation of the vibro-acoustic model of a pressurized membrane.* Mechanical Systems and Signal Processing, 2014. 45(2): p. 330-345.
45. Sorensen, D.C. and M. Embree, *A DEIM Induced CUR Factorization.* arXiv preprint arXiv:1407.5516, 2014.
46. Farhat, C. and F.M. Hemez, *Updating finite element dynamic models using an element-by-element sensitivity methodology.* AIAA journal, 1993. 31(9): p. 1702-1711.
47. Mottershead, J.E., M. Link, and M.I. Friswell, *The sensitivity method in finite element model updating: a tutorial.* Mechanical Systems and Signal Processing, 2011. 25(7): p. 2275-2296.
48. Lim, J.H., *A correlation study of satellite finite element model for coupled load analysis using transmissibility with modified correlation measures.* Aerospace Science and Technology, 2014. 33(1): p. 82-91.
49. Homma, T. and A. Saltelli, *Importance measures in global sensitivity analysis of nonlinear models.* Reliability Engineering & System Safety, 1996. 52(1): p. 1-17.
50. Haukaas, T. and A. Der Kiureghian, *Parameter sensitivity and importance measures in nonlinear finite element reliability analysis.* Journal of engineering mechanics, 2005. 131(10): p. 1013-1026.
51. Helton, J.C., et al., *Survey of sampling-based methods for uncertainty and sensitivity analysis.* Reliability Engineering & System Safety, 2006. 91(10): p. 1175-1209.
52. Ionescu-Bujor, M. and D.G. Cacuci, *A comparative review of sensitivity and uncertainty analysis of large-scale systems-I: Deterministic methods.* Nuclear science and engineering, 2004. 147(3): p. 189-203.
53. Cacuci, D.G. and M. Ionescu-Bujor, *A comparative review of sensitivity and uncertainty analysis of large-scale systems-II: Statistical methods.* Nuclear Science and Engineering, 2004. 147(3): p. 204-217.
54. Iooss, B. and P. Lemaître, *A review on global sensitivity analysis methods*, in *Uncertainty Management in Simulation-Optimization of Complex Systems*. 2015, Springer. p. 101-122.
55. Drmac, Z. and S. Gugercin, *A New Selection Operator for the Discrete Empirical Interpolation Method--improved a priori error bound and extensions.* arXiv preprint arXiv:1505.00370, 2015.
56. Bales, D.B., et al., *Sensor Truncation via Gait Classification using Underfloor Accelerometers.* IEEE Internet of Things, 2016.
57. Borggaard, J. and J. Burns, *A PDE sensitivity equation method for optimal aerodynamic design.* Journal of Computational Physics, 1997. 136(2): p. 366-384.
58. Dennis, J.A.S., R., *Numerical Methods for Unconstrained Optimization and Nonlinear Equations*. Numerical Methods for Unconstrained Optimization and Nonlinear Equations.
59. Borggaard, J., D. Pelletier, and K. Vugrin. *On sensitivity analysis for problems with numerical noise*. in *Proc. 9th AIAA/NASA/USAF/ISSMO Symposium on Multidisciplinary Analysis and Optimization*. 2002.
60. Burman, J. and B. Rikard Gebart, *Influence from numerical noise in the objective function for flow design optimisation.* International Journal of Numerical Methods for Heat & Fluid Flow, 2001. 11(1): p. 6-19.
61. Carter, R.G., *On the global convergence of trust region algorithms using inexact gradient information.* SIAM Journal on Numerical Analysis, 1991. 28(1): p. 251-265.
62. Gilmore, P., et al., *Implicit filtering and optimal design problems*, in *Optimal Design and Control*. 1995, Springer. p. 159-176.

Summary, Path Forward, and Contributions

This paper has demonstrated the foundation and tools required to provide an optimized thermal morphing anisogrid structure for a wide variety of potential applications. Once a specific application is defined, the methodology in this paper can be implemented to provide an optimized structure with a broad range of power, workspace size, modal properties, mass, frequency response, and minimum morphing constraints. This capability has been achieved through three different efforts: Dynamic model reduction parameter importance calculations, and, finally, a full evaluation of the concepts morphing performance and an optimization of the minimum morphing capability.

This effort has shown that the Loewner-SVD data based model reduction approach can efficiently model and reduce complex dynamical systems. This work has demonstrated the reduced model development methodology using FEM transfer functions and demonstrated the method for development of test data based reductions. The 10,272 × 10,272 stiffness and mass matrix of the anisogrid system were reduced to an accurate 30 × 30 state space model with a resulting $H_2\ norm$ error of 0.3. This model reduction method has been shown to provide an opportunity to add to the state-of-the-art in reduced models for finite element model reduction problems as well as provide unique opportunities to develop reduced models from test data. The method is computationally efficient, enabling the calculation of multiple reduction sizes to ensure that the optimal reduction model is chosen. Furthermore, it has been shown that this method is simple to use and can provide valuable model reduction capability without the need for a prior accurate model development.

The methodology for parameter ranking has been shown to be accurate, computationally efficient and robust to engineering errors. The ranking used shows significant improvement over engineering judgment and demonstrates a potential improvement in the field of sensitivity analysis through the addition of advanced algorithms to evaluate the importance rather than simply the scale of a parameter's impact. Hypothesis testing was used to determine the best performing methodology between all variations of: the inputs used to generate the sensitivity input matrix, the model reduction method used, the weighting method chosen, and a sweep evaluating the effect of errors between the expected and real design space. From this study, the Q-DEIM linear weighted method using inputs at the maximum and minimum of the design space demonstrated itself as the best ranking method. The robustness of all ranking methods are evaluated against 0%, 5%, 10%, 25%, 50%, and 75% uncertainty in the initially applied error bound. The resulting ranking has been shown to be robust to substantial uncertainty in the error bound showing value in the method even if there is little knowledge of the problem.

Furthermore, this paper successfully demonstrates an efficient optimization methodology for the thermal morphing anisogrid smart structure. This method for modeling and evaluation is shown to be feasible and to have a low computational cost. This paper has shown that the thermal morphing anisogrid high precision morphing concept has significant promise for high precision thermal control in the space environment. The nominal geometry using low CTE composite was shown to have a minimum morphing capability of 30 nm in the X-axis given a thermal control capability of 1°C and a maximum displacement capability of 1 μm. A simple evaluation of the design space found the minimum cost function to be 0.0077 and a maximum cost function of 513. The resulting five orders of magnitude variation in the cost function demonstrates the range of applications that the anisogrid thermal morphing system can address.

The parameters ranking methodology was verified, and the three parameter optimization achieved 98% of the overall cost function reduction that the five parameter optimization effort provided. The minimum morphing X and Y axis control was found to achieve a minimum control of 10 nm and a maximum control of 600 nm, given a thermal control capability of 1°C and an allowable maximum input loading of 10°C. Finally, this system was shown to be able to achieve 1 Hz frequency response capabilities given an input power of 6 kW. This work has demonstrated the foundation and tools required to provide an optimized thermal morphing anisogrid structure for a wide variety of potential applications. Once a specific application is defined, the methodology in this paper can be implemented to provide an optimized structure with a broad range of power, workspace size, mass, frequency response, and minimum morphing constraints.

This effort contributed to the field of model reduction by demonstrating the Data Based Loewner method on a variety of classical engineering problems to identify computational cost and quality of the resulting reduction. An iterative method was identified as a valid method to define the optimally reduced model scale. The overall reduction capability of the Data-Based Loewner model reduction method has been quantified on complex FEM structures. To expand beyond the work done here, the implementation of this model reduction method, to provide a state space model based on test data, could provide unparalleled model coupling predictions in the high-frequency regime.

Through this investigation, an opportunity to expand upon the use of the Loewner method was identified. A fundamental limit in current reduced models is that their accuracy is limited based on the accuracy of the modeling method being reduced. The use of test data provides opportunities to generate accurate models where the development of an accurate model is difficult or impossible. One of the classic issues with the current modeling methods is the capturing of high-frequency dynamics. The effort shown in this work can be expanded to provide an alternative method to develop highly accurate dynamic models that could provide unparalleled coupled model predictions using test data. An opportunity exists to expand the method by generating the reduced model in the form of a stiffness and a mass matrix, rather than by the state space representation. This would enable simple integration of the reduced models into well-established FEM code, allowing for untested structures to be coupled with the high-frequency Loewner Data Based models and providing increased accuracy coupling dynamic predictions.

The parameter ranking methodology described here expands on the capability of classical sensitivity analysis by adding an intelligent ranking algorithm to the classic sensitivity method. This approach has been shown to be robust for use in model correlation efforts as well as for the selection of parameters for optimization. To improve the performance of this methodology and to ensure its validity on other cases, further investigation into the best data to provide to the algorithm and a study into the normalization methods are needed. The method demonstrated here used parameter values at the edges of the design space, but further investigation into alternative methods could improve performance. Alternate weighting methods and normalization techniques should also be applied to evaluate potential performance improvements. An additional application of interest for this methodology is in the ranking of parameter importance for the generation of neural networks and other machine learning methods trying to solve complex problems, such as model correlation. As non-critical parameters are removed from the machine learning effort, the quality of the model performance improves and the method's computational costs reduce. Identifying the right truncation point to maximize model accuracy greatly increases the potential of machine learning algorithms. The author is currently investigating the improvements in computational cost and the neural network performance improvement when this methodology is applied. This effort may enable machine learning algorithms, trained on FEM data, to instantly predict parameter values that would correlate a dynamic FEM to test data. This has the potential to identify errors in the FEM or failures in the test specimen during low energy testing so that FEM issues or structural failures can be addressed before the application of high energy environments.

To improve on the current methods used to evaluate the thermal morphing anisogrid structure, the combined loading cases need to be better understood. Current efforts in assessing the minimum morphing capability took a brute force approach requiring the search area within the design space to be limited. A significant advance in performance could be found through a deeper understanding of the optimal morphing configurations for 6 DOF control. To achieve this, a greater understanding of the relationship between the geometric inputs and the minimum morphing loading combination case needs to be investigated. This would also provide the required insight needed to build a better optimization cost function and improve on the minimum morphing geometry. Several other morphing performance criteria have yet to be addressed, including: corrective force capability, dynamic properties as a function of geometry, manufacturing tolerance effects, thermal morphing specific failure modes, and the calculation of convective losses. Through addressing these needs, the concept can be applied to a specific morphing application with greater success.

A significant portion of the work associated with this effort was focused on the development of the parameterized Matlab code used to build and run the FEM. To encourage further efforts in this field, the parameterized Matlab code is published openly at (https://github.com/A-Phoenix/Anisogrid-Model) to allow others to build upon this work.

This work has addressed issues in the fields of model reduction, sensitivity analysis, FEM development, optimization, and adaptive morphing structures. While future investigations are required, through this effort, the thermal morphing anisogrid structural performance has been quantified.